

ABSTRACT

Title of Dissertation: THEORETICAL, EXPERIMENTAL,
AND OBSERVATIONAL STUDIES OF
IRON X-RAY SPECTRA: FROM THE
LABORATORY TO THE UNIVERSE

Gabriel J Grell
Doctor of Philosophy, 2024

Dissertation Directed by: Professor Richard Mushotzky
Department of Astronomy

The spectral lines of iron ions, particularly the dominant neon-like Fe XVII charge state, provide crucial diagnostics for the physical conditions of hot astrophysical plasmas in the X-ray regime. However, the diagnostic utility of these lines are hampered by significant discrepancies at the $\sim 20\%$ level between spectral observations, laboratory experiments, and theoretical calculations of the astrophysically important Fe XVII transitions, an issue that has been observed in numerous studies over several decades. Understanding the source of these discrepancies is critical for the improvement of both theoretical atomic models and laboratory experiment data on transition energies and cross sections of electron-ion processes, which themselves will be key for comparison to observations from X-ray spectroscopy missions such as *XRISM*, *Line Emission Mapper (LEM)*, *Arcus*, and *Athena*. My dissertation encapsulates the main branches of X-ray astrophysics by focusing on the use of theoretical models and experimental measurements to further the diagnostic use, understanding, and interpretation of spectroscopic observations of

iron transition lines.

I modeled the effects of UV photoexcitation in O-type stars on a spectral line ratio of the Fe XVII $3s - 2p$ transitions in an attempt to explain an anomalous value found for the X-ray spectra of the O star ζ Puppis. I conjectured that the strong UV field of ζ Pup produces the observed ratio by depopulation of metastable $3s$ excited states, and that the ratio can potentially be used as an independent diagnostic of the radial distribution of X-ray-emitting plasma. Using the Flexible Atomic Code (FAC) collisional-radiative model to model the effect of UV photoexcitation on the Fe XVII lines, I compared the model calculations to archival spectra of coronal and hot stars from the *Chandra* HETGS and *XMM-Newton* RGS. The calculations showed that UV photoexcitation does not produce a sufficiently large dynamic range in the Fe XVII line ratio to explain the difference in the observed ratio between coronal stars and ζ Pup.

I used FAC to compute steady-state populations of Fe XVII states and calculate cross sections for the dielectronic recombination (DR) and direct electron-impact excitation (DE) line formation channels of Fe XVII, and benchmarked the model predictions with experimental cross sections of Fe XVII resonances that were mono-energetically excited in an electron beam ion trap (EBIT) experiment. I extended the benchmark to all resolved DR and DE channels in the experimental dataset with a focus on the $n \geq 4$ DR resonances, finding that the DR and DE absolute cross section predictions for the higher n complexes disagree considerably with experimental results when using the same methods as in previous works. However, agreement within $\sim 10\%$ of the experimental results was achieved by an approach whereby I doubly convolve the predicted cross sections with both the spread of the electron-beam energy and the photon-energy resolution of the EBIT experiment. I also calculated rate coefficients from the experimental and theoretical cross sections, finding general agreement within 2σ with the rates

found in the OPEN-ADAS atomic database.

Circling back to the ζ Pup Fe XVII ratio, I probed the potential significance of the process of resonant Auger destruction (RAD), which occurs when a photon emitted by an ion is absorbed in a neighboring cooler part of the stellar wind by near-coincident inner-shell transitions of lower charge state ions. The inner-shell excited ion then undergoes Auger decay, in which the energy is transferred to an outer electron that is subsequently ejected from the atom by autoionization. EBIT measurements at a synchrotron beamline determined that $3d - 2p$ transitions of the lower iron charge state Fe VI is nearly coincident in transition energy with the Fe XVII 3G line, which would enable possible destruction of Fe XVII 3G photons and thus a potential explanation of the lower line intensity ratio found in ζ Pup. Model calculations show a noticeable amount of optical thickness for the Fe VI line, but the calculated X-ray line profile model does not show nearly enough reduction of the Fe XVII 3G line to suggest that RAD by Fe VI lines is causing the ratio anomaly in ζ Pup.

Finally, I introduce preliminary steps for the analysis of XRISM spectral observations of Fe $K\alpha$ lines from the starburst galaxy Messier 82. The key unsolved questions regarding M82 are what drives the hot wind and how much gas escapes the galaxy. Understanding the hot wind requires accurate measurements of its energy content, which requires obtaining constraints for the density, temperature, and velocity at the wind's base. In order to sufficiently constrain the hot component velocity, the 6.7 keV Fe XXV line width and center must be determined to better than 10%. This accuracy requires an energy resolution $\Delta E \leq 5$ eV, which can be achieved by the high-resolution X-ray measurements with the XRISM Resolve calorimeter array. The M82 observation and subsequent analysis will confirm whether hot gas pressure is the primary driver of the galactic wind by measuring the energy contained in the $T \sim 10^8$ K hot gas, and will constrain

the mass-loading rate by measuring the velocity of the superheated nuclear gas using the Fe XXV line width.

By completing these works, I will have successfully contributed to the refinement and advancement of theoretical, laboratory, and observational X-ray astrophysical data for iron transition lines.

THEORETICAL, EXPERIMENTAL, AND OBSERVATIONAL STUDIES OF
IRON X-RAY SPECTRA: FROM THE LABORATORY TO THE UNIVERSE

by

Gabriel J Grell

Dissertation submitted to the Faculty of the Graduate School of the
University of Maryland, College Park in partial fulfillment
of the requirements for the degree of
Doctor of Philosophy
2024

Advisory Committee:

Professor Richard Mushotzky, Chair / Advisor
Dr. Maurice Leutenegger, Research Advisor
Professor Michael Coleman Miller
Professor Christopher Reynolds
Professor James Drake, Dean's Representative

© Copyright by
Gabriel J Grell
2024

Preface

Much of the work presented in this dissertation has been published in peer-reviewed journals. Chapter 2 was published in *The Astrophysical Journal* as "Fe XVII 2p-3s Line Ratio Diagnostic of Shock Formation Radius in O Stars" (Grell et al., 2021) and is presented with minimal modifications. This work was also presented at the *American Astronomical Society* winter meeting in 2021.

Chapter 3 was published in *The Astrophysical Journal* as "Laboratory Benchmark of $n \geq 4$ Dielectronic Recombination Satellites of Fe XVII" (Grell et al., 2024) and is presented with minimal modifications. The experimental research was funded by the Max Planck Society (MPS), Germany. This work was also presented at the *Atomic Processes in Plasmas* and the *International School on Atomic and Molecular Data Evaluation* conferences in 2023, and the *American Astronomical Society* winter meeting in 2024.

Chapter 4 is an early draft of a paper currently in preparation for submission to *The Astrophysical Journal*. We anticipate that this chapter will be submitted for publication soon after the submission of this dissertation.

Most of the work discussed in this dissertation was supported by NASA's Astrophysics Program under NASA award No. 80GSFC21M0002.

Dedication

To my family.

Acknowledgments

As I write my acknowledgments, I look back on my entire life journey and the people that have been there along the way. From immigrating from the island of Trinidad to being on the precipice of attaining my doctorate degree, my road to this point has not come without its bumps and I would be remiss not to thank the incredible people that have supported and encouraged me all these years.

I would first like to thank my advisors. Maurice, thank you for taking a chance on me as your research assistant. Your guidance, knowledge, humor, and genuine passion for the field have helped me become both a better scientist and a better person. I cannot thank you enough for your support, and I'm looking forward to keeping our regular Taco Bell trips and Monday morning football chats going. Hopefully we'll get a Ravens-Packers Super Bowl in the next few years.

Richard, thank you for your constant words of encouragement and belief in my ability. I've always been appreciative of your mental check-ins and making sure I'm happy, especially during the pandemic. Your reassurance has been immensely important to me and I'm grateful that you've always had my back.

I also thank my thesis committee members Cole, Chris, and Jim. Thank you for agreeing to be a part of my committee and for your helpful feedback throughout my candidacy.

I must also give a special thanks to my Harvard undergraduate advisors Randall, John, and Jason. I remember being very on-the-fence about going to graduate school before you all convinced me to apply, and I can say without a doubt that I wouldn't be where I am today without your support.

I thank my Goddard colleagues Chintan, Scott, Renata, and Roi for their guidance and

words of advice. Chintan, I'm especially grateful for your guidance during my time in Germany. Thank you for looking after me and helping me navigate both Hamburg and Heidelberg; I look back at that experience as the highlight of my time in graduate school.

I am extremely grateful for all of my graduate school classmates at the University of Maryland. Joe, Vicente, Ben, Erica, Ramsey, Harrison, Milena, Tomás: thank you all for your friendship, help with problem sets, the house parties, the Town Hall happy hours, and for being the best company in the department and at conferences.

To my hometown friends, I am truly blessed to have had such caring, genuine, and motivating friendships over the years. I thank some of my closest friends: Shamim, Omar, Vijay, Taha, Jairo, Suraj, Lucas, Karam, Ben. We've all grown up together and I'm so proud to call you my brothers. Ben I hope you're living it up in paradise and I'll cherish all the great times we had forever. In particular, I want to give a special thanks to my roommates John and Jake. Living together at UMD, through a pandemic, and now as your tenant, you both have truly become best friends of mine and I cannot thank you enough.

Going all the way back to grade school, I'd like to thank a few particular teachers: Mrs Crystal, Mr Sharrow, Dr Goldenberg, Mr Nelson, Coach Coco. Thank you for seeing something in me and inspiring me to reach for the stars, I wouldn't be here without your guidance. I also thank the entire Ingenuity Project for giving Baltimore City kids like me the opportunity to have this career path.

To my godmother Denise, you have loved me as one of your own and I cannot thank you enough for your support and encouragement. Thank you for always being there for me and my family Aunty.

To my sisters Jessy and Keisha, I cannot put into words how much I love and appreciate

you both. Thank you for always having my back, for being my confidants, for the airport rides, for helping with my constant apartment moves, and for being both my biggest haters (I definitely needed it) and biggest supporters through all the ups and the downs.

Lastly to my parents Vanessa and Jeffrey, I owe all of this to your endless love and support. Thank you for all of the sacrifices you have made, the values and life lessons you have instilled in me, driving us to school every day, coming to every sports game and school event, and for all of the ways you have helped me become the person I am today. I love you both with all my heart and I will always strive to make you proud.

Table of Contents

Preface	ii
Dedication	iii
Acknowledgements	iv
Table of Contents	vii
List of Tables	x
List of Figures	xi
List of Abbreviations	xiii
Chapter 1: Introduction	1
1.1 History of X-ray Spectroscopy	1
1.2 Atomic Processes in X-ray Spectra	6
1.2.1 Radiative Transitions	8
1.2.2 Excitation	9
1.2.3 Ionization	10
1.2.4 Recombination	15
1.2.5 Cross Sections and Rate Coefficients	17
1.2.6 Astrophysical Plasmas	18
1.3 Spectral Line Diagnostics	20
1.4 Theoretical Spectral Modelling	25
1.4.1 Atomic Structure	25
1.4.2 Plasma Modelling Codes	30
1.4.3 Flexible Atomic Code	32
1.5 Laboratory Experiments	34
1.5.1 Electron Beam Ion Trap	35
1.5.2 X-ray Detectors	41
1.6 Iron Transition Lines	44
1.7 Outline of Dissertation	51
Chapter 2: Fe XVII $2p$ - $3s$ Line Ratio Diagnostic of Shock Formation Radius in O Stars	53
2.1 Introduction	53
2.2 Fe XVII Diagnostics of UV Field Intensity and Density	58

2.3	Atomic Model	64
2.3.1	FAC	64
2.3.2	Analytical Model	66
2.3.3	Model Atmospheres	74
2.4	Line Profile Model	76
2.5	Model Fitting and Results	80
2.5.1	Observations and Data Reduction	80
2.5.2	Fitting Results	82
2.6	Discussion	89
2.7	Conclusions	93
2.8	Acknowledgments	94
Chapter 3: Laboratory Benchmark of $n \geq 4$ Dielectronic Recombination Satellites of Fe XVII		95
3.1	Introduction	95
3.2	Experiment	98
3.3	Electronic-Structure Calculations	99
3.4	Data Analysis and Results	103
3.4.1	Data Calibration	103
3.4.2	Absolute Cross Section Calibration	110
3.4.3	Doubly Convolved Cross Sections	111
3.4.4	Rate Coefficients	113
3.5	Discussion	116
3.6	Conclusions	118
3.7	Acknowledgments	120
Chapter 4: Investigating Resonant Auger Destruction of Fe XVII $3s - 2p$ Lines in O Stars		122
4.1	Introduction	122
4.2	Experiment	127
4.3	Optical Depth Model Calculations	128
4.4	Line Profile Model	134
4.5	Discussion and Future Work	138
4.6	Conclusions	141
Chapter 5: Conclusions		143
5.1	Future Work	143
5.1.1	XRISM Spectral Analysis of Messier 82	143
5.1.2	Preliminary M82 XRISM Spectra	150
5.1.3	Extension of Previous Works	150
5.2	Summary of Dissertation	152
Appendix A: Chapter 2 Appendix		155
A.1	Archival Observations	155
A.2	Solution of Rate Equations	158

Appendix B: Facilities and Software Used in Dissertation 167
 B.1 Facilities 167
 B.2 Software 167
Bibliography 169

List of Tables

2.1	Fe XVII Energy Levels	60
2.2	Fe XVII 3s Transitions and Oscillator Strengths	72
2.3	Log of Key Stellar Parameters and OBsIDs	81
3.1	Experimental and FAC-Calculated Integrated Cross Sections with Deviations . . .	115
3.2	FAC-Calculated Rate Coefficients for Different Electron Temperatures Compared to Values from OPEN-ADAS	119
A.1	Log of Archival Observations from <i>Chandra</i> and <i>XMM-Newton</i>	155

List of Figures

1.1	Direct Electron-Impact Excitation and Photoexcitation Diagrams	11
1.2	Resonant Excitation Diagram	12
1.3	Collisional Ionization and Photoionization Diagrams	14
1.4	Dielectronic Recombination Diagram	16
1.5	Electron Temperature Dependency of G Ratio and Electron Density Dependency of R Ratio	24
1.6	He-like Ion Radiative Transitions	29
1.7	Schematics of Electron Beam Ion Trap	37
1.8	FLASH-EBIT at LCLS	40
1.9	Electron Beam Ion Trap Sub-Assemblies	42
1.10	Comparison of Observed, Experimental, and Theoretical Values for Fe XVII ($3G$ + $M2$) / $3C$ Ratio	48
1.11	Experimental versus Theoretical Fe XVII $3d$ Direct Electron-Impact Cross Sections	50
2.1	<i>XMM-Newton</i> RGS Spectra of ζ Pup and ζ Ori	57
2.2	Fe XVII Radiative Transitions	59
2.3	Fe XVII $3s$ Fractional Line Strengths	68
2.4	Model-predicted Fe XVII $3s$ Ratios	69
2.5	Observed versus Calculated Fe XVII $3F$ Fractions as a Function of Photospheric Blackbody Temperature	70
2.6	Fe XVII $3F$ Fractions vs. UV Field Intensity (W)	71
2.7	Comparison of Blackbody and TLUSTY Models	75
2.8	Observed versus Calculated Fe XVII $3F$ Fractions as a Function of Stellar Effective Temperature	77
2.9	Comparisons of <i>newind</i> Models as a Function of Effective Temperature	79
2.10	Capella Fe XVII $3s$ Spectra from <i>Chandra</i> MEG Fit with Gaussian Models	83
2.11	ζ Pup Fe XVII Spectra from the <i>XMM-Newton</i> RGS Fit with <i>newind</i> Model	86
2.12	ζ Pup Fe XVII Spectra from the <i>XMM-Newton</i> RGS Fit with Gaussian Models	87
2.13	Fe XVII Fractional Line Strengths as a Function of UV Field Temperature	88
3.1	X-ray Photon Flux from FLASH-EBIT Experiment as a Function of Photon Energy and Electron-Beam Energy	100
3.2	X-ray Photon Flux from the Doubly Convolved FAC Calculations as a Function of Photon Energy and Electron-Beam Energy	101

3.3	$n = 4 - 2$ Experimental versus FAC-Calculated Absolute Cross Sections	104
3.4	$n = 4 - 2$ Experimental versus Doubly Convolved FAC-Calculated Cross Sections	105
3.5	$n = 5 - 2$ Experimental versus FAC-Calculated Absolute Cross Sections	106
3.6	$n = 5 - 2$ Experimental versus Doubly Convolved FAC-Calculated Cross Sections	107
3.7	$n = 6 - 2$ Experimental versus FAC-Calculated Absolute Cross Sections	108
3.8	$n = 6 - 2$ Experimental versus Doubly Convolved FAC-Calculated Cross Sections	109
4.1	Model Spectra of Fe VI $3d - 2p$ and Fe XVII $3G$ using Experimental Transition Energies	129
4.2	$p - z$ Ray Coordinate System	131
4.3	Curves of Growth Due to Fe VI Line in O Star Wind	133
4.4	Optical Depth $\tau(p, z)$ of Fe VI Line in O Star Wind	135
4.5	ζ Pup Fe XVII spectra from the <i>XMM-Newton</i> RGS Fit with <code>radwind</code> Model for Fe VI Line	137
4.6	ζ Pup Fe XVII spectra from the <i>XMM-Newton</i> RGS Fit with <code>radwind</code> Model for Fe V Line	140
5.1	<i>Chandra</i> ACIS-S Composite Image of M82	144
5.2	<i>Chandra</i> ACIS-S and <i>XMM-Newton</i> RGS Spectra of Fe XXV Lines in M82 Nuclear Region	146
5.3	Preliminary <i>XRISM</i> Resolve Spectra of M82 Nuclear Region	149

List of Abbreviations

ACIS	Advanced CCD Imaging Spectrometer
AGN	Active Galactic Nuclei
AI	Autoionization
APEC	Astrophysical Plasma Emission Code
ATHENA	Advanced Telescope for High-ENergy Astrophysics
CALDB	Calibration Database
CCD	Charge-Coupled Device
CI	Collisional Ionization
CIAO	Chandra Interactive Analysis of Observations
CE	Collisional Excitation
CGM	Circumgalactic Medium
CRM	Collional-Radiative Model
CV	Cataclysmic Variable
CX	Charge Exchange
DE	Direct Electron-Impact Excitation
DESY	Deutsches (German) Electron Synchrotron
DR	Dielectronic Recombination
DW	Distorted-Wave
EBIT	Electron Beam Ion Trap
EPIC	European Photon Imaging Camera
EWS	Embedded Wind Shock
FAC	Flexible Atomic Code
FWHM	Full-Width Half-Maximum
FOV	Field-of-View
FPCS	Focal Plane Crystal Spectrometer
HC-EBIT	Heidelberg Compact Electron Beam Ion Trap
HCI	Highly Charged Ion
HETGS	High Energy Transmission Grating Spectrometer
HRC	High Resolution Camera
HULLAC	Hebrew University / Lawrence Livermore Atomic Code
ICM	Intracluster Medium
ISM	Interstellar Medium
LETGS	Low Energy Transmission Grating Spectrometer
LCLS	Linac Coherent Light Source

LLNL	Livermore Lawrence National Laboratory
MBPT	Many Body Perturbation Theory
MCDF	Multi-Configuration Dirac-Fock
MCHF	Multi-Configuration Hartree-Fock
MCP	Microchannel Plate
MPI-K	Max Planck Institute for Nuclear Physics
NASA	National Aeronautics and Space Administration
NIST	National Institute of Standards and Technology
OGS	Objective Grating Spectrometer
PES	Photoelectron Spectrometer
PI	Photoionization
PV	Performance Verification
RAD	Resonant Auger Destruction
RE	Resonant Excitation
RGS	Reflection Grating Spectrometer
RR	Radiative Recombination
ROI	Region of Interest
RCI	Relativistic Configuration Interaction
SAS	Science Analysis System
SDD	Silicon Drift Detector
SED	Spectral Energy Distribution
SNR	Supernova Remnant
SXS	Soft X-ray Spectrometer
UHV	Ultra-High Vacuum
ULX	Ultra-Luminous X-ray Source
UV	Ultraviolet
TES	Transition-Edge Sensor
TMP	Turbomolecular Pump
TTS	T Tauri Star
WHIM	Warm-Hot Intergalactic Medium
X-IFU	X-ray Integral Field Unit
XMM	X-ray Multi-Mirror Mission
XRIB	X-ray Binary
XRISM	X-ray Imaging and Spectroscopy Mission

Chapter 1: Introduction

1.1 History of X-ray Spectroscopy

The concept of energy forever changed in 1895 when German scientist Wilhelm Conrad Roentgen first observed and documented an unknown type of radiation that was released as experimental discharge from a gas-filled tube ([Ames, 1896](#)). He discovered that firing streams of this radiation through an organism's arms and hands created detailed images of the bones inside. Unable to explain its physical nature, Roentgen coined this phenomenon as "X"-ray radiation. This energy proved to be pivotal in the field of medicine, as the advent of X-ray imaging machines enabled the clinical diagnosis of bone fractures and diseases ([Tubiana, 1996](#)).

The fields of astronomy and physics would also expand considerably from the discovery of this radiation. The first hint of the existence of cosmic X-rays came in 1949, when radiation detectors onboard rockets were launched above the atmosphere where they detected X-rays in the form of photons, or particles of light, coming from the Sun ([Friedman et al., 1951](#)). This proved to be just a preview of the Universe's high-energy environment, as a decade later a detector was launched on an Aerobee sounding rocket and discovered X-ray radiation coming from Scorpius X-1 using small-aperture Geiger counters ([Giacconi et al., 1962](#)), which is now confirmed as the extrasolar X-ray source with the strongest apparent brightness ([Chen, 2017](#)). This technique signaled the requirement for space-based X-ray detectors, as most X-ray radiation is absorbed

by Earth's atmosphere. It also highlighted the need for more sophisticated detection methods, as the limited observing time of this method made the identification and analysis of the observed objects' nature very difficult.

In order to unravel detailed physical conditions of these celestial objects, astronomers developed technology in the form of satellite spectrometers to detect X-ray photons and retrieve their spectral information. Spectral emission lines are produced when transitions of electrons from upper to lower energy levels occur in specific elements, and the energy of the line center indicates the level transition of the particular element involved. From these spectral lines, it is possible to determine the elemental abundance, temperature, and other physical properties of the observed objects. By collecting and modelling this information, the formation, evolution, and interactions of X-ray emitting sources throughout the visible Universe can then be described.

The first satellite launched for the purpose of X-ray observations was the *Uhuru* X-ray Explorer Satellite in 1970 (Giacconi et al., 1971b). *Uhuru* was responsible for performing the first mapping survey of the X-ray sky. *Uhuru* made use of proportional counters as detectors, which detect X-ray radiation through high density xenon gas ionization (Glasser et al., 1994). In addition to its all-sky survey, the most prominent achievements of *Uhuru* were the discoveries of the X-ray binary (XRB) systems Centaurus X-3 (Giacconi et al., 1971a), Hercules X-1 (Schreier et al., 1972), and Vela X-1 (Kellogg et al., 1973), which are binary star systems luminous in the X-ray regime that typically consist of a neutron star orbiting a main-sequence or supergiant star. *Uhuru* was also used to discover Cygnus X-1 (Oda et al., 1971), and its observations were instrumental in the confirmation of the object as the first discovered black hole.

The *Einstein* observatory (Giacconi, 1980) was the next major satellite launched in 1978 with a primary focus on extrasolar X-ray observations. *Einstein* was the first mission to utilize

high-resolution focusing optics for observations, making use of the first space-based fully imaging X-ray telescope as well as a high-resolution mirror assembly and imager, imaging proportional counter, and three separate spectrometers: a solid state spectrometer, focal plane crystal spectrometer (FPCS), and objective grating spectrometer (OGS). The proportional counter enabled a wider field-of-view (FOV) and moderate energy resolution to allow the detection of fainter sources. The FPCS and OGS enabled images of both point-like and extended sources, while the low-throughput spectrometers offered the first opportunities for high-resolution spectroscopic analysis of extrasolar X-ray sources. However, the FPCS and OGS were not very sensitive with an effective area of order $0.1 - 1 \text{ cm}^2$, and thus were most useful for the brightest X-ray sources such as XRBs (Vrtilek et al., 1991). The mission was also responsible for the first high-resolution spectral studies of supernova remnants (SNRs) including Cassiopeia A (Murray et al., 1979). Despite its shortcomings, the overall success of *Einstein* demonstrated that X-ray spectroscopy missions were just as vital to the field of astrophysics as missions focused on the optical and ultraviolet wavebands (Clark, 1982).

The advent of diffraction grating spectrometers onboard the *Chandra* X-ray Observatory (Weisskopf et al., 2000) and the *X-ray Multi-Mirror Mission (XMM-Newton)* Observatory (Jansen et al., 2001), both launched in 1999, provided the greatest advancement of the field to date. *Chandra* carries both the High Energy Transmission Grating Spectrometer (HETGS) and Low Energy Transmission Grating Spectrometer (LETGS), covering an energy band of 0.1 - 10 keV, and enabling a $\sim 0.5''$ spatial resolution as well as a spectral resolving power of $R \sim 1000$. The spectral images are readout by its focal plane imaging detectors for each individual photon. *Chandra* is equipped with two primary imaging detectors: the Advanced CCD Imaging Spectrometer (ACIS) composed of silicon charge-coupled device (CCD) cameras

that convert incoming X-rays to photoelectrons in order to measure the photon energy, and the High Resolution Camera (HRC) consisting of microchannel plates (MCP) which amplify photon signal and provide spatial information to construct detailed maps of the observed source. Similarly, the *XMM-Newton* mission is equipped with the the European Photon Imaging Camera (EPIC) and Reflection Grating Spectrometer (RGS) to achieve high-resolution spectroscopy. EPIC, which is composed of two metal-oxide-silicon CCD arrays and one pn CDD with a different chip geometry, takes advantage of the full 0.2 – 12 keV energy range of *XMM-Newton*'s mirrors as well as a moderate angular resolution of $\sim 6''$ (Strüder et al., 2001). The RGS, which covers an energy range of 0.3 – 2.5 keV, consists of arrays of grazing incidence reflection grating plates to produce large dispersion at the plate groove densities, in order to match the instrument's angular resolution. The RGS provides slightly lower spatial resolution and spectral resolving power compared to *Chandra*, but provides a much higher throughput with an effective area of $\sim 1500 \text{ cm}^2$ at 1 keV (Jansen et al., 2001). The grating spectrometers for both missions are subject to spectral / spatial confusion for extended sources (Flanagan et al., 2003). However, because of its superior angular resolution to *Chandra*, the RGS is better equipped to produce high-resolution spectra of extended objects, which is advantageous for observations of galaxy clusters, supernova remnants, and elliptical galaxies (Kaastra, 2017).

These specifications have enabled a plethora of key discoveries and studies by both missions (Paerels & Kahn, 2003; Santos-Lleo et al., 2009; Wilkes et al., 2022). Some of the most prominent achievements by *Chandra* include the detection of the resolved structure of the Cassiopeia A supernova remnant (Weisskopf & Hughes, 2006), the accretion of protoplanetary disk material onto T Tauri stars (TTS) (Kastner et al., 2002; Brickhouse et al., 2009), resolved X-ray jets in galactic and extragalactic sources (Schwartz, 2010), and outflows from ultra-luminous

X-ray sources (ULXs) (Pinto et al., 2016). *XMM-Newton* is responsible for the major discovery of the lack of cool X-ray emitting gas in the cores of galaxy clusters (Tamura et al., 2001a,b; Peterson et al., 2001; Kaastra et al., 2001; Sakelliou et al., 2002). *XMM-Newton* also enabled the discovery of an abundance anomaly in the stellar coronae of cooler stars known as the inverse first-ionization potential effect, a new class of Type 1 supernovae with young and massive progenitors, and unresolved inner shell lines from low iron charge states in AGN outflows (Sako et al., 2001).

Several advancements were expected with the ill-fated *Hitomi* mission (Takahashi et al., 2016) launched in 2016, which was equipped with a wide-band microcalorimeter as the detector (Kelley et al., 2016; Porter et al., 2018). A traditional microcalorimeter consists of a mercury telluride absorber that absorbs incoming X-ray photons through the photoelectric effect, a thermometer that measures the temperature rise of the absorber, and a cryogenically-cooled heat sink that collects the heat and cools the system back down to its equilibrium temperature (Moseley et al., 1984; McCammon, 2005). Microcalorimeters achieve better broadband width and higher efficiency than grating spectrometers. Having high-resolution spectra for both point sources and spatially extended sources enabled by its soft X-ray spectrometer (SXS), a calorimeter array, *Hitomi* was able to determine the most accurate measurement to-date of the velocity turbulence in the Perseus cluster by measuring spectral line broadening (Hitomi Collaboration et al., 2018). The instrument also enabled high spectral resolution of iron transition lines for both clusters and point sources, as well as broadband sensitivity over the 0.3 - 100 keV band (Kaastra, 2017). However, these strengths could not be realized due to the abrupt end of the mission.

Spectroscopic efforts will continue to advance with the *X-Ray Imaging and Spectroscopy*

Mission (XRISM) recently launched in 2023. *XRISM*'s Resolve detector is a microcalorimeter array that delivers a ≤ 5 eV FWHM energy resolution in the 0.3 - 12 keV bandpass (Tashiro et al., 2018). The future *Athena* mission will achieve an even better energy resolution of ~ 2.5 eV FWHM with its X-ray Integral Field Unit (X-IFU) transition-edge sensor (TES) calorimeter (Barret et al., 2016), as well as an improved angular resolution of $5 - 10''$ and a larger total number of pixels, which will all improve the imaging capabilities. *XRISM* and *Athena*'s capabilities will enable the detection of even fainter lines than those observed by *Chandra*, *XMM-Newton*, and *Hitomi*.

1.2 Atomic Processes in X-ray Spectra

Spectrometers have proven to be effective probes of astrophysical plasmas from which the X-ray photons originate. The Universe is filled with a variety of forms of ionized plasma which accounts for most cosmic baryonic matter (Ezoe et al., 2021). 80% of the baryons in the visible Universe are considered to reside in hot plasmas (Fukugita et al., 1998) in the form of highly charged ions, primarily residing in and around stars, galaxies, and clusters as well as the photoionized intergalactic medium and circumgalactic medium (Shull et al., 2012; Hitomi Collaboration et al., 2017). Extreme objects in the Universe such as white dwarfs, neutron stars, and supermassive black holes are studied by observing the plasmas which fall into or flow out from their deep potential wells.

In order to interpret the X-ray spectra of these objects, the emission and absorption mechanisms occurring in the plasmas must be understood. The spectra of optically thin plasmas, meaning plasmas with low optical depths in which the probability of photons being scattered or

absorbed are low, consist of both line and continuum components ([Mewe, 1999](#)). Continuum X-ray emission is primarily generated via a process called bremsstrahlung ("braking radiation"), caused by deceleration of an electron in the electrostatic field of an ion

$$X^{q+} + e^{-}(E_0) \rightarrow X^{q+} + e^{-}(E_1) + \gamma \quad (1.1)$$

where X represents the ion, q represents the charge state, e^{-} represents the electrons, γ represents the released photon, and E_0 and E_1 represent the kinetic energies of the electron before and after the collision respectively. To satisfy energy conservation, the electron's kinetic energy loss from the deceleration is released back into the system as a photon. Since the deceleration of the electron can vary continuously, the energy of the emitted photons can also vary continuously, resulting in the X-ray emission having a distribution of photon energies and thus a continuum spectrum. Bremsstrahlung is dominant at higher temperatures of a few keV where line emission is much weaker, as abundant elements are mostly fully ionized. For further reading on bremsstrahlung, see [Rybicki & Lightman \(1979, Chapter 5\)](#).

X-ray line spectra are produced by transitions of electrons from high to low levels of highly charged ions. Most observable ion spectral lines in the high-energy regime appear in X-ray spectra as a result of transitions into the K ($n = 1$) and L ($n = 2$) electron shells, which are the two closest shells to the nucleus and require the most energy to excite or ionize. X-ray spectra from celestial objects contain an abundance of spectral lines from highly charged ions, which provide valuable plasma diagnostics to probe a range of astrophysics. However, understanding the atomic physics underlying X-ray emission and absorption is imperative for robust interpretation of the spectra. All relevant atomic processes that could be populating or de-

populating a spectral line must be accounted for. These processes primarily consist of radiative decay, excitation, ionization, and recombination.

1.2.1 Radiative Transitions

Emission lines are formed when a system undergoes radiative decay, in which an electron in an excited state drops down to a lower energy level and the energy is released as a photon. The two predominant decay mechanisms are known as stimulated emission and spontaneous emission of photons. Stimulated emission occurs when an excited ion is exposed to a photon with resonant energy, which causes the upper state to decay. The excited ion can also decay back to the ground state by means of spontaneous photon emission. The probabilities of these mechanisms are defined by the Einstein coefficients of stimulated emission B_{ul} and spontaneous emission A_{ul} respectively, where u and l refer to the upper and lower levels involved.

Absorption lines are formed when X-ray photons from a hot plasma pass through a cooler component along the observer line-of-sight. As a result, the observed radiation flux is reduced due to the photons being absorbed and re-emitted in random directions. The probability of this mechanism is defined by the Einstein coefficient of photon absorption B_{lu} , as the inverse process of stimulated emission.

For excited ions having multiple decay mechanisms, the relative intensities of the competing decays are called branching ratios. Each ratio is a measure of the probability that a particular decay path will occur, and therefore the sum of branching ratios for an ion equals one.

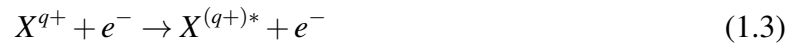
A useful parameter that can be derived from the decay mechanisms is the oscillator strength, which is proportional to the Einstein coefficient of spontaneous emission A_{ul} as

$$f_{lu} = \frac{g_l}{g_u} \frac{2\pi\epsilon_0 m_e c^3}{\omega_{ul} e^2} A_{ul} \quad (1.2)$$

where g_l and g_u represent the degeneracy levels of the lower and upper (excited) states respectively, ϵ_0 represents the electric constant, m_e represents the electron mass, e represents the electron charge, and ω_{ul} represents the oscillation frequency. Both oscillator strengths and branching ratios are important parameters for determining transition probability estimations in astrophysical plasmas.

1.2.2 Excitation

Collisional excitation (CE) is the process where an electron or ion collides with an atom or molecule and the collision causes an increase in the internal energy of the ion. This subsequently leads to a bound electron in the ion being excited from one level to a higher one. In the case of direct electron-impact excitation (DE), the ion interacts with a free electron with a discrete kinetic energy and part of the kinetic energy is transferred to the ion. This process can be denoted as



where $X^{(q+)*}$ represents the excited state of the ion. The electron energy of the incident electron after the collision is equal to its original kinetic energy minus the energy difference between the final and initial states of the bound electron. The top panel of Figure 1.1 shows a diagram of the DE process. DE is the dominant line formation process in collisional plasmas which are further discussed in Section 1.2.6. The inverse of this process is collisional de-excitation, in which the

electron radiatively decays back to its original state and a photon is subsequently emitted, thus leading to line formation.

An atom or ion may also be excited by photon absorption in a resonant process called photoexcitation. In this process, a bound electron is resonantly excited by a photon if the energy of the incoming photon matches the difference between the final and initial state of the bound electron. The bottom panel of Figure 1.1 shows a diagram of the photoexcitation process. This process can be denoted as



Resonant excitation (RE) describes a situation following a process known as dielectronic capture, in which the capture of a free electron by an ion with the simultaneous excitation of a bound electron gives rise to a doubly excited quasi-bound state. One of the electrons is subsequently ejected through autoionization (described in Section 1.2.3) and the other decays to a lower lying excited level, thus leaving the ion in an excited state. Because it is a resonant process, the bound electron can only be excited to an upper level if the energy of the captured electron equals the difference between the lower and upper energy levels. Figure 1.2 shows a diagram of the RE process.

1.2.3 Ionization

In the process of collisional ionization (CI), a free electron inelastically collides with the bound electron of an atom. If the kinetic energy of the colliding electron exceeds the binding energy of the bound electron, the latter is emitted from its shell and the atom becomes positively

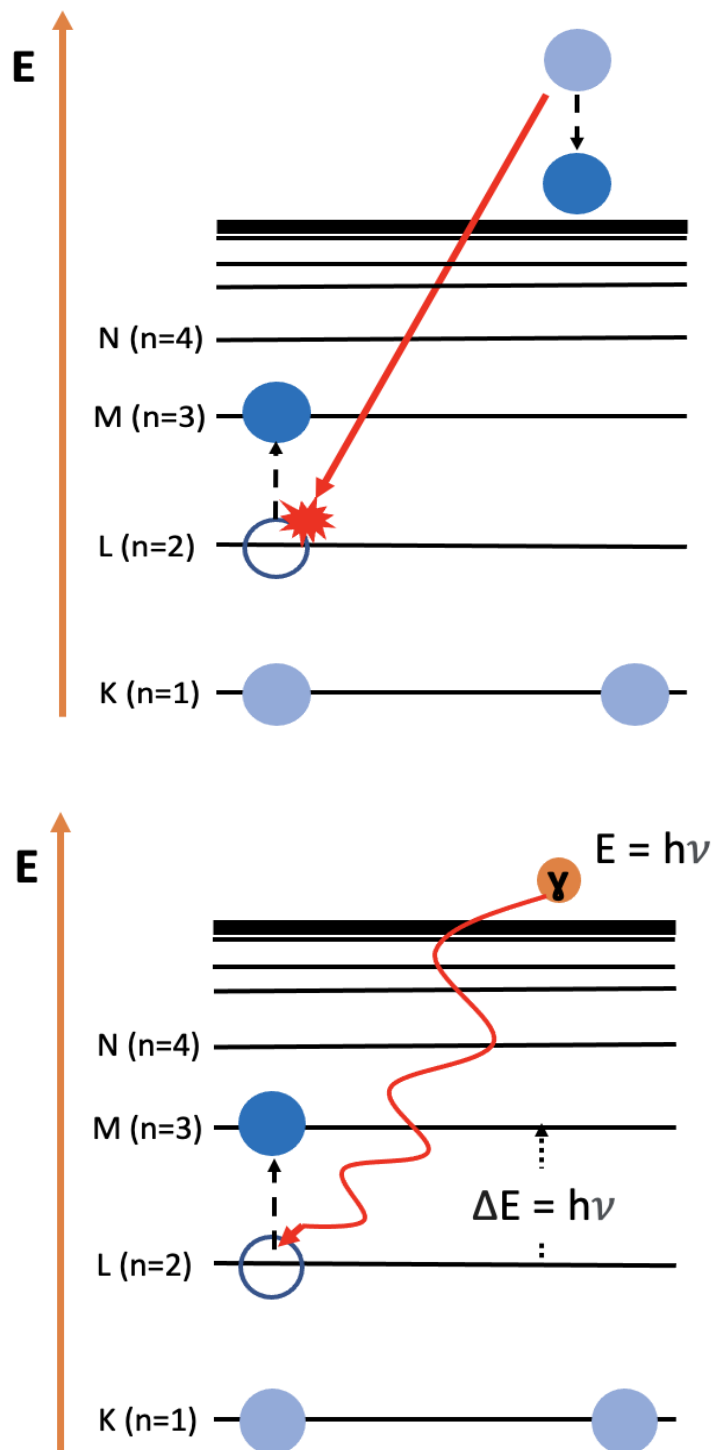


Figure 1.1: **(Top)** Direct electron-impact excitation (DE) process. An free electron collides with a bound electron in the L ($n = 2$) shell, which excites the bound electron to the M ($n = 3$) shell. The free electron loses an equivalent amount of kinetic energy in the collision. **(Bottom)** Photoexcitation process. A photon is absorbed by a bound electron in the L shell, which excites it to the M shell. Since it is a resonant process, the photon has the same amount of energy as the transition.

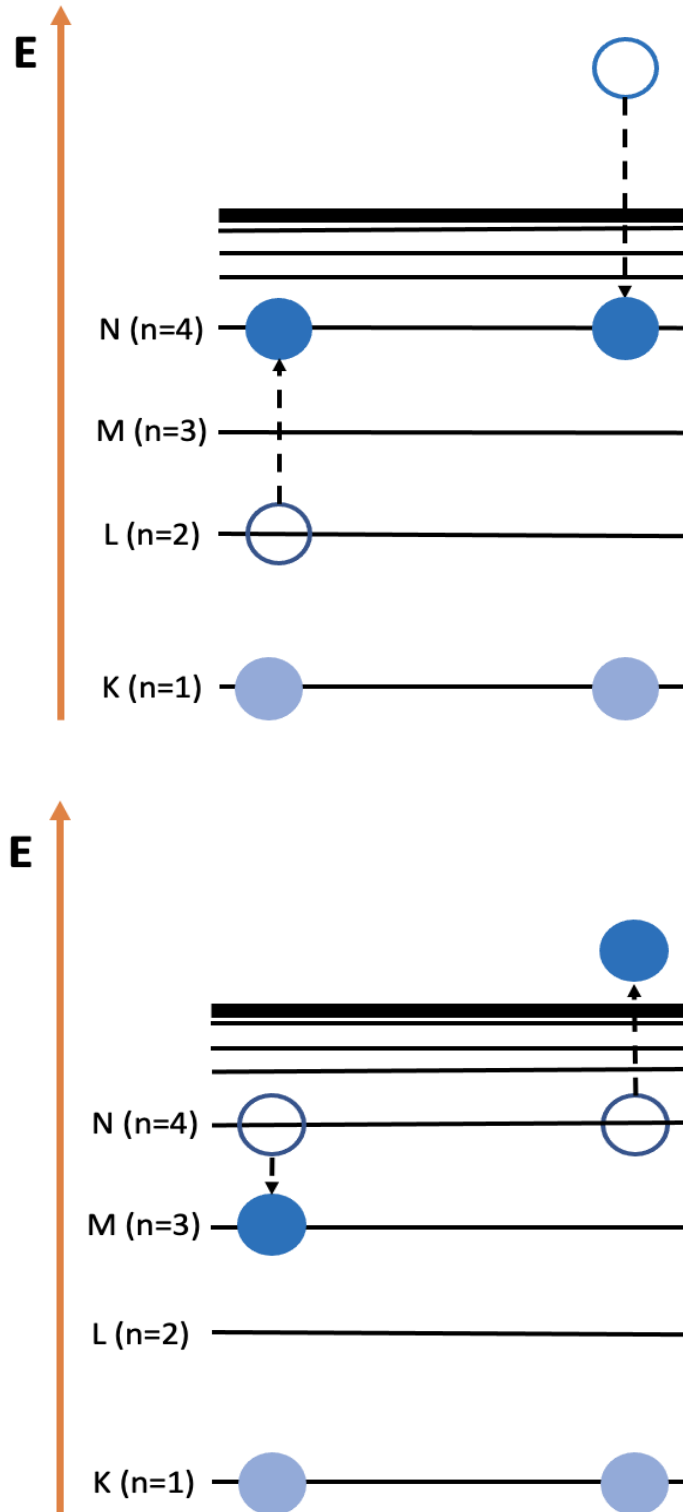
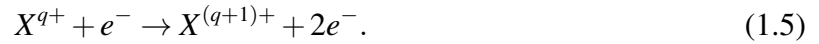


Figure 1.2: **(Top)** Resonant excitation (RE) process beginning with dielectronic capture, in which a free electron is captured into the N ($n = 4$) shell while a bound L ($n = 2$) shell electron is simultaneously excited to the N shell. **(Bottom)** One of the electrons is then ejected through autoionization and the other decays down to the M ($n = 3$) shell.

ionized. The top panel of Figure 1.3 shows a diagram of the CI process. The process occurs as



An atom or ion can also be ionized by means of photoionization, which occurs when a photon transfers its energy to a bound electron, which ejects the electron and leaves the ion in an excited state



Similar to electron-impact ionization, this process only occurs if the energy of the photon exceeds the binding energy of the bound electron. The difference between the photon energy and the binding energy of the electron is transferred to the now freed electron, resulting in additional kinetic energy. The bottom panel of Figure 1.3 shows a diagram of the photoionization process.

An ion in an excited state may undergo the process of autoionization (AI), in which an outer-shell electron is spontaneously emitted. AI also occurs during the two-step process of Auger decay, which occurs when an inner-shell electron is ionized and a bound outer-shell electron rapidly fills the electron hole. The energy difference is then non-radiatively transferred to a second bound electron, which gets autoionized from the system. This process can only occur when the interaction energy exceeds the inner-shell excitation threshold. The released energy can also be emitted as a photon in the process known as fluorescence.

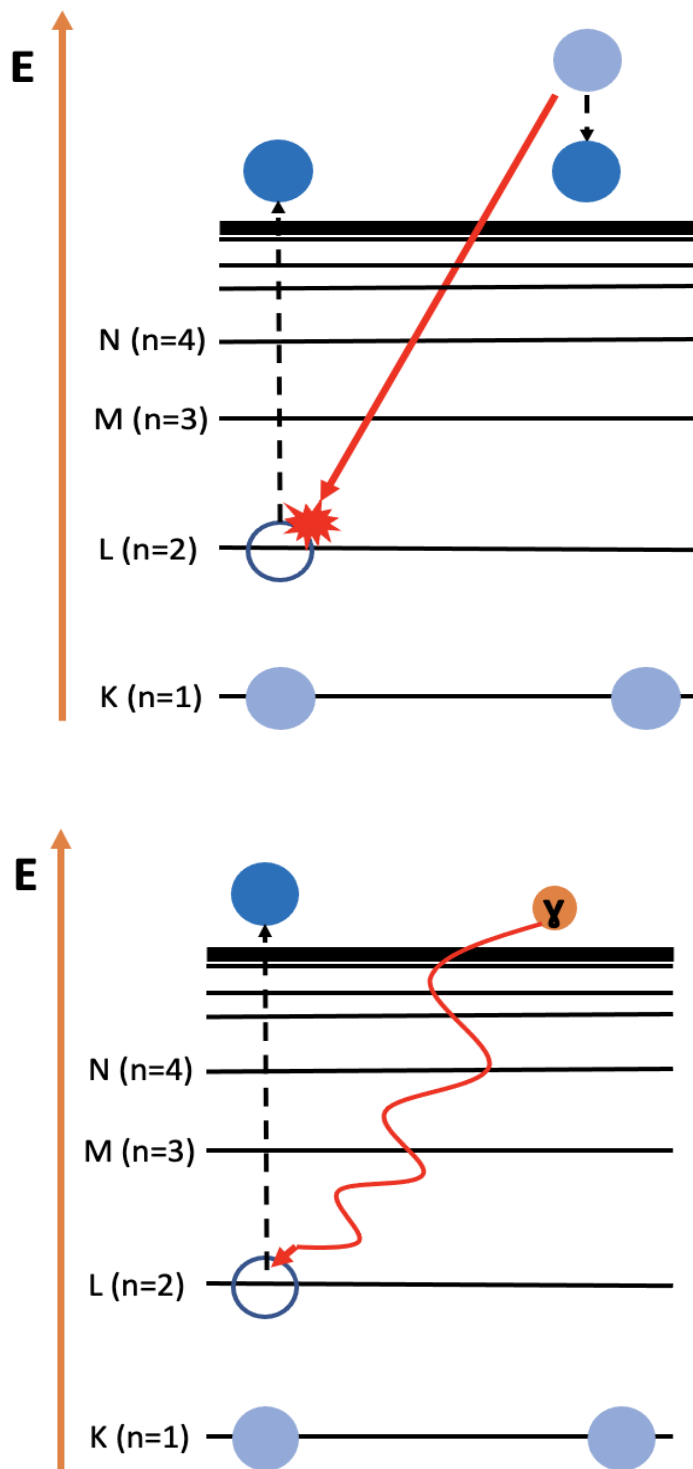


Figure 1.3: **(Top)** Collisional ionization (CI) process. An free electron collides with a bound electron in the L ($n = 2$) shell, causing the bound electron to be ejected from the atom. **(Bottom)** Photoionization (PI) process. A photon is absorbed by a bound electron in the L shell, which ejects the electron.

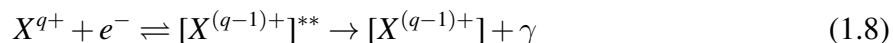
1.2.4 Recombination

Recombination is the inverse process of ionization, in which a free electron is captured into a vacant shell of an ion. There are two predominant recombination processes: radiative and dielectronic. Radiative recombination (RR) takes place when an ion captures an electron into one of its bound orbits with a simultaneous photon emission. It is the inverse process of photoionization. This process is represented as



Dielectronic recombination (DR), which is the inverse of autoionization, refers to a two-step resonant process in which dielectronic capture is followed by radiative decay, emitting a photon and producing a satellite line. This line will have a slightly lower energy than the main "parent" lines due to the perturbation caused by the added spectator electron ([Dubau & Volonte, 1980](#)). Figure 1.4 shows a diagram of the DR process.

The DR process is represented as



where $[X^{(q-1)+}]^{**}$ represents the intermediate doubly excited state and $[X^{(q-1)+}]$ represents the ion after recombination. The DR process is very similar to radiative recombination, however it is a resonant process and can only take place if the free electron captured has the exact energy (sum of kinetic and binding energy) required to promote the core electron. In contrast, radiative recombination involves a continuous distribution of free-electron energies.

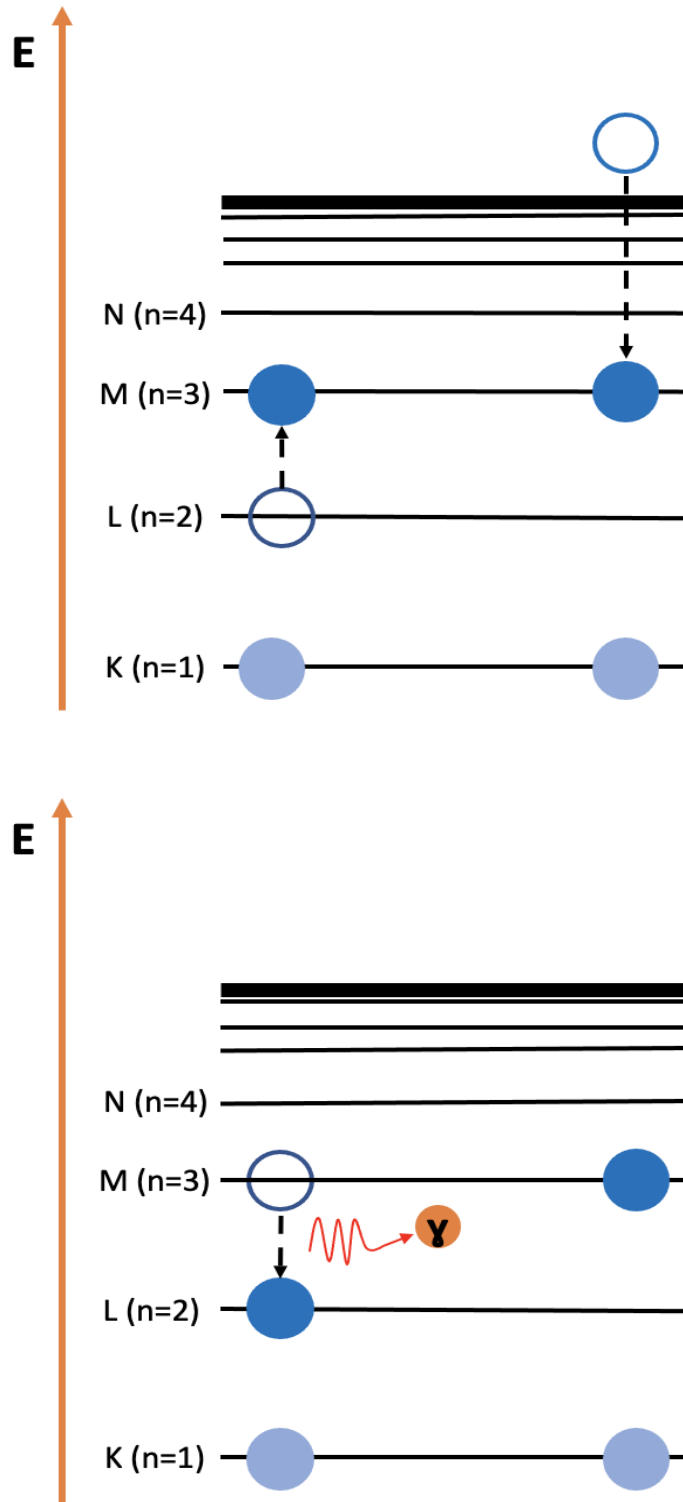


Figure 1.4: **(Top)** Dielectronic recombination (DR) process beginning with dielectronic capture, in which a free electron is captured into the M ($n = 3$) shell while a bound L ($n = 2$) shell electron is simultaneously excited to the M shell. **(Bottom)** One of the M shell electrons then recombines and a photon is emitted.

1.2.5 Cross Sections and Rate Coefficients

The probability of the level-populating processes described above is measured by their cross sections, which is defined as the ratio of the event rate per target particle to the incident particle flux. A cross section σ has units of area (cm^2) and can be interpreted as the size of the object that the incident particle must hit in order for the process to occur. It is possible to measure the differential cross section, meaning the ratio of the event rate per target particle in a given direction ($d\sigma / d\Omega$), or the total cross section integrated over all scattering angles. These processes primarily depend on the interaction energy of the electron-ion collision, which drives the formation of the spectral line. The cross section for each process has its own dependencies, i.e. the kinetic energy of the free electron, binding energy of the bound electron, energy of initial and excited ion state, etc.

For plasma diagnostics, it is convenient to describe cross sections with rate coefficients, which are resonant strengths integrated over a Maxwellian distribution of collision energies. These coefficients (in units $\text{cm}^3 \text{s}^{-1}$) are defined as

$$\alpha_i = \int_{E_0}^{\infty} v \sigma_i f(E, T_e) dE \quad (1.9)$$

where v represents the electron velocity, σ_i represents the interaction cross section for process i , E_0 represents the threshold energy for the process i to occur, T_e is the electron temperature, and $f(E, T_e)$ represents the Maxwellian velocity distribution which is typically represented as

$$f(E, T_e) dE = \frac{2}{\sqrt{\pi}} \left(\frac{E}{kT_e} \right)^{3/2} \frac{e^{-E/kT_e}}{\sqrt{E}} dE. \quad (1.10)$$

By calculating rate coefficients, a useful diagnostic is obtained for spectral modelling as well as estimations for electron density and temperature under different plasma conditions.

For further reading on atomic processes as well as derivations of cross section and rate coefficient equations, see [Raymond & Brickhouse \(1996\)](#) and [Mewe \(1999\)](#).

1.2.6 Astrophysical Plasmas

Observations have revealed that X-ray radiation is produced in either thermal or non-thermal processes depending on the nature of the energy of electrons involved in the relevant process ([Mewe, 1999](#)). Thermal processes depend purely on the temperature of the emitting source, and the energy of the electrons can be described by a Maxwellian distribution. Non-thermal processes such as synchrotron radiation, which is emission from charged particles accelerating in a magnetic field, do not depend on the temperature of the emitting source and typically produce featureless power-law spectra. Thermal X-ray emitting plasmas, which are abundant in intermediate-Z metals such as nickel and iron, show spectral line emission features that can be analyzed to reveal their temperatures, velocity structure, and chemical composition. The most common types of plasmas are either 1) photoionized, in which photoionization is the dominant process and the external radiation field is strong enough to affect the plasma's energy balance and ionization structure, or 2) collisional if collisions between electrons and ions are dominant processes.

A photoionized plasma has a strong and ambient radiation field which leads to photoionization being the dominant ionization mechanism, and in the case of photoionization equilibrium, a balance between radiative cooling and photoelectric heating. In this type of

plasma, the equilibrium temperature and the degree of ionization are dependent on an ionization parameter ξ given by the ratio of radiation flux to the particle (electron + ion) number density. Excited levels are populated by photoexcitation from ground, and to a lesser degree, from radiative recombination and radiative cascades following recombination onto higher levels.

This plasma type is assumed to apply for accretion-powered sources. An example is X-ray binaries (XRBs), in which the accretors are neutron stars or stellar mass black holes. The accretion disk of XRBs are theorized to radiate thermal emission, which then photoionizes plasma in the observer line-of-sight. Another source is cataclysmic variables (CVs), in which the X-ray accretors are white dwarfs. High-resolution X-ray spectra have also demonstrated the presence of photoionized plasma in the emission regions of active galactic nuclei (Kinkhabwala et al., 2002).

In contrast, a collisional plasma has a weak radiation field and as a result, electron-ion collisions dominate the level-populating processes. In this case, both the ionization and steady-state level populations are directly dependent on electron temperature. Additionally, the plasma is assumed to be optically thin to its own radiation, and therefore scattering and absorption processes are assumed negligible. Many well-studied X-ray emitting plasmas are collisionally ionized and have no strong central continuum emission to affect their thermal states. These plasmas, which dominate the X-ray spectra of supernova remnants (SNR), stellar coronae, the interstellar medium (ISM) of elliptical and spiral galaxies, and galaxy clusters, have temperatures in the range of $10^6 - 10^8$ K.

The electron temperature in collisional plasmas is comparable to the ionization potential for the most abundant ions, which is the energy required to remove an electron from the ion. This property differs significantly from photoionized plasmas in which the electron temperature is typically much lower as a result of the stronger radiation field. A useful method to distinguish

these two plasma types in X-ray spectra is to observe their radiative recombination continua (RRC), which indicates the electron energy distribution in the plasma. The characteristic width of the continua can be estimated as $\sim k_B T_e$, where k_B represents the Boltzmann constant and T_e represents the electron temperature. For a collisional plasma, $k_B T_e$ scales approximately with the ionization threshold energy χ of the most abundant ions, whereas for a photoionized plasma $k_B T_e \ll \chi$ (Kahn et al., 2002).

In rare cases, an X-ray emitting plasma may also be in local thermodynamic equilibrium (LTE) in which the excited states of the ions are populated statistically at a local temperature. In this scenario, the rates for excitation processes are on the same scale as de-excitation rates, meaning particle collisions occur rapidly and the distribution responds immediately so that equilibrium holds. This state simplifies level population computations for simulations of spectra, but requires a sufficiently high electron density and all radiative processes to be negligible. This assumption is not valid for most X-ray emitting plasmas due to the high radiative decay rates of transitions (Kahn et al., 2002). Assuming LTE would require electron densities of $n_e \geq 10^{24} \text{ cm}^{-3}$ (Apruzese et al., 2002). Because of this, calculations and interpretations of spectral emission from plasmas must be based on accounting for all processes that populate and depopulate a given energy level.

1.3 Spectral Line Diagnostics

The emission lines from highly charged ions are valuable as diagnostics for key astrophysical plasma parameters. Transition probabilities are determined by electron quantum states, which are significantly dependent on plasma conditions including electron temperature,

electron density, and ionization balance. As a result, spectral lines are probes for these physical conditions. Since plasma ionization balance is dependent on temperature, the detection of a spectral line itself can imply the existence of plasma near the temperature where the ion is preferentially formed. The detection of multiple ion charge states from a single element is also useful for determining the plasma ionization distribution, which is a key independent diagnostic for total column density.

Intrinsic characteristics of the spectral lines also have major diagnostic utility. The strength of the line is useful to determine conditions such as degree of ionization, temperature, and density as well as elemental abundance and optical depth. For example, the Fe $K\alpha$ lines, which are some of the strongest in the X-ray regime and are further discussed in Section 1.6, were utilized to prove the existence of resonant scattering in the Perseus cluster core by using the ion's spectral line strengths as a diagnostic (Hitomi Collaboration et al., 2018). The study measured the suppression of the flux in the Fe XXV resonance line at 6.7 keV in the center of the cluster, which was attributed to photons having been scattered out of the line-of-sight. Since optical depth at line center depends on turbulent Doppler broadening, the comparison of fluxes between the optically thin Fe XXV forbidden line and optically thick Fe XXV resonance line was also used to measure the characteristic amplitude of gas velocities in the intracluster medium (ICM).

Line width can also be used as a diagnostic of velocity turbulence, as the degree of Doppler broadening is directly proportional to the width of the velocity distribution (Rudge & Raine, 1999; Rebusco et al., 2008). This is because X-ray photons emitted by a moving source relative to the observer point-of-view are subject to Doppler shift. Radiation emitted from a star will be broadened as a result of velocity line-of-sight variations on opposite sides of the star due to rotation. Line width can also be used to measure the kinetic temperature of gas, as atoms will be

moving at faster velocities in hotter gas, and thus the spectral lines will appear broader.

Line shifts, which are wavelength displacements of spectral lines away from the positions expected from cosmic redshift or the Doppler shift caused by radial motion ([Dravins, 2003](#)), can also be used as a diagnostic of the kinematic properties of the observed source. The degree of the shift depends on the relative velocity between the source and observer. Deriving velocities from line shifts has enabled the detection of outflows from AGN and supernovae feedback, as well as the radial profile of galactic rotation curves ([ZuHone et al., 2024](#)).

For the typical temperatures of X-ray emitting plasmas, the most abundant elements are found in their hydrogen-like (one electron) or helium-like (two electrons) charge states. Most H-like lines consist of Lyman series transitions, which are produced through electric dipole transitions. An electric dipole transition occurs when an electron jumps from the ground state to the first excited level in an ion. These transitions are the dominant effect resulting from the interaction between an electron and a charged particle, and the direct result is the emission of a photon. H-like lines from the abundant elements, including carbon, nitrogen, oxygen, silicon, sulfur, calcium, iron, and nickel, are found from 0.2 – 8 keV ([Kahn et al., 2002](#)). These transitions have high radiative decay rates and negligible collisional line mixing, giving them limited use as temperature and density diagnostics. However, the lines are typically some of the brightest in the X-ray regime and have proven useful as diagnostics for elemental abundance and velocity ([Rasmussen et al., 2001](#)).

He-like lines have proven to be particularly valuable diagnostics for electron density, temperature, and ionization conditions of emitting plasma ([Gabriel & Jordan, 1969](#)). The most important transitions are denoted as: the resonance line w ; the intercombination lines x and y ; and the forbidden line z (see Figure 1.6). Resonance lines are produced by an electric dipole

transition, and are typically among the strongest in X-ray spectra. This is due to most electrons in an astrophysical source being in the ground state, and therefore it takes the least amount of energy for them to reach the first excited state. These transitions have selection rules dictating which ones are "allowed" or "forbidden" when an atom switches from one quantum state to another. An intercombination line (semi-forbidden) is an electric dipole transition that changes the total spin of the system. A forbidden line is one that is not allowed by an electric dipole transition, but is produced by a magnetic dipole transition that is caused by the coupling of an electron's magnetic dipole moment to the magnetic field of an interacting electromagnetic wave.

Because these lines have different dependencies on temperature and density, their line ratios are also reliable diagnostics. The use of these diagnostics to determine conditions in X-ray emitting plasmas has proven vital for advancing existing plasma models and subsequently, furthering our knowledge of astrophysical objects. For example, the strength for collisional excitation of the w line increases with temperature in collisional plasmas, while the excitation collision strength for the x , y , and z lines decrease or remain relatively constant. As a result, the line ratio $G = (x + y + z)/w$ can be utilized as a robust diagnostic of electron temperature in collisional plasmas. Similarly, the z line dominates at low electron density but is suppressed as density increases, while the strengths of the x and y lines increase. As a result, the ratio $R = z/(x + y)$ is a useful diagnostic of collisional plasma electron density. Figure 1.5 shows both the electron temperature and density dependencies for the G and R ratios respectively for the He-like ions Ne IX and Mg XI from a study by [Wolfson et al. \(1983\)](#). The line ratios can also serve as a diagnostic of UV photoexcitation, as later explained in Chapter 2. A significant UV radiation field, which is prevalent in the spectra of early-type stars and accretion-powered sources, leads to suppression of the z line and enhancement of the x and y lines ([Mauche et al., 2001](#); [Kahn et al.,](#)

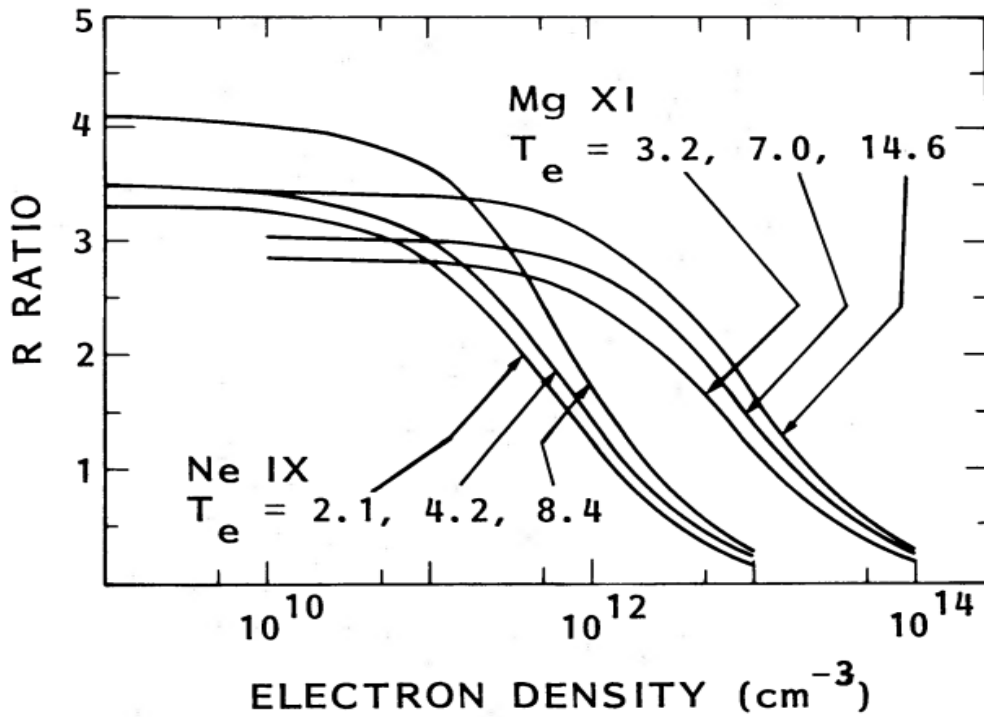
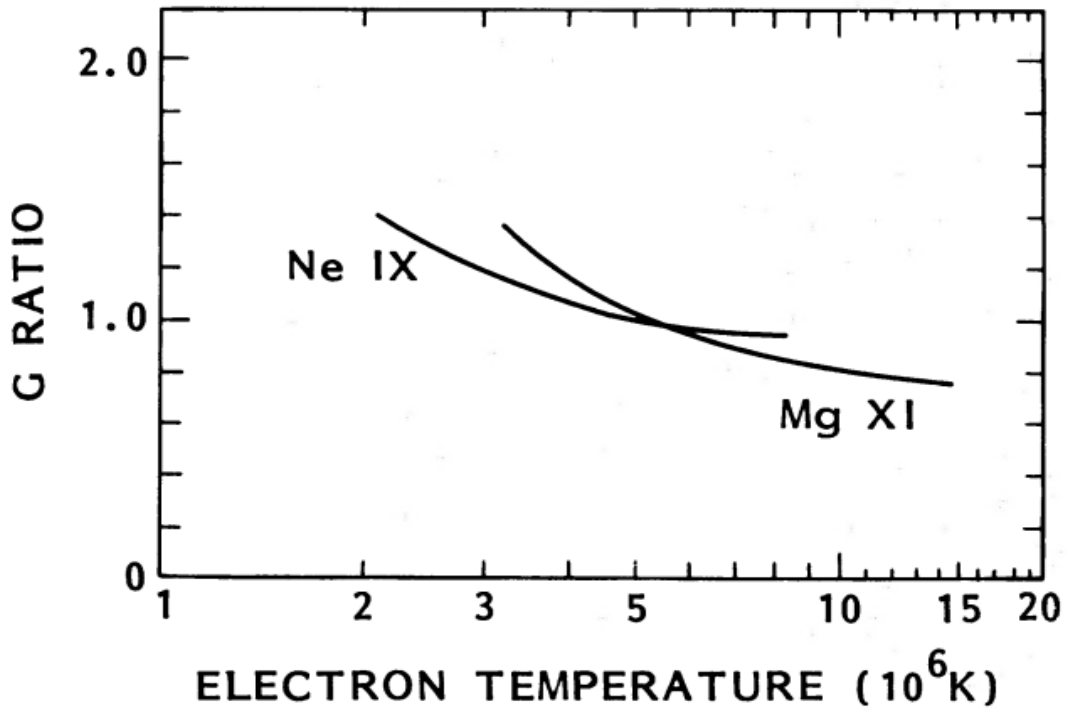


Figure 1.5: (Left) Diagram showing electron temperature dependency of the G ratio for He-like ions Ne IX and Mg XI in collisional plasmas. (Right) Diagram showing electron density dependency of the R ratio for Ne IX and Mg XI ions in collisional plasmas for various electron temperatures. Figures are from [Wolfson et al. \(1983\)](#).

2001a).

Taking ratios of lines originating from different charge states, or two lines from the same ionization stage but with different temperature dependencies, can be also used to infer conditions such as electron temperature. A method devised by [Gabriel \(1972\)](#) found that taking the ratio of the intensity of dielectronic recombination satellite lines relative to the intensity of their associated collisionally excited resonance line yields a robust calculation of electron temperature.

1.4 Theoretical Spectral Modelling

1.4.1 Atomic Structure

Comprehensive modelling of X-ray line spectra requires high-accuracy calculations of atomic structure data, including energy levels, transition energies, cross sections, oscillator strengths, rate coefficients, and polarization. In order to calculate the atomic structure of a system, solutions must be approximated for the Schrödinger equation, which describes how a quantum state evolves over time. The equation is given by

$$\hat{H}\psi(t) = i\hbar \frac{d}{dt}\psi(t) \quad (1.11)$$

where t represents time, the wavefunction $\psi(t)$ is a state vector of the system, \hbar is the reduced Planck's constant representing the quantization of angular momentum, and \hat{H} represents the Hamiltonian (energy) operator describing the total energy of the system. In the case of stationary quantum systems, the Schrödinger equation can be treated as time-independent, such that

$$\hat{H}\psi = E\psi \quad (1.12)$$

where E represents the corresponding eigenvalues of the Hamiltonian, or possible energies that the system could have upon measurement. This form is used to calculate the orbital structure of atoms and ions, as only time-independent equations have the mathematical structure required to produce the discrete spectrum of energy eigenfunctions and eigenvalues. The Hamiltonian can be defined as

$$\hat{H} = \hat{H}_0 + \hat{H}_{elec-elec} + \hat{H}_{s-o} \quad (1.13)$$

where \hat{H}_0 represents the sum of all single electron Hamiltonians, $\hat{H}_{elec-elec}$ represents the mutual electrostatic interaction, or Coulomb repulsion, between electrons, and \hat{H}_{s-o} represents the interactions between spin and orbital angular momenta for each individual electron. As such, the term is denoted as a sum of kinetic, potential, and interaction terms for all involved electrons.

The solutions of the Schrödinger equation for single or multi-electron systems depend on four quantization parameters: 1) the principal quantum number n representing electron shells or energy levels, 2) the orbital quantum number l representing the subshells within each electron shell, 3) the magnetic quantum number m_l representing the orbitals of a given subshell, and 4) the electron spin quantum number m_s . According to the Pauli exclusion principle, no two electrons can have an identical combination of quantum numbers. As a result, the quantum numbers set limits on the number of electrons that can occupy a given state.

The principle quantum numbers n can be labeled as upper-case alphabetic letters starting from K, i.e. K represents the $n = 1$ shell, L represents $n = 2$, etc. The maximum number of

electrons that can fill a shell follows the formula $2n^2$, meaning i.e. the K-shell can hold 2 electrons and the L-shell can hold 8 electrons. The orbital quantum number l is labeled by lower-case alphabetic letters with s, p, d, f, g, \dots representing $l = 0, 1, 2, 3, 4, \dots$ respectively. The number of orbitals in a subshell is determined by the magnetic quantum number m_l , which can range from $-l$ to $+l$ for a given subshell l . The spin of the electrons m_s is an intrinsic property and has two directions, spinning up ($m_s = +1/2$) or spinning down ($m_s = -1/2$). The number of possible values of m_l follows the formula $2l + 1$, and each orbital can contain 2 electrons of opposite spin. Therefore, the s subshell can have only 1 orbital and a total of 2 electrons, while the p subshell can have 3 orbitals and a total of 6 possible electrons. Electrons occupy orbitals in order of increasing energy, meaning (with a few exceptions for transition metals) the higher energy subshells will not be filled until the lower energy orbitals are fully occupied. As an example, a neutral neon atom, which has 10 total electrons, has a configuration of $1s^2 2s^2 2p^6$, as these are the first three orbitals to be filled.

The energy levels of an atom or ion are determined by diagonalizing the total Hamiltonian. The relative strength of $\hat{H}_{elec-elec}$ versus \hat{H}_{s-o} determines how the angular momenta of each electron are coupled together. For structure calculations of multi-electron systems, an appropriate coupling scheme must be utilized, as the energy eigenvalues are dependent on the order in which the angular momenta are added.

Simpler systems with atomic numbers $Z < 30$ are most commonly described using Russell-Saunders coupling, or LS-coupling, which denotes structure with the total orbital angular momentum vector \vec{L} and total spin angular momentum vector \vec{S} (Russell & Saunders, 1925). For these lighter atoms, the interactions between the orbit and spins of individual electrons are much weaker compared to the interactions between the total orbital angular

momenta and total spin angular momenta of all electrons in the atom ($\hat{H}_{elec-elec} \gg \hat{H}_{s-o}$). The total orbital angular momentum vector \vec{L} represents the sum of orbital momenta for all electrons in the atom $\vec{L} = \sum_i \vec{l}_i$. Similarly, the total spin angular momentum vector \vec{S} represents the sum of the spin of each electron in the atom $S = \sum_i \vec{s}_i$. The total angular momentum \vec{J} is taken as the vector sum of \vec{L} and \vec{S} , and these quantum numbers can be combined into the shorthand notation $^{2S+1}L_J$, where $2S + 1$ represents the spin multiplicity of the level, L is the appropriate letter symbol for the total orbital quantum number, and J is the total angular momentum quantum number.

To use helium as an example, the ground state has an electron configuration of $1s^2$. The orbital angular momenta of the two electrons are $l_1, l_2 = 0$, and have spin angular momenta of $s_1 = +1/2$ and $s_2 = -1/2$. Thus, $\vec{L} = 0$ and $\vec{S} = 0$, yielding a LS notation of 1S_0 . The first excited state of helium, which has a configuration of $1s2s$, can have a total spin of $\vec{S} = 0$ or $\vec{S} = 1$ and therefore can have a LS notation of either 1S_0 for $J = 0$ or 3S_1 for $J = 1$. The excited state of helium with a $1s2p$ configuration has a total $\vec{L} = 1$ and possible total spins of $\vec{S} = 0$ or $\vec{S} = 1$, yielding possible combinations of

- $1s2p\ ^3P_0$ for $J = 0$
- $1s2p\ ^3P_1$ for $J = 1$
- $1s2p\ ^3P_2$ for $J = 2$

Figure 1.6 shows a diagram of the possible level transitions between the K-shell and the L-shell for He-like ions with their respective LS notations. The energies of transitions resulting from photoexcitation, represented by the curved arrows, are in the UV regime for astrophysically important ions as further discussed in Chapter 2.

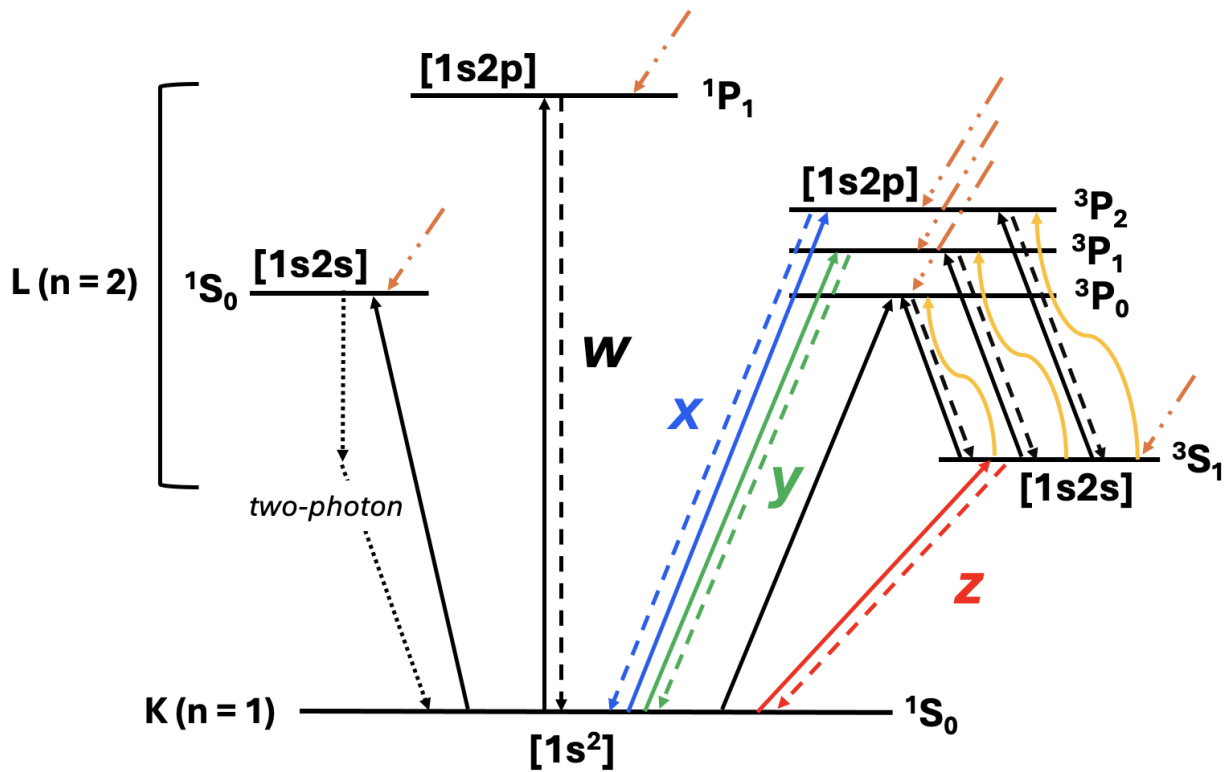


Figure 1.6: Diagram showing possible level transitions for He-like ions, with w , x , y , and z representing the transitions producing the resonance, intercombination, and forbidden lines respectively. Each possible level is labeled with its respective LS notation. The solid lines represent transitions from direct electron-impact excitation, the curved yellow lines represent photoexcitation, the orange dashed lines represent radiative/dielectronic recombination, the broken dotted lines represent decay via two-photon transition, and the dashed lines represent radiative decay.

LS coupling is convenient for simple systems but is not useful for complex ions with multiple electrons, which entail many combinations of quantum numbers for an electron configuration. Additionally, in heavier systems the strength of spin-orbit interactions becomes more comparable, or even more dominant, relative to the strength of electrostatic interactions. Such systems make use of *jj*-coupling, in which the angular momenta \vec{l}_i and \vec{s}_i of each electron couple to a total single angular momenta \vec{j}_i , which vectorially add up to the total angular momentum \vec{J} of the entire system. In this case, each electron's momenta must be individually considered for an accurate assessment of the atom's behavior. Using the same excited helium state with a $1s2p$ configuration as an example, the $1s$ electron yields a total angular momenta $j_1 = |0 \pm 1/2| = 1/2$ and the $2p$ electron yields $j_2 = |1 \pm 1/2| = (1/2, 3/2)$. As a result, the possible combinations from *jj*-coupling are

- $[1s_{1/2}2p_{1/2}]_{J=0}$
- $[1s_{1/2}2p_{1/2}]_{J=1}$
- $[1s_{1/2}2p_{3/2}]_{J=1}$
- $[1s_{1/2}2p_{3/2}]_{J=2}$

For further reading on spectroscopic notation and coupling schemes, see [Condon & Shortley \(1963\)](#) and [Cowan \(1981\)](#).

1.4.2 Plasma Modelling Codes

In order to use spectral lines to infer plasma properties, theoretical models must be derived to try to match the data as closely as possible. The better the fit, the more that can be inferred

from the comparison. However, to try to include every possible atomic process and configuration in a plasma model would be both time consuming and computationally expensive. Therefore, the theoretical models used must make necessary approximations based on plasma conditions in order to calculate level populations. Given their relevance to work in this dissertation, I specifically highlight the widely-used models for collisional plasmas.

There are two main types of collisional plasma models that are used in coding packages for X-ray spectral modelling: Coronal and Collisional-Radiative (CR). In a Coronal plasma, the rate of electron-ion collisions is very low, it is optically thin to its own radiation, and radiative decay is the dominant de-excitation mechanism. This model also assumes the “ground-state” approximation, in which electron density is low enough such that excited state populations are negligible and all ions are assumed to be in the ground state when collisions occur. This model is typically used for spectral analysis of stellar coronae, SNRs, and galaxy clusters ([Mewe, 1999](#)). A Collisional-Radiative (CR) plasma model assumes collisional-radiative equilibrium, meaning the electron-ion collision rate and the rate of photon interactions are equally balanced in terms of de-excitation mechanisms. As a result, a level with a low radiative decay rate may be collisionally de-excited before it can radiate. This model is used to account for all relevant collisional and radiative processes for atomic level population calculations in plasmas for subsequent spectral modelling ([Ralchenko, 2016](#)).

As discussed in the previous section, accurate calculations of atomic structure are necessary for robust theoretical models. This involves solving the time-independent Schrödinger equation by constructing wavefunctions containing information regarding all orbital and spin angular momenta for every individual electron. Aside from the very simplest atoms, the Schrödinger equation cannot be solved analytically. As a result, there have been a multitude of approaches

developed to numerically solve the equation, including the Hartree-Fock method, relativistic configuration interaction (RCI) method, and Many Body Perturbation theory (MBPT). Given its relevance to this dissertation, I highlight the configuration interaction method, which is a widely-used approximation in modern atomic physics codes (Sherrill & Schaefer, 1999). This approach calculates approximate atomic state functions by defining

$$\Psi_i = \sum_{i=1}^n c_i \psi_i \quad (1.14)$$

where Ψ_i is the trial wavefunction represented by a linear combination of configurations ψ_i , each weighted by a mixing coefficient c_i obtained from diagonalizing the total Hamiltonian. The mixing coefficients are optimized while the individual configurations remain the same until the total system energy is minimized. The accuracy of the atomic structure depends on the number of electron configurations included in the calculation.

1.4.3 Flexible Atomic Code

The Flexible Atomic Code (FAC) calculates atomic structure, as well as a wide range of atomic radiative and collisional processes (Gu, 2008). FAC combines the strengths of several existing atomic codes such as HULLAC (Bar-Shalom et al., 2001), ATOM (Amusia et al., 1998), and SZ (Sampson et al., 1989; Zhang et al., 1989) by implementing a fully relativistic approach based on the Dirac equation, which is a generalized form of the Schrödinger equation that takes relativistic effects into account (Dirac, 1928), and the configuration interaction method. FAC also provides a more integrated interface for atomic structure calculations compared to other codes such as SUPERSTRUCTURE (Eissner et al., 1974), multi-configuration Hartree-Fock

(MCHF) (Fischer, 2000), and multi-configuration Dirac-Fock (MCDF) (Grant et al., 1980), by treating both bound-bound and continuum processes within the same program. The code models continuum processes using an approach called the distorted-wave (DW) approximation, which ignores the coupling between resonances and the continuum background and assumes effects from scattering events to be negligible (Mott & Massey, 1933; Madison & Shelton, 1973). The implementation of these approaches enables the ability to efficiently calculate the atomic structure of highly charged ions with high accuracy and reasonable runtime.

FAC computes the atomic structure of the initial, intermediate, and final states of a particular charge state, along with its related transitions. The output data include energy levels, radiative transition rates, collisional excitation and ionization cross sections, photoionization rates, and autoionization rates, thereby enabling the integration of various atomic processes within a single framework. FAC is also equipped with a collisional-radiative model (CRM) that constructs synthetic spectra for plasmas under different physical conditions using atomic data. It calculates level populations for a given temperature and density assuming collisional-radiative equilibrium.

One of the most advantageous aspects of FAC compared to other programs is its user-friendly scripting tools. The python library `pfac` can be used to write scripts with FAC functions in order to derive energy levels and transition rates. By writing a python script, the atom of interest and the desired electron configurations can be specified. FAC then calculates the central potential of the configurations interacting with one another, and diagonalizes the Hamiltonian to calculate atomic structure. The output of this calculation is a list of all possible configurations with specified quantum numbers values as well as the energy of each configuration with respect to the ground state. For every transition, FAC calculates the transition energy, oscillator strength,

decay rate, and multipole expansion. The software package has proven to be robust, as excellent agreement has been found between FAC calculations and both astrophysical data and laboratory measurements (Gu, 2003; Zhong et al., 2004). Most of the new theoretical predictions in Chapters 2 and 3 of this dissertation are based on FAC calculations.

1.5 Laboratory Experiments

Complex plasma models are largely derived from theoretical calculations. However to achieve a reliable scientific interpretation of spectroscopic observations, theoretical calculations must be verified by results obtained from spectroscopic measurements in laboratory experiments. With *XRISM* and *Athena* enabling high-resolution X-ray spectroscopy, it is crucial to have robust atomic data benchmarked by laboratory astrophysics experiments. The most robust approach in spectral analysis is to use atomic data that has already been validated by experiments in plasma models.

However, X-ray line energy measurements for many ion species within databases such as the NIST Atomic Spectral Database (Kelleher et al., 1999), MEKAL (Kaastra et al., 1996a), and AtomDB (Foster et al., 2012) are either unavailable or took place several decades ago (Bearden, 1967), which has resulted in omissions and errors regarding line identification in X-ray spectral observations. For example, a spectral analysis of Procyon by Raassen et al. (2002) from *Chandra* observations was unable to identify an electric-dipole forbidden Ar IX line because of its absence in the published atomic line database compiled by Kelly (1987), instead misidentifying it as a S IX line. Lepson et al. (2003) was later able to correctly identify the line through laboratory measurements of argon charge states. This example highlights the need to measure spectral

lines with better energy resolution and efficiency through advanced laboratory measurements. This enables better model fits to observations and further reduces the uncertainties for derived quantities such as intensity line ratios ([Beiersdorfer et al., 2018](#)), in order to fully maximize their diagnostic use.

Studies finding disagreements of theoretical predictions with laboratory data have shown that both systematic experimental uncertainties and plasma model constraints must also be continually improved. A prominent example of theory-experiment discrepancies is highlighted in [Section 1.6](#) for the $3d$ cross sections of neon-like iron Fe XVII (or Fe¹⁶⁺). Improved experiments are instrumental in the reduction of the systematic uncertainties of diagnostics in analyses of astrophysical X-ray spectra. By improving the constraints on these quantities, the atomic data implemented in the Astrophysical Plasma Emission Code (APEC) ([Smith et al., 2001](#)), SPEX ([Kaastra et al., 1996b](#)), and CHIANTI ([Del Zanna, G. et al., 2015](#)) spectral modeling codes can be further calibrated, which is crucial for interpreting spectroscopic observations with better accuracy.

For a comprehensive explanation of laboratory astrophysics experiments and their applications to X-ray astronomy, see [Beiersdorfer \(2003\)](#).

1.5.1 Electron Beam Ion Trap

One of the most useful instruments developed for the production and study of highly charged ions is the electron beam ion trap (EBIT). An EBIT operates by means of a monoenergetic electron beam that induces a negative space-charge potential ([Levine et al., 1988](#)). This beam is emitted by a cathode mounted inside an electron gun and is guided along

the axis of a set of cylindrical drift tubes until it finally reaches a collector electrode. A magnetic field of increasing strength (in the axial direction) reaches its maximum at the center of the trap, creating a quasi-uniform magnetic field in the central bore and compressing the beam to a sub-millimeter diameter at the trap center. This results in a very high current density that enables efficient ionization and ion trapping (in the radial direction). The electron beam energy is defined by the difference between the potential central drift tube and potential of the cathode.

Neutral atoms are injected into the trap through a differentially-pumped injection system, ionized to high charge states by successive electron impact by the electron beam, and compressed to a sub-millimeter diameter at the trap center by the magnetic field. The resulting ions are radially trapped by the negative space charge of the compressed beam and electrostatically confined in the axial direction by the potential applied to the cylindrical drift tubes. Figure 1.7 show diagrams of the EBIT layout and function.

The cross-sectional area of the drift tubes reshapes the ion trap into a narrow potential well, which forces the ions into a small region to increase ion density and collisional excitation rate, and has a flat bottom to ensure all of the trapped ions have the same energy. Charge breeding, a technique to increase the charge state of ions, is enabled by further ionization of the trapped ions by the electron beam (Penetrante et al., 1991). Collisions between the beam electrons and trapped ions efficiently drive ionization, excitation, and recombination processes, as electrons inside the trap have well-defined kinetic energy due to acceleration potentials corrected by the space-charge contributions of the electron beam and trapped ions. The charge-state distribution inside an EBIT is determined by the ionization and recombination rates, which themselves depend on the electron beam energy and density, the confinement time, and the background neutral gas pressure in the trap center. The densities achieved in the trap are low enough to be in the coronal limit, meaning

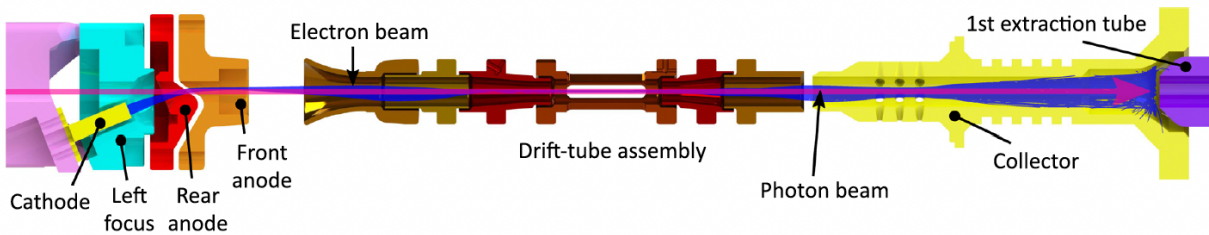
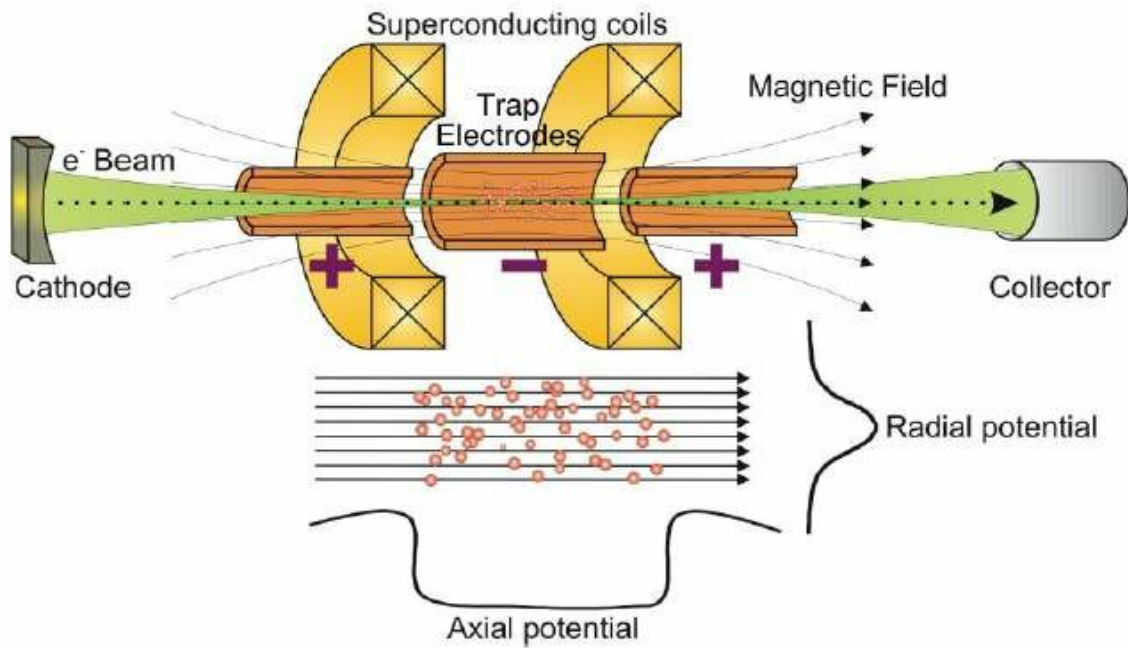


Figure 1.7: **(Top)** EBIT Schematic from Hjalmar Bruhns (Max Planck Institute for Nuclear Physics). Electrostatic potential confines the ions axially and the electron beam space-charge radially. Ions are bred to higher charge states by impact with the electron beam. **(Bottom)** EBIT diagram from Micke et al. (2018). Ions are produced, trapped, and examined at the center of the drift tube assembly.

the collisional rates are much lower than the rates for radiative and autoionization processes. As a result, an ion has time to de-excite to the ground state following ionization, excitation, or recombination processes, emitting radiation for subsequent detection. The unidirectional electron beam produces anisotropic and polarized X-ray emission.

EBITs are also equipped with a vacuum system consisting of several turbomolecular pumps (TMPs) to reach an ultra-high vacuum (UHV) pressure on the order of 1×10^{-9} mbar. UHV conditions are required as low residual gas pressure is essential for both producing and maintaining high ion charge states. To ensure that these conditions are maintained, each subsection of the EBIT (electron gun, trap, collector, injection system) is connected to a two-stage pumping system consisting of a TMP and a pre-vacuum system, which itself consists of an additional TMP and a roughing pump.

The modern EBIT was first developed in the 1980s by [Levine et al. \(1988\)](#) at the Livermore Lawrence National Laboratory (LLNL). EBITs have enabled direct access to the confined ion cloud mono-energetic excitation, as well as photoexcitation and photoionization by monoenergetic photons at synchrotron facilities, making them extremely valuable spectroscopic instruments. The most prominent class are high-performance EBITs, which use superconducting magnets with field strengths from 3 – 8 T. These EBITs are responsible for most of the experiments conducted over the last three decades ([McDonald et al., 1992](#); [Dilling et al., 2006](#); [Xue et al., 2014](#)). These experiments have proven essential for furthering our understanding of astrophysics, as well as atomic theory and metrology, as the extracted electron-impact excitation, ionization, and recombination cross sections are fundamental parameters that have facilitated the analysis of astrophysical phenomena ([Hitomi Collaboration et al., 2017](#)) and complex materials ([Fowler et al., 2021](#)).

An additional class are miniature room-temperature EBITs with permanent magnets, developed in order to achieve compactness and reduce construction and operational costs (Khodja & Briand, 1997; Schmidt et al., 2014; Liang et al., 2019). This class was optimized by Micke et al. (2018) with the novel design of the Heidelberg Compact EBIT (HC-EBIT), which offers a stronger magnetic field up to 0.86 T, higher electron beam currents up to 80 mA, and higher electron beam energies up to 10 keV. A subclass of mini-EBITs have also been developed for use at synchrotron light sources by means of an off-axis electron gun, thereby enabling experiments of trapped highly charged ions that are excited or ionized by the radiation of synchrotron beamlines.

Permanent-magnet EBITs are composed of four main sub-assemblies: 1) a permanent magnet housing structure surrounding a central conical vacuum chamber; 2) a cylindrical drift tube assembly; 3) the electron gun; and 4) the collector. The drift tube assembly and the collector are both mounted inside the central vacuum chamber. The magnetic structure of the permanent-magnet EBIT has a compact rotational symmetry allowing for sufficient space around the trap. Arrays of neodymium-iron-boron permanent disk magnets for each of the two poles generate the magnetic field, with each array containing three parallel stacks of three magnets and mounted between magnetic steel parts connected to iron rods and pole pieces. The produced magnetic field is guided by the steel and iron parts and concentrated in the axial direction toward the trap at the trap center, reaching a maximum magnetic field strength of 0.86 T.

The drift tube assembly consists of a set of six cylindrical electrodes, which accelerate and guide the electron beam towards the collector and trap the produced ions for study. The drift tubes are stacked along four alumina-ceramic rods and mounted between two stainless-steel rings within the vacuum chamber. The water-cooled collector electrode is where the electron

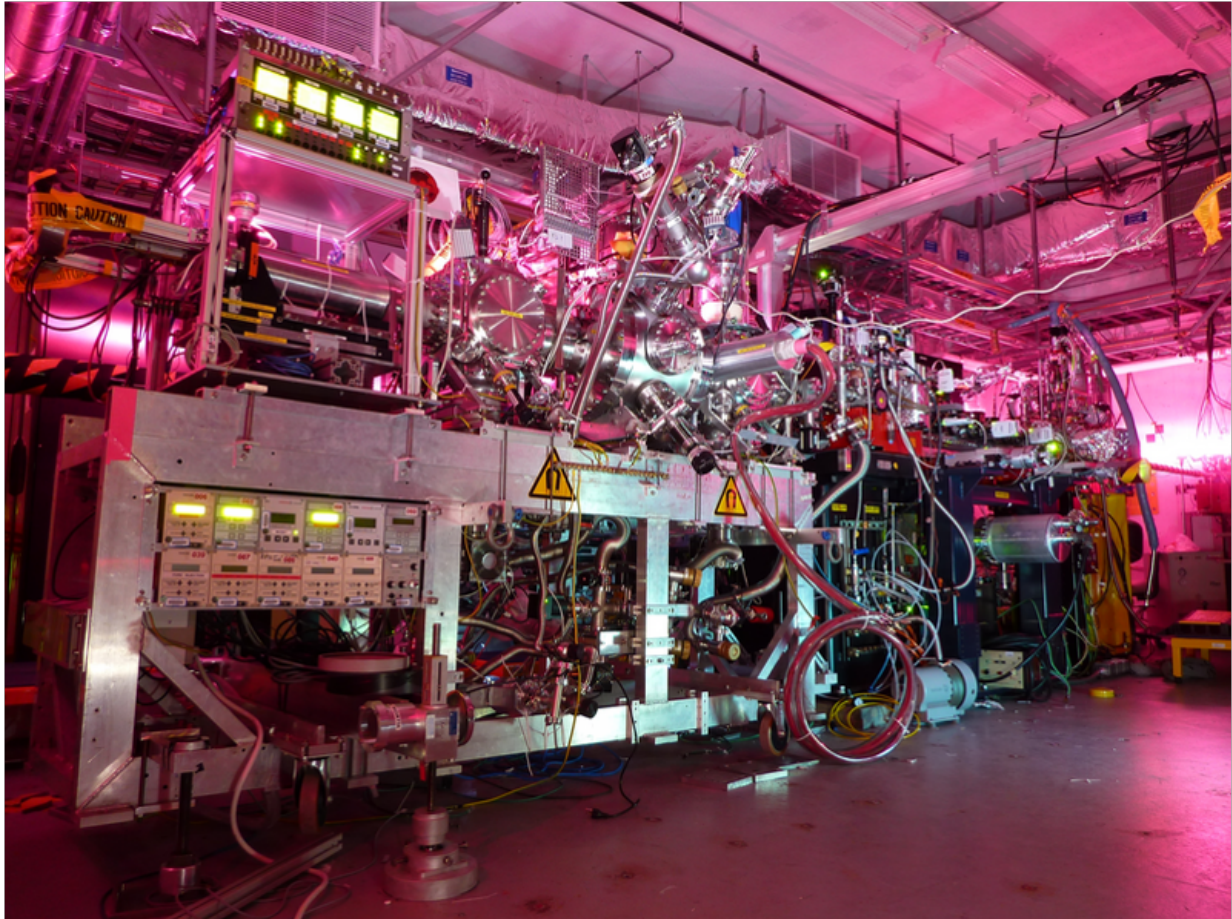


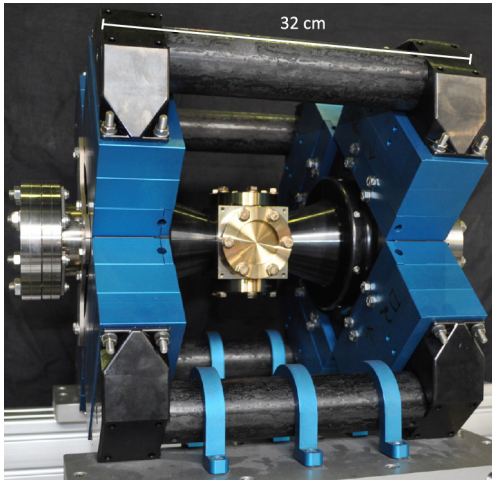
Figure 1.8: FLASH-EBIT at the Linac Coherent Light Source (LCLS) (Picture from José Crespo López-Urrutia).

beam terminates at ground. The magnetic field strength at the collector is much lower than at the trap center, which allows the electron beam to expand and hit the wall. It is composed of two copper parts, the inner collector electrode and the outer shell enclosing a volume for cooling water.

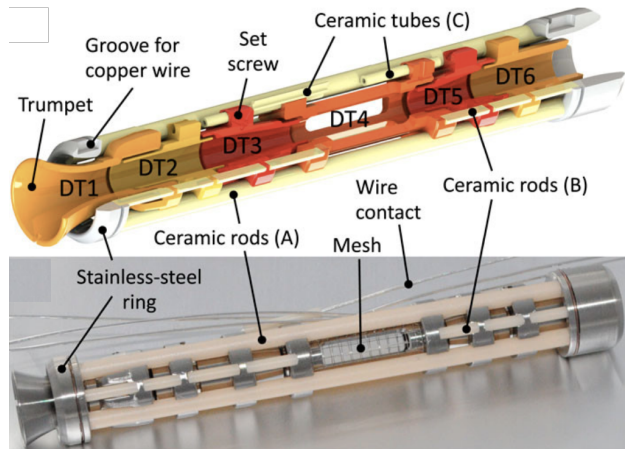
The use of an off-axis electron gun allows an external X-ray photon beam to pass through the permanent-magnet EBIT, which allows the simultaneous use of a second end station and thus enables cross calibration of the energy scale for different experimental techniques. When used at synchrotron beamlines, EBITs have been utilized for high-precision transition energy and oscillator strength measurements ([Leutenegger et al., 2020](#); [Kühn et al., 2022](#)) as well as radiative branching ratios and natural line widths of inner-shell transitions ([Steinbrügge et al., 2022](#)), which are key parameters for studies of photoionized plasmas near X-ray sources powered by accretion onto compact objects. These experiments are essential for fully understanding the formation of accretion-powered sources such as AGN ([Simon et al., 2010](#)) and XRBs ([Beiersdorfer et al., 2017a](#)). Oscillator strength and natural line width measurements are also enabled, which are sensitive tests of atomic structure calculations used in X-ray plasma emission models ([Bernitt et al., 2012](#); [Kühn et al., 2020](#)).

1.5.2 X-ray Detectors

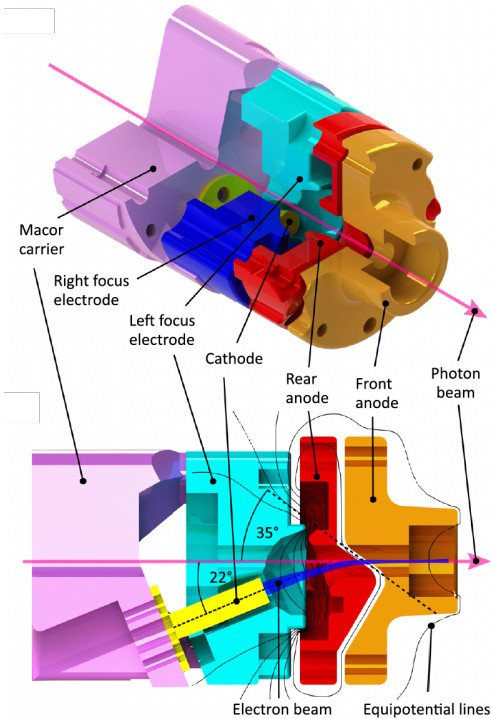
Silicon drift detectors (SDDs) have proven to be reliable for measurements of the X-ray emission from EBIT experiments. SDDs are a type of semiconductor (solid-state) detection device that produces electron-hole pairs in response to irradiation, which can then be collected and read out ([Rachevski et al., 2014](#)). In SDDs, a charge is generated through photon absorption



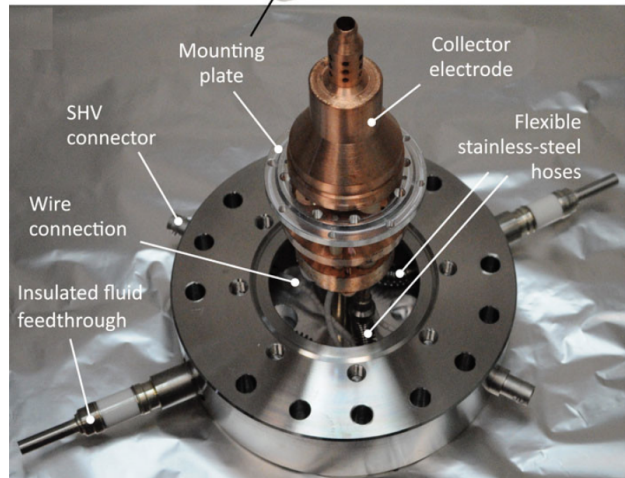
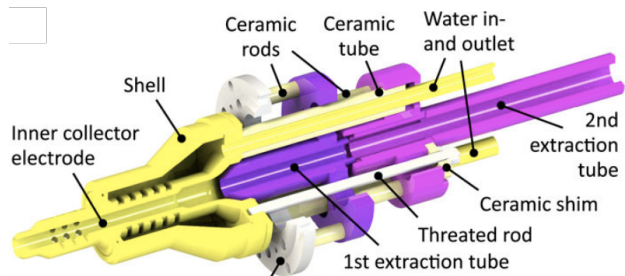
(a) Permanent magnet EBIT housing, highlighting magnets (blue) and magnet yoke (black) surrounding the central conical vacuum chamber containing the EBIT.



(b) The drift tube assembly which provides an electric potential structure that guides the electron beam and traps the produced ions.



(c) The electron gun which points at an angle of 22° to the trap axis to allow an external photon beam to pass through the central bore.



(d) The water-cooled collector where the electron beam terminates at ground.

Figure 1.9: EBIT main sub-assemblies. All images from [Micke et al. \(2018\)](#).

by the silicon material in the middle plane of the detector, and is then drifted towards a readout anode at the detector edge by an electric field sustained through a series of cathodes on both sides. The charge cloud widens due to diffusion while drifting. Upon reaching the readout anode, the charge is measured with an amplifier and is converted to a digital value. SDDs offer a very high count rate capability as a result of their ability to operate at short signal peaking times. The EBIT experiment described in Chapter 3 utilized an SDD for emission detection.

X-ray microcalorimeters achieve significantly higher photon energy resolution measurements than SDDs. Calorimeters such as *XRISM*'s Resolve use doped silicon thermistors cooled down to 50 mK which enable a ~ 5 eV energy resolution for 6 keV X-ray photons (Porter et al., 2018; Ezoe et al., 2020), a significant improvement over an SDD's ~ 125 eV resolution for the same photon energy. As mentioned in Section 1.1, a microcalorimeter consists of an X-ray absorber that absorbs incoming photons through the photoelectric effect, a thermometer that measures the temperature rise of the absorber, and a cryogenically-cooled heat sink that collects the heat and cools the system back down to its equilibrium temperature (Moseley et al., 1984; McCammon, 2005). The system must be cooled to sub-Kelvin temperatures in order to suppress noise.

A transition-edge sensor (TES), which is the planned detection system for *Athena*'s X-ray Integral Field Unit (X-IFU) (Barret et al., 2016), is currently the most mature type of microcalorimeter (Betancourt-Martinez et al., 2014). This calorimeter design works by biasing a superconducting film in its superconducting-to-normal transition. The resistance of the film is highly sensitive to temperature changes caused by photon absorption, which enables its function as a calorimeter to measure single photon energies. Considering these instruments are the detection systems for *XRISM* and *Athena*, targeted laboratory experiments

using microcalorimeters are essential to maximize the utility of spectral observations from these missions.

1.6 Iron Transition Lines

Iron is among the most abundant elements in the visible Universe, with transitions from iron ions dominating the X-ray spectra of many objects. As a result, iron transition lines are of significant importance for astrophysical plasma studies (Decaux et al., 1997). The Fe-K complex (transitions out of the K-shell) contains some of the strongest emission lines in the 6.4 – 7 keV energy range band from collisionally ionized plasmas with temperatures between 2 – 12 keV, in which intermediate-Z elements such as iron are significantly ionized. Transitions onto $n = 1$ states of H-like (Fe XXVI) and He-like (Fe XXV) ions comprise the K-shell lines. When an electron vacancy in the K-shell is filled by an L-shell electron, the transition is referred to as a $K\alpha$ line. Similarly when the K-shell vacancy is filled by an M-shell electron, the transition produces a $K\beta$ line. Fe $K\alpha$ emission spectra are produced by $2p - 1s$ inner-shell radiative transitions for several charge states from Fe XVIII–XXIV. These lines are crowded in a relatively narrow spectral band, and have been observed with high resolution from solar flares (Tanaka, 1986), AGN (Fabian et al., 2000), and the accretion disks of supermassive black holes (Jovanović et al., 2011). The most prominent line, known as the "K" line or "broad iron" line, is composed of the $K\alpha_1$ line at 6.404 keV and $K\alpha_2$ line at 6.391 keV (Kaastra & Mewe, 1993). The production of these lines is theorized to be caused by collisional excitation of neutral Fe I by low energy electrons.

The Fe XXV $K\alpha$ line is a blend of He-like triplet lines at 6.7 keV. Decay from the states $[1s2p] \ ^1P_1$, $[1s2p] \ ^3P_1$, $[1s2p] \ ^3P_2$, and $[1s2s] \ ^3S_1$ to the $[1s^2] \ ^1S_0$ ground state produce the

Fe XXV w resonance line, x intercombination line, y intercombination line, and z forbidden line respectively. These lines, produced by photionization and collisional excitation in hot plasmas, are prominent features of many X-ray emitting astrophysical sources (Koyama et al., 2007). Additionally, the $K\alpha$ line may also include satellite lines produced by DR and innershell excitation (Beiersdorfer et al., 1992, 1993). Because the observed line centroid and line width of the $K\alpha$ line depends on the intensity ratio of the triplet lines, the line is a key diagnostic for plasma temperature and velocity turbulence conditions as later described in Chapter 5.

The Fe-L complex (transitions out of the L-shell) has some of the strongest features in the X-ray spectra of many collisional plasma sources below 2 keV, including massive stars and galaxy clusters (Gu et al., 2019). The complex is populated by radiative transitions onto $n = 2$ states of neon-like (Fe XVII) to lithium-like (Fe XXIV) Fe ions, primarily through multiple channels of collisional excitation, recombination, and ionization mechanisms.

The X-ray spectrum from Fe XVII (or Fe $^{16+}$) in particular has one of the strongest spectral signatures of any highly charged ion. In this system, sixteen electrons are removed and ten remain within the electronic shell, hence the system has a similar electronic configuration as neutral neon. Spectra from hot astrophysical plasmas with temperatures of a few MK are dominated by the L-shell transitions of Fe XVII ions in the 0.7 - 0.9 keV range, particularly the $3d - 2p$ and $3s - 2p$ transitions (Parkinson, 1973; Canizares et al., 2000; Behar et al., 2001a; Xu et al., 2002). Fe XVII is the dominant ion under these conditions due to its closed-shell configuration and high ionization potential (Chen et al., 2003). The Fe XVII X-ray spectrum is dominated by two manifolds in particular: transitions from $3d - 2p$ and $3s - 2p$ levels. Decay from the states $[2p_{1/2}^2 2p_{3/2}^4 3d_{3/2}]_{J=1} \ ^1P_1$ and $[2p_{1/2}^2 2p_{3/2}^3 3d_{5/2}]_{J=1} \ ^3D_1$ to the $[2p^6]_{J=0} \ ^1S_0$ ground state produce the $3d - 2p$ transitions known as the 3C and 3D lines respectively, which are found in the 0.8 - 0.9

keV range. The $3s - 2p$ transitions produce the $3F$, $3G$, and $M2$ lines found in the $0.7 - 0.8$ keV range. The spectroscopic notations for the $3s - 2p$ lines are described in Chapters 2 and 4.

The wavelength separation between these transitions is sufficiently wide enough to be resolved by modern spectrometers while also narrow enough to minimize errors in spectrometer response (Brown et al., 1998; Paerels & Kahn, 2003). As a result, these Fe XVII transitions, along with the less intense Fe L-shell transitions in other charge states such as sodium-like and fluorine-like Fe, are potentially useful diagnostics for physical conditions of hot astrophysical plasmas. These conditions include electron temperature, density, velocity turbulence, and X-ray opacity diagnostics (Behar et al., 2001a; Beiersdorfer et al., 2018; Paerels & Kahn, 2003).

An effective method to infer gas velocity structure in elliptical galaxies, galaxy clusters, and coronal active regions is to use the Fe XVII transition lines to probe the effect of resonant scattering as a diagnostic (Rugge & McKenzie, 1985). The $3C$, $3G$, and $M2$ lines are very sensitive to the effect due to their emissivities and the Fe XVII ionic fraction peaking in the $0.3 - 10$ keV temperature range (Ogorzalek et al., 2017). Additionally, since their transition probabilities are high, they have high cross sections to absorb and immediately re-emit photons of the same energy (resonant scattering). This ultimately leads to line flux suppression along the observer line-of-sight towards the core of elliptical galaxies (Gilfanov et al., 1987). Resonant scattering is reduced by small-scale turbulent gas motions which broaden the line and lower the optical depth. As a result, measuring the level of the effect can be used to constrain the turbulent velocities in the X-ray emitting plasma of galaxies. Using the ratio of these lines as a diagnostic enabled the estimation of turbulent velocity amplitudes of the order of 100 km/s in the cores of the elliptical galaxies NGC 4636 (Xu et al., 2002; Werner et al., 2009), NGC 5044, and NGC 5813 (de Plaa et al., 2012).

The lines have also proven crucial for studies of opacity in coronal hot stars such as Capella (Mewe et al., 2001; Phillips et al., 2001), as well as iron abundances in elliptical galaxies, the interstellar medium, circumgalactic medium, and galactic halos (Nakashima et al., 2018). Iron abundances and abundance ratios such as $[O/Fe]$, which are primarily constrained by Fe XVII emission lines, have been key for probing the physical conditions and origins of these astrophysical regions. The $3s - 2p$ transition lines have also proven to be sensitive to electron density and UV photoexcitation (Mauche et al., 2001). In Chapter 2, I assess the potential use of the Fe XVII $3s - 2p$ transition line ratios as an independent diagnostic of plasma formation radius in O-type stars (Grell et al., 2021). The motivation for this work was to investigate an anomalous Fe XVII $3s - 2p$ line ratio in the X-ray spectrum of the O-type star ζ Puppis, which exhibited a $(3G + M2) / (3F)$ line ratio value of ~ 1.4 in comparison with ~ 2.4 for almost all other collisionally excited astrophysical spectra. I utilized the FAC CRM to model the effect of UV photoexcitation from O stars on the ratio values.

This work was one of numerous studies, which are also further described in Chapter 2, over several decades that have demonstrated significant disparities between the astrophysical observations, laboratory experiments, and theoretical calculations of line intensity ratios of the astrophysically important Fe XVII $3d - 2p$ and $3s - 2p$ transitions (Beiersdorfer et al., 2002; Ness & Schmitt, 2005; Gu, 2008). Disparities of 10 – 20% (Phillips et al., 1999; Beiersdorfer et al., 2002; Beiersdorfer et al., 2004; Brown et al., 2006; Shah et al., 2019) between theoretical models, laboratory experiments, and observational data have led to significant systematic uncertainties in analyses of X-ray astrophysical spectra, thus severely limiting interpretations.

For example, de Plaa et al. (2012) estimated uncertainties as high as 30% for the individual Fe XVII line strengths produced by spectral modeling codes, which led to a factor of two

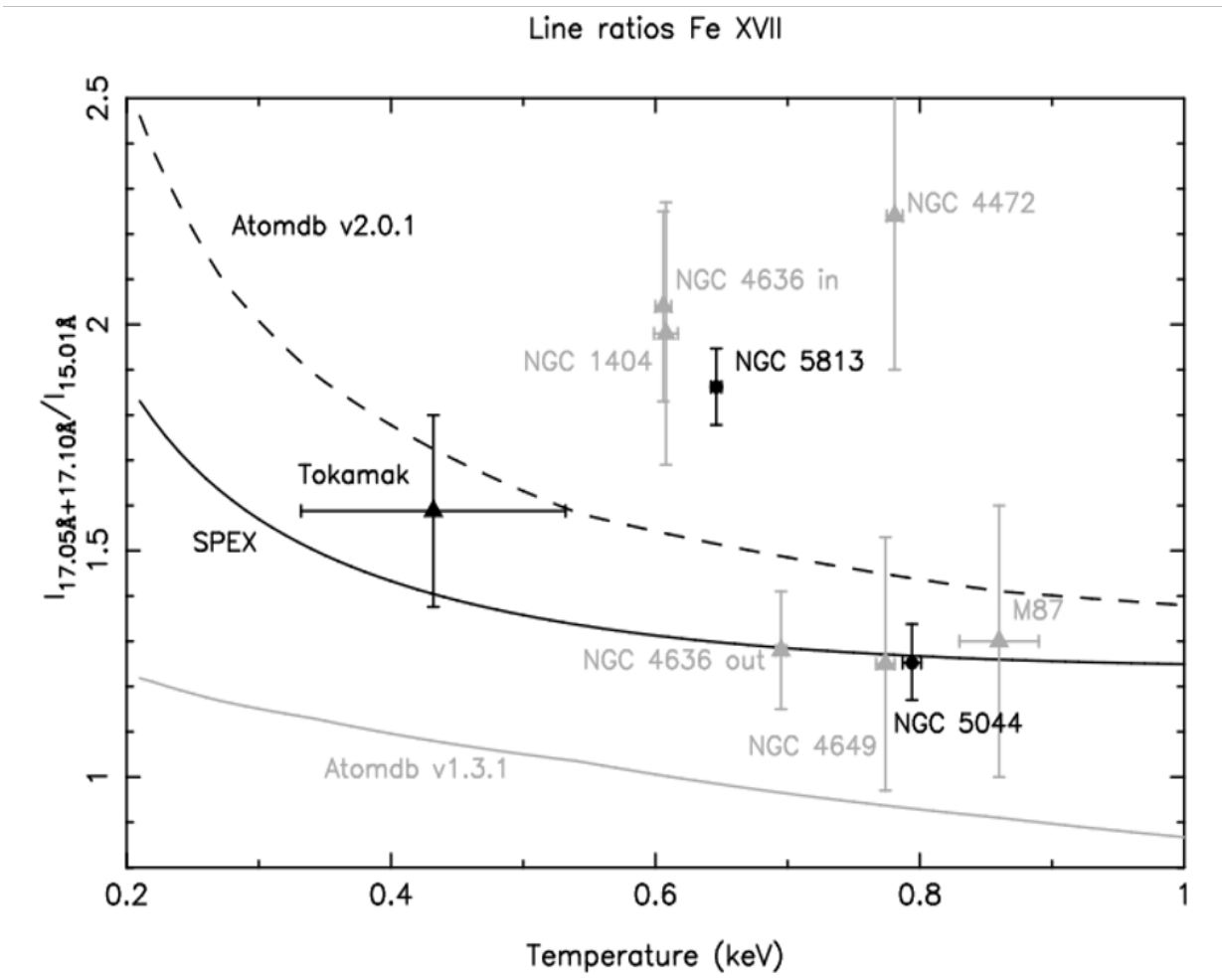


Figure 1.10: Observed, experimental, and theoretical values for the Fe XVII (3G + M2) / 3C ratio as a function of temperature. AtomDB prediction differs by 30% compared to SPEX prediction, thus limiting conclusive interpretations of the astrophysical values derived from the spectra of elliptical galaxies. Figure is from [de Plaa et al. \(2012\)](#).

difference in the derived turbulent velocity when the $(3G + M2) / (3C)$ ratio was increased by just 15%. As shown in Figure 1.10, the significant disparity between the two major plasma codes SPEX (Kaastra et al., 1996b) and APEC (Smith et al., 2001), as well as the laboratory measurement from a tokamak experiment, severely limit astrophysical interpretations of the spectra from elliptical galaxies NGC 5044 and NGC 5813. Ogorzalek et al. (2017) also used the $M2 / 3F$ line ratio to constrain the turbulent velocities in the X-ray emitting plasma of giant elliptical galaxies, but found a 15% difference between APEC and SPEX predicted ratios for the same temperature plasma. These issues emphasize the need for more comprehensive laboratory measurements of these transitions in order to benchmark theoretical predictions with better constraints, especially considering interpretations of these lines are predominantly dependent on broadband fits using atomic structure codes to model spectral features (Liedahl et al., 1995).

Recent experiments have made progress in investigating these discrepancies. Shah et al. (2019) used the FLASH-EBIT (Epp et al., 2010) to determine Fe XVII $3s$ and $3d$ line emission cross sections and use the measurements to benchmark theoretical predictions from FAC. Figure 1.11 shows the theory-experiment cross section comparison for the $3d$ manifold. They improved the electron beam energy resolution (~ 5 eV) by an order of magnitude compared to previous experiments, allowing resolution of strong DR and RE resonance contributions to DE. These measurements were used to calibrate the atomic data implemented in the SPEX (Kaastra et al., 1996b) spectral modeling code. Bernitt et al. (2012) and Kühn et al. (2020) measured the oscillator strengths of Fe XVII transitions using a novel X-ray laser spectroscopy technique and found them to be lower than predicted by most atomic theoretical calculations, but consistent with astrophysical observations and EBIT measurements. Most recently, Kühn et al. (2022) used the PolarX-EBIT (Micke et al., 2018) to find an experimental Fe XVII $3C / 3D$ oscillator-strength

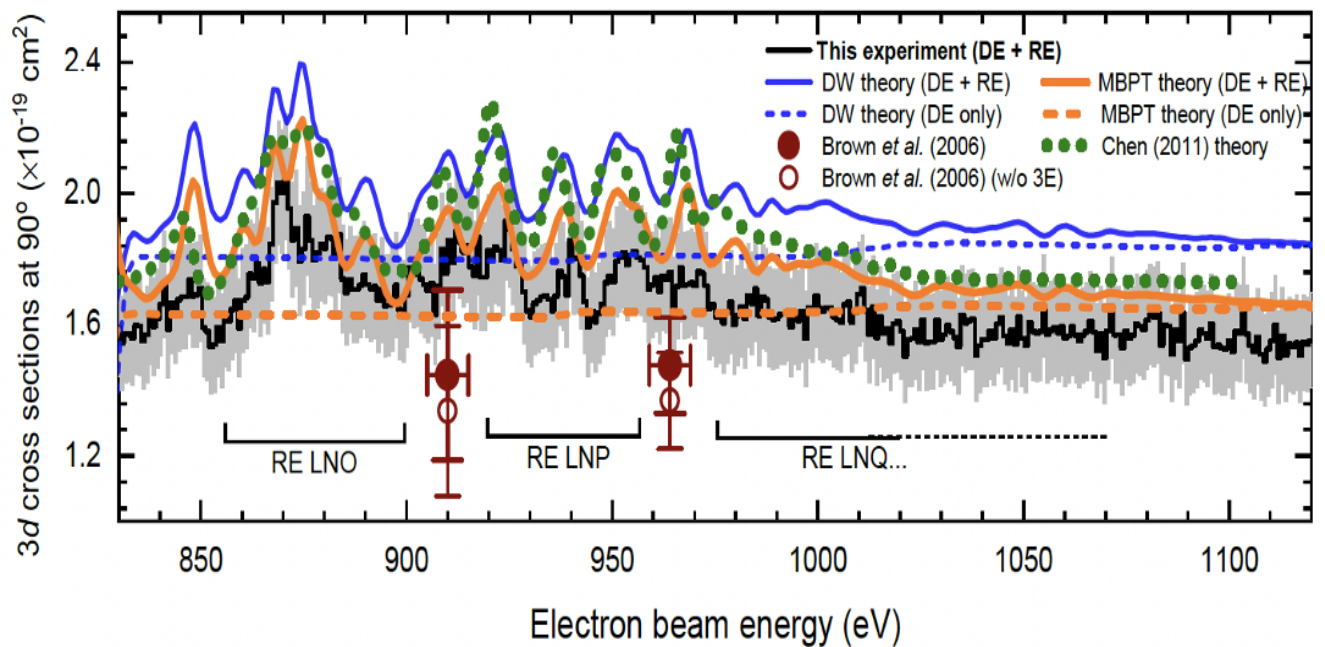


Figure 1.11: Figure from [Shah et al. \(2019\)](#) showing comparison of experimental and theoretical excitation cross sections for the Fe XVII $3d - 2p$ transition manifold as a function of electron beam energy (eV). Theoretical calculations from FAC (using both the distorted-wave (DW) approximation and MBPT), as well as calculations from [Chen \(2011\)](#), overestimate the $3d$ experimental cross sections from FLASH-EBIT (black curve) by $\sim 10 - 20\%$.

ratio finally in excellent agreement with theoretical predictions.

Despite extensive efforts to improve theoretical methods and experiments, significant systematic uncertainties still remain for these lines. Additionally, most of the widely used atomic databases such as NIST, AtomDB, and CHIANTI are not using up-to-date benchmarked models. Given the fact that Fe XVII emission is ubiquitous in the X-ray spectra of nearly all high energy objects, it is imperative to continue improvement efforts in order to construct more reliable spectral and atomic models. This will immediately facilitate several science goals that have been set for XRISM targets, particularly concerning turbulent velocity amplitudes, iron abundances, and optical depth in elliptical galaxies, clusters, and stellar coronae. These astrophysical quantities will soon be limited by the systematic uncertainties of atomic models and not observational capabilities.

1.7 Outline of Dissertation

In this dissertation, I aim to further improve the diagnostic utility of iron transition lines by conducting studies through theoretical, experimental, and observational means. Four main questions are addressed in the following chapters:

1. Can neon-like Fe XVII transition lines be used as a diagnostic of the radial distribution of the X-ray-emitting plasma in massive hot stars?
2. Can laboratory measurements from an electron beam ion trap experiment be used to improve constraints on the theoretical predictions of Fe XVII lines produced by direct electron-impact excitation and dielectronic recombination?

3. Can theoretical and experimental efforts be combined to probe the effect of resonant Auger destruction in the Fe XVII transition lines of massive hot stars?
4. Can well-resolved Fe-K lines from XRISM observations be used to provide accurate temperature and velocity constraints on the Messier 82 galaxy?

In Chapter 2, I use the FAC collisional-radiative model to model the effect of photoexcitation from O-type stars on Fe XVII $3s - 2p$ line ratios in an attempt to explain an anomalous ratio value in the O star ζ Puppis. In Chapter 3, I benchmark theoretical atomic calculations from FAC by comparing model-predicted Fe XVII DR satellite cross sections to experimental cross sections measured using FLASH-EBIT at the Max Planck Institute for Nuclear Physics (MPI-K) in Heidelberg, Germany. In Chapter 4, I investigate the potential significance of resonant Auger destruction of Fe XVII photons caused by lower iron charge states in causing the same ζ Puppis Fe XVII ratio anomaly. In Chapter 5, I provide a summary and conclusions for the dissertation and describe the planned analysis of Fe K-shell emission lines from XRISM observations of the starburst galaxy Messier 82 (M82), which was selected as a top priority Performance Verification (PV) target for the mission.

Chapter 2: Fe XVII $2p$ - $3s$ Line Ratio Diagnostic of Shock Formation Radius in O Stars¹

2.1 Introduction

The first discovery of X-ray emission from a massive hot star was achieved by the Einstein satellite in 1979 after observations of the X-ray binary Cyg X-3 revealed the presence of bright O-type stars in the nearby vicinity (Harnden et al., 1979). The X-ray spectra of hot stars are mainly thermal in nature, as they have been proven to be dominated by discrete lines from metals with ionization stages skewed toward lower temperatures (Guedel & Naze, 2009). The spectra also appear soft (particularly for O stars), as the best fits have favored thermal components with temperatures less than 1 keV (Zhekov & Palla, 2007; Cohen et al., 2014).

OB stars are known to produce powerful winds with mass-loss rates as high as $10^{-5} M_{\odot} \text{yr}^{-1}$ (Morton, 1967; Puls et al., 2006). These winds are driven by radiation pressure from scattering in UV transitions (Castor et al., 1975), where this force is multiplied by displacement of optically thick driving transitions from their shadow in frequency space due to their Doppler shift in the supersonic wind, an effect known as deshadowing.

The currently accepted model for X-ray production in single, nonmagnetic OB stars was

¹Published in *The Astrophysical Journal* Vol. 917 as "Fe XVII $2p$ - $3s$ Line Ratio Diagnostic of Shock Formation Radius in O Stars" by G. J. Grell, M. A. Leutenegger, and C. Shah

introduced by [Feldmeier et al. \(1997\)](#), who used hydrodynamic simulations to show that X-ray emission arises in mutual collisions of dense, shock-compressed shells; this phenomenon is known as the embedded wind shock (EWS) mechanism. These wind shocks were theorized to arise from the instabilities intrinsic to deshadowing in the line-driving mechanism responsible for the stellar wind ([Lucy & Solomon, 1970](#); [Owocki et al., 1988](#)). The scattered radiation field should suppress these instabilities near the wind base, and shocks are expected to form starting a few tenths of the stellar radius above the photosphere ([Owocki & Puls, 1999](#); [Sundqvist & Owocki, 2015](#)).

X-ray emission lines observed with the high-resolution diffraction grating spectrometers on board *XMM-Newton* and *Chandra* have confirmed the source of soft X-ray emission in single, nonmagnetic O stars to be EWS ([Cassinelli et al., 2001](#); [Kahn et al., 2001b](#); [Kramer et al., 2003](#)), given their relatively soft spectra and velocity-broadened emission lines. [Owocki & Cohen \(2001\)](#) calculated theoretical X-ray line profiles expected for hot stars when assuming that X-ray-emitting material follows the bulk motion of the wind, finding that higher continuum photoelectric absorption optical depths produce more asymmetric, blue-shifted lines. These models were applied to derive wind optical depths and thus make mass-loss rate estimates for a sample of stars observed with *Chandra* and *XMM-Newton* ([Cohen et al., 2010, 2014](#)).

The forbidden-to-intercombination line ratio $\mathcal{R} \equiv f/i$ of helium-like ions is a diagnostic of electron density and UV field strength². UV photons and/or collisions depopulate the metastable upper level $1s2s^3S_1$ of the forbidden line ($1s2s^3S_1 \rightarrow 1s^2^1S_0$) and weaken it while enhancing the strength of the intercombination lines ($1s2p^3P_{1,2} \rightarrow 1s^2^1S_0$) ([Gabriel & Jordan, 1969](#); [Blumenthal](#)

²In this chapter we adopt the notational convention that ratios are denoted with calligraphic \mathcal{R} , while stellar radii are denoted with italic R .

et al., 1972). The scaling of the ratio with UV flux and electron density is given by

$$\mathcal{R} = \mathcal{R}_0 \frac{1}{1 + \phi/\phi_c + n_e/n_c}, \quad (2.1)$$

where \mathcal{R}_0 is the ratio value in the limit of no UV photoexcitation and low electron density, ϕ is the photoexcitation rate from 2^3S to 2^3P , n_e is the electron density, ϕ_c is the critical photoexcitation rate at which $\mathcal{R} = \mathcal{R}_0/2$, and n_c is the critical density. The mean density in the wind of a massive star is given by $n_e = 6.4 \times 10^9 \text{ cm}^{-3} \dot{M}_{-6} r_{20}^{-2} v_{2000}^{-1}$, where \dot{M}_{-6} is the mass-loss rate in units of $10^{-6} M_\odot \text{ yr}^{-1}$, r_{20} is the radius in units of $20 R_\odot$, and v_{2000} is the velocity in units of 2000 km s^{-1} . Such densities are not high enough to affect \mathcal{R} for most helium-like ions in most of the wind, although the density may be important for N VI and C V in the inner wind. Because the mean UV field strength of massive stars is quite high, \mathcal{R} can thus be used as a diagnostic for UV field strength and therefore shock location (Kahn et al., 2001b).

Leutenegger et al. (2006) incorporated the effect of the radial dependence of UV flux on $\mathcal{R} \equiv f/i$ in the context of line profiles based on Owocki & Cohen (2001), and used this to model the helium-like triplet ion complex to constrain the radial distribution of X-ray-emitting plasma in four OB stars. This was parameterized by a shock onset radius R_0 , with X-ray-emitting plasma having a fixed filling factor above this radius. They found that the minimum onset radius of emission is typically $1.25 < R_0/R_* < 1.67$, where R_* is the stellar radius. Furthermore, they showed that the forbidden line is formed at large radii, while the intercombination line is enhanced where the UV flux is higher (close to the star), with the result that the forbidden line is comparatively broad while the intercombination line is somewhat more centrally peaked.

Mauche et al. (2001) developed a similar diagnostic using the metastable $3s$ levels of the

important neon-like Fe XVII ion. They applied their model to the cataclysmic variable (CV) EX Hydra, which is thought to have a high-density polar accretion flow; however, this model has not yet been applied as an observational diagnostic of UV field strength in astrophysics. OB stars are a natural candidate for such an application.

[Leutenegger et al. \(2012\)](#) noted an anomalous ratio in the Fe XVII $2p - 3s$ lines of the O4 supergiant ζ Puppis (see also [Hervé et al., 2013](#)). While the ratio $(3G + M2) / 3F$ is typically found to be approximately 2.4 for all O-type stars, as well as a range of other astrophysical sources, for ζ Pup it was found to be only about 1.4. [Rauw et al. \(2015\)](#) found a similar but lesser effect in the O6 supergiant λ Cephei. Based on [Mauche et al. \(2001\)](#), we conjecture that the strong UV fields of ζ Pup and λ Cep could be responsible for the observed line ratios. However, because the $M2+3G$ blend is typically unresolved in hot star spectra as shown in Figure 2.1 for ζ Pup and ζ Ori, we cannot easily use the $M2/3G$ ratio as in [Mauche et al. \(2001\)](#), and we instead aim to develop the $3F / (3F + 3G + M2)$ fraction as an independent diagnostic of plasma formation radius.

In this chapter, we use the Flexible Atomic Code (FAC) to calculate atomic data and a collisional-radiative model for Fe XVII, accounting for the effect of UV photoexcitation from OB stars, and we incorporate the results of these calculations into existing line profile models for O-star X-ray spectra. § 2.2 of this paper describes the metastable $3s$ levels of Fe XVII and reviews the theoretical literature on this subject. § 2.3 describes the atomic model. § 2.4 describes the line profile model `newind`, which incorporates the radial dependence of the $2p - 3s$ line ratios of neon-like ions. § 2.5 describes observations and data reduction for archival observations of coronal and hot stars taken by the *Chandra* HETGS and *XMM-Newton* RGS, and shows the model fitting results and calculations. In § 2.6 we discuss our results and future work.

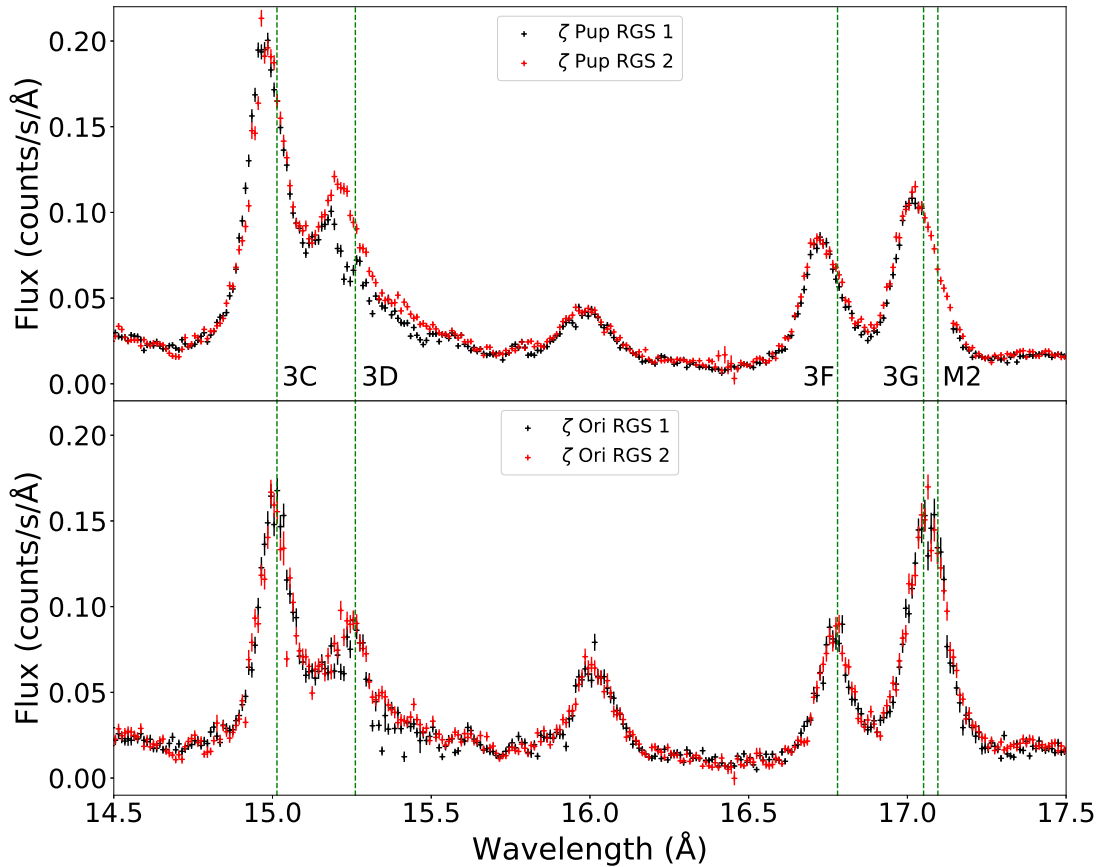


Figure 2.1: *XMM-Newton* RGS spectra of ζ Pup (top) and ζ Ori (bottom). These spectra were obtained from the *XMM-Newton* Science Archive and reduced using the SAS (Science Analysis System) version 18.0. The black plus (+) signs represent the spectra from RGS1, and the red plus signs represent the spectra from RGS2. The green dashed lines represent the wavelengths of (left to right) the 3C, 3D, 3F, 3G, and M2 transitions. The M2+3G complex (17.06 - 17.14 Å) is unresolved in both spectra due to Doppler broadening in the stars' supersonic winds.

2.2 Fe XVII Diagnostics of UV Field Intensity and Density

X-ray spectra from hot plasmas with temperatures of a few MK are dominated by the L-shell $3d - 2p$ and $3s - 2p$ transitions of Fe XVII ions in the 15 – 17 Å range (Parkinson, 1973; Canizares et al., 2000; Behar et al., 2001a; Xu et al., 2002; Paerels & Kahn, 2003). The $3s - 2p$ transitions known as the $3F$, $3G$, and $M2$ lines are produced by decay from $[2p_{1/2}2p_{3/2}^43s_{1/2}]_{J=1} \ ^3P_1^\circ$, $[2p_{1/2}^22p_{3/2}^33s_{1/2}]_{J=1} \ ^1P_1^\circ$, and $[2p_{1/2}^22p_{3/2}^33s_{1/2}]_{J=2} \ ^3P_2^\circ$ to the $[2p^6]_{J=0} \ ^1S_0$ ground state, respectively, as depicted in Figure 2.2. The $3F$ line is observed at 16.777 Å, the $3G$ line at 17.051 Å, and the $M2$ line at 17.096 Å (Brown et al., 1998; May et al., 2005).

Mauche et al. (2001) focused primarily on the strength of the $M2$ line as a density diagnostic, since its weakening is the most striking change in model spectra under the high-density conditions typical in the accretion flow of an intermediate polar cataclysmic variable CV. For most O stars, broadening of the emission lines makes it challenging to independently measure the strength of the $M2$ line, as it blends with $3G$, although, because the broadening is typically only comparable to the splitting of $3G$ and $M2$, it is still possible. A cleaner diagnostic is possible using the $(3G + M2) / 3F$ ratio, although the dynamic range of this ratio across density and UV field strength is smaller than for the $M2$ line alone. For this reason we need to thoroughly optimize our calculations in two important ways. First, we need to use UV field strength models appropriate to O stars, rather than blackbody models. Second, we need to carefully consider the effects of systematic uncertainties in the atomic calculations themselves.

Numerous studies have demonstrated disparities between the astrophysical observations, laboratory experiments, and theoretical calculations of line intensity ratios of the $3s - 2p$ transitions at the $\sim 10 - 20\%$ level (Phillips et al., 1999; Beiersdorfer et al., 2002; Beiersdorfer

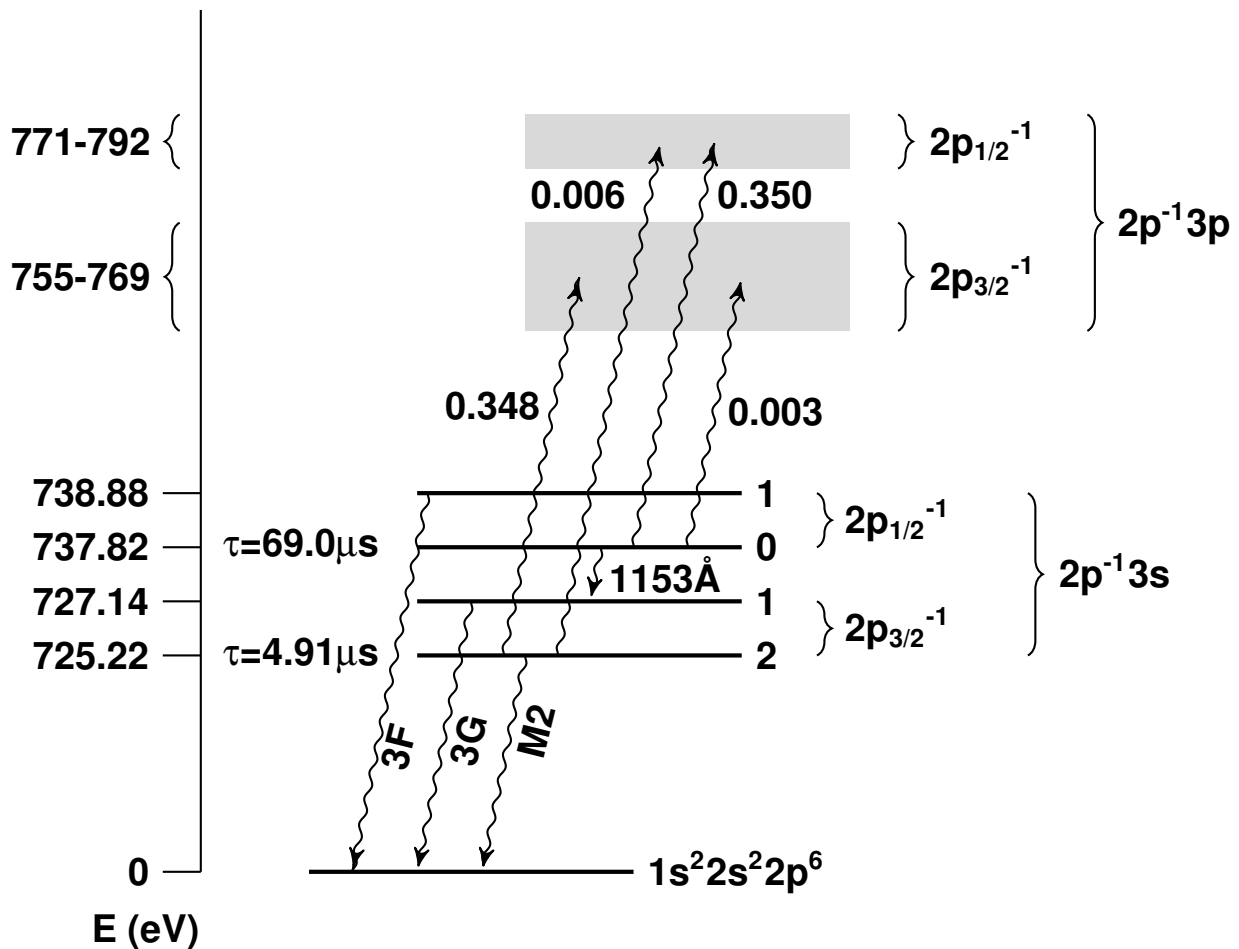


Figure 2.2: Diagram showing important radiative processes for depopulating metastable $3s$ excited states of Fe XVII. Individual energy levels are shown as horizontal lines, while for simplicity groups of $3p$ levels are shown as light-gray boxes. Wavy lines show radiative transitions. Radiative lifetimes of the two metastable states are shown (Crespo López-Urrutia & Beiersdorfer, 2010; Beiersdorfer et al., 2016). Oscillator strengths are printed next to the corresponding transitions; these strengths represent sums over relevant levels.

Table 2.1: Fe XVII ground state and $2p^{-1}3s$ and $2p^{-1}3p$ singly excited levels and their respective configurations and energies (as calculated in this work using FAC and measured from [Brown et al. \(1998\)](#) and [Beiersdorfer et al. \(2016\)](#)). The $1s$ and $2s$ shells are closed in all configurations listed. LS coupling terms were assigned using the GRASP2K atomic structure package ([Jönsson et al., 2013](#)). Mixing of LS coupling terms is especially strong between levels 2 and 4 ($J = 1$, odd), and levels 6, 9, and 13 ($J = 2$, even).

Level	Configuration		Energy (eV)	
			FAC	Experiment
0	$[2p^6]_{J=0}$	1S_0	0.00	0.00
1	$[2p_{1/2}^2 2p_{3/2}^3 3s_{1/2}]_{J=2}$	$^3P_2^o$	724.15	725.22
2	$[2p_{1/2}^2 2p_{3/2}^3 3s_{1/2}]_{J=1}$	$^1P_1^o$	726.19	727.14
3	$[2p_{1/2} 2p_{3/2}^4 3s_{1/2}]_{J=0}$	$^3P_0^o$	736.78	737.82
4	$[2p_{1/2} 2p_{3/2}^4 3s_{1/2}]_{J=1}$	$^3P_1^o$	738.09	738.88
5	$[2p_{1/2}^2 2p_{3/2}^3 3p_{1/2}]_{J=1}$	3S_1	754.47	
6	$[2p_{1/2}^2 2p_{3/2}^3 3p_{1/2}]_{J=2}$	3D_2	758.09	
7	$[2p_{1/2}^2 2p_{3/2}^3 3p_{3/2}]_{J=3}$	3D_3	759.66	
8	$[2p_{1/2}^2 2p_{3/2}^3 3p_{3/2}]_{J=1}$	1P_1	760.86	
9	$[2p_{1/2}^2 2p_{3/2}^3 3p_{3/2}]_{J=2}$	3P_2	762.66	
10	$[2p_{1/2}^2 2p_{3/2}^3 3p_{3/2}]_{J=0}$	3P_0	768.30	
11	$[2p_{1/2} 2p_{3/2}^4 3p_{1/2}]_{J=1}$	3D_1	770.17	
12	$[2p_{1/2} 2p_{3/2}^4 3p_{3/2}]_{J=1}$	3P_1	773.39	
13	$[2p_{1/2} 2p_{3/2}^4 3p_{3/2}]_{J=2}$	1D_2	773.79	
14	$[2p_{1/2} 2p_{3/2}^4 3p_{1/2}]_{J=0}$	1S_0	790.35	

et al., 2004). Moreover, the theoretical predictions of the $M2/3G$ line ratio in the low-density limit have been shown to yield significantly smaller values than both laboratory measurements and astrophysical observations of low-density plasmas (Ness & Schmitt, 2005; Gu, 2008). Such discrepancies have sparked strong interest in the scientific community and given rise to a number of experimental and theoretical works attempting to explain the possible reason for the observed discrepancy.

Initially, Loulergue & Nussbaumer (1975) and Smith et al. (1985) pointed out that the $3s$ line strengths can be affected by the resonant excitation (RE) in Fe XVII. Saba et al. (1999) showed that dielectronic recombination (DR) in Fe XVIII can also alter the $3s$ level populations. Later, Doron & Behar (2002) utilized the Hebrew University Lawrence Livermore Atomic Code, a relativistic configuration interaction (RCI) code, to construct a three-ion model that included the effects of RE of Fe XVII, DR of Fe XVIII, and collisional inner-shell ionization (CI) of Fe XVI as line formation processes, leading to slightly better model-data agreement. Gu (2003) expanded this theoretical study to include all relevant L-shell ions (Fe XVII–XX) using the relativistic distorted-wave method implemented in FAC and showed that DR and RE are highly important for Fe XVII–XX in modeling of collisionally ionized plasmas. Both works also showed that $2p$ inner-shell ionization affects the Fe XVII $3s - 2p$ transition by only 1-3 %.

Furthermore, the collision strengths of $3s$ transitions were also investigated by Chen & Pradhan (2002) and Chen et al. (2003) using the Breit-Pauli R -matrix method. They included all possible resonance contributions that can arise from 89 atomic levels associated with the $n = 3$ and 4 complexes in their close-coupling expansion. Loch et al. (2006) expanded their R -matrix calculations to 139 levels, including $2p^55l$ configurations. The generated atomic data were used in a collisional-radiative model to predict the $3s/3d$ line ratio. However,

EBIT measurements (Beiersdorfer et al., 2002) still showed $\sim 20\%$ discrepancy with the R -matrix calculations. In order to better diagnose the theoretical origins of disagreement with experiment, rather than measuring line ratios as in Beiersdorfer et al. (2002); Beiersdorfer et al. (2004), Brown et al. (2006) measured line emission cross sections for Fe XVII relative to the well-known radiative recombination cross sections and inferred that discrepancies between experiments, observations, and theories exist in the calculation of *direct* excitation cross sections. A converged Dirac R -matrix and relativistic distorted-wave calculations, reported by Chen (2007, 2008), with only $\sim 5\%$ error in calculated cross sections, showed $\sim 20\%$ discrepancy with measurements (Brown et al., 2006).

Gu (2008) later reviewed the accuracy of previous Fe XVII theories by comparing them to *Chandra* spectra of stellar coronae, finding that the main problem of the previous studies was likely the inability to fully include electron correlation effects, which are important for atomic structure calculations. In this work, second-order many-body perturbation theory (MBPT) was used to calculate highly accurate energy levels and transition matrix elements of Fe XVII lines. The cross sections were calculated essentially using the distorted-wave method, though they have been corrected using the accurate multipole transition matrix elements that are calculated using the MBPT method. This improved the cross sections of Fe XVII lines and reduced the disagreement with experiment from $\sim 20\%$ to $\sim 15\%$.

Recent studies have made progress in investigating these discrepancies. Gu et al. (2019) produced model spectra of ions from Fe XVII to Fe XXIV for optically thin, collisionally ionized plasma. They expanded the work of Gu (2003) by including all relevant direct and indirect line formation processes. They used an updated version of FAC, which will be discussed in further detail in § 2.3.1. Their work yielded a 5% lower electron-impact RE rate for the $M2$ line and 30%

lower resonant rate for the 3G line.

[Shah et al. \(2019\)](#) used the Heidelberg FLASH-EBIT to produce an ion population mainly consisting of Fe XVII ions in order to determine the 3s and 3d line emission cross sections. They improved the electron beam energy resolution (~ 5 eV) by an order of magnitude compared to previous experiments, allowing resolution of strong DR and RE resonance contributions to DE, and increased the counting statistics by three orders of magnitude compared to previous experiments ([Laming et al., 2000](#); [Beiersdorfer et al., 2002](#); [Brown et al., 2006](#); [Brown, 2008](#); [Gillaspy et al., 2011](#)). Their cross section and line ratio measurements were compared to different combinations of theoretical atomic models. They found that the combination of distorted-wave and MBPT calculations, previously shown by [Gu \(2008\)](#), led to good agreement with the total 3s cross sections. The model also yielded a 9% discrepancy for the 3d cross section and 11% for 3s/3d, which are both consistent with previous laboratory measurements ([Beiersdorfer et al., 2002](#); [Brown et al., 2006](#)). Moreover, these laboratory data were also used to calibrate the atomic data implemented in the SPEX ([Kaastra et al., 1996b](#)) spectral modeling code. Subsequently, these data were fed into a global model of the *Chandra* grating spectrum of Capella, which in turn improved the overall fit compared to the fit using the default data available in SPEX version 3.04 (see details in [Gu et al. \(2019, 2020\)](#)).

A novel X-ray laser spectroscopy technique was also employed to directly scrutinize the underlying atomic structure of Fe XVII. [Bernitt et al. \(2012\)](#) and [Kühn et al. \(2020\)](#) measured the quantum mechanical oscillator strengths of Fe XVII transitions and found them to be lower than predicted by most atomic theoretical calculations, but consistent with astrophysical observations and EBIT cross-section measurements. The theoretical calculations agreeing the best with the experiments were perturbation theory methods, as well as configuration interaction calculations

using a very large number of states to achieve better convergence.

Despite these extensive efforts to improve theoretical methods and experiments over the past two decades, significant discrepancies still remain for Fe XVII X-ray lines. Thus, as discussed in § 2.3, our theoretical predictions for the $(3G + M2) / 3F$ ratio must therefore be interpreted in the context of aforementioned discrepancies.

2.3 Atomic Model

2.3.1 FAC

Our understanding of stellar astrophysics has made strides with the development of software packages capable of transforming how stellar theory and modeling interact with observations. One such software package is FAC, which calculates atomic structure, as well as a wide range of atomic radiative and collisional processes (Gu, 2008). The atomic code has proven to be robust, as excellent agreement has been found between FAC calculations and both astrophysical data and laboratory measurements (Bitter et al., 2003; Gu, 2003; Zhong et al., 2004; Fournier & Hansen, 2005; Gu et al., 2019).

FAC computes the atomic structure of the initial, intermediate, and final states of a particular charge state, along with its related transitions. The output data include energy levels, radiative and autoionization transition rates, collisional excitation and ionization cross sections, photoionization rates, and autoionization rates, thereby enabling the integration of various atomic processes within a single framework. The code implements a fully relativistic method based on the Dirac equation and distorted-wave approximation for continuum processes, which enable the ability to reliably model highly charged ions.

FAC is also equipped with a collisional-radiative model (CRM) that constructs synthetic spectra for plasmas under different physical conditions using atomic data. It calculates level populations for a given temperature and density assuming collisional-radiative equilibrium. These level populations are then multiplied by the radiative transition rates to derive line intensities.

We used FAC to calculate the line strengths of the Fe XVII transitions at different UV field intensities in order to study changes in line ratio and model the effect of UV photoexcitation from O stars. To do this, we first used FAC to calculate the relevant atomic data for Fe XVII, as well as for the neighboring charge states Fe XVIII and Fe XVI, which contribute to the Fe XVII line formation process through recombination and ionization. We included cascades up to $n = 25$, and resonance excitation with spectators up to $n = 10$. We then ran the CRM for a range of electron temperatures (see, e.g., Figure 2.3) and a range of UV field configurations. For the model-data comparisons in § 2.5, we assumed an electron temperature of 500 eV for all calculations. We assumed a density of 10^4 cm^{-3} for all calculations, i.e. in the limit of the low collisional excitation rate for metastable states.

FAC assumes a uniform UV field with mean local intensity J_ν . For the case of an O star, it is typically assumed that the specific intensity I_ν is constant across the stellar disk (i.e., neglecting limb darkening, and neglecting the scattered radiation field in the wind), so that the mean intensity is given by

$$J_\nu(r) = I_\nu(R_*)W(r), \quad (2.2)$$

where $W(r)$ is the geometrical dilution factor, i.e., the fractional solid angle subtended by the

stellar disk from the point of view of a test particle at radius r :

$$W(r) = \frac{1}{2} \left(1 - \left[1 - \left(\frac{R_\star}{r} \right)^2 \right]^{1/2} \right) \quad (2.3)$$

The maximum astrophysical dilution factor of $W(r) = 0.5$ represents the solid angle just above the photosphere; $W = 1$ would occur only in the interior of an ideal blackbody enclosure.

This is then used to calculate the photoexcitation rates:

$$\phi_{lu} = 4\pi \frac{\pi e^2}{m_e c} f_{lu} \frac{J_\nu}{h\nu}, \quad (2.4)$$

where e is the electron charge, m_e is the electron mass, c is the speed of light, f_{lu} is the oscillator strength for transitions from lower level l to upper level u , h is the Planck constant, and ν is the frequency of the transition.

2.3.2 Analytical Model

In order to gain insight into the numerical results obtained with the FAC CRM and also to allow for adjustments to these results based on experimental and observational constraints, we sought to derive an analytical relation for the Fe XVII line ratios as a function of UV field intensity. To do this, we solved the coupled rate equations for the $n = 3$ singly excited states; a detailed discussion of this is given in Appendix A.2. We obtained the following equations for the case where UV photoexcitation is important but the electron density is sufficiently low:

$$\mathcal{R}_1 = \frac{\mathcal{R}_1^\circ(1 + P_3) + \mathcal{R}_3^\circ P_{3,1}}{(1 + P_1)(1 + P_3) - P_{3,1}P_{1,3}} \quad (2.5)$$

$$\mathcal{R}_2 = \mathcal{R}_2^\circ + \mathcal{R}_1 P_{1,2} + \mathcal{R}_3(1 + P_{3,2}); \quad (2.6)$$

$$\mathcal{R}_3 = \frac{\mathcal{R}_3^\circ(1 + P_1) + \mathcal{R}_1^\circ P_{1,3}}{(1 + P_1)(1 + P_3) - P_{3,1}P_{1,3}}; \quad (2.7)$$

$$\mathcal{R}_4 = \mathcal{R}_4^\circ + \mathcal{R}_1 P_{1,4} + \mathcal{R}_3 P_{3,4}. \quad (2.8)$$

Here the subscripts i refer to the $3s$ excited states in ascending energy order from 1 to 4. \mathcal{R}_i are the ratios of the strengths of decays from level i to ground relative to the sum of all three lines for levels 1, 2, and 4, while \mathcal{R}_3 gives the strength of the UV transition from level 3 to level 2 relative to the sum of the three X-ray lines; in other words, \mathcal{R}_1 , \mathcal{R}_2 , and \mathcal{R}_4 give the fractional strengths of $3F$, $3G$, and $M2$, respectively, within the $2p - 3s$ complex. \mathcal{R}_i° gives the line ratios in the absence of photoexcitation. $P_{i,j}$ gives the effective normalized photoexcitation rate from $3s$ level i to $3s$ level j summed over all intermediate $3p$ states, and P_i gives the effective normalized photoexcitation rate from $3s$ level i to all other levels combined. $P_{i,j}$ and P_i are defined in § A.2.

Table 2.1 shows the relevant Fe XVII levels with their corresponding configurations and energies as calculated by us using FAC. Level index 0 is the ground state, 1-4 are the four $3s$ excited states, and 5-14 are the 10 $3p$ excited states.

Table 2.2 shows the most important $2p-3s$ transitions and their respective oscillator strengths, f_{lu} , and the branching ratios to the lower levels. These values were used to calculate the effective photoexcitation rates for the relevant levels. The final column is the product of the oscillator strength and branching ratio, showing the relative importance of each transition in changing the Fe XVII level populations.

Figure 2.3 shows the trends of the fractions and neon-like charge balance in the absence of UV photoexcitation as a function of electron temperature (eV). The fractions vary only weakly

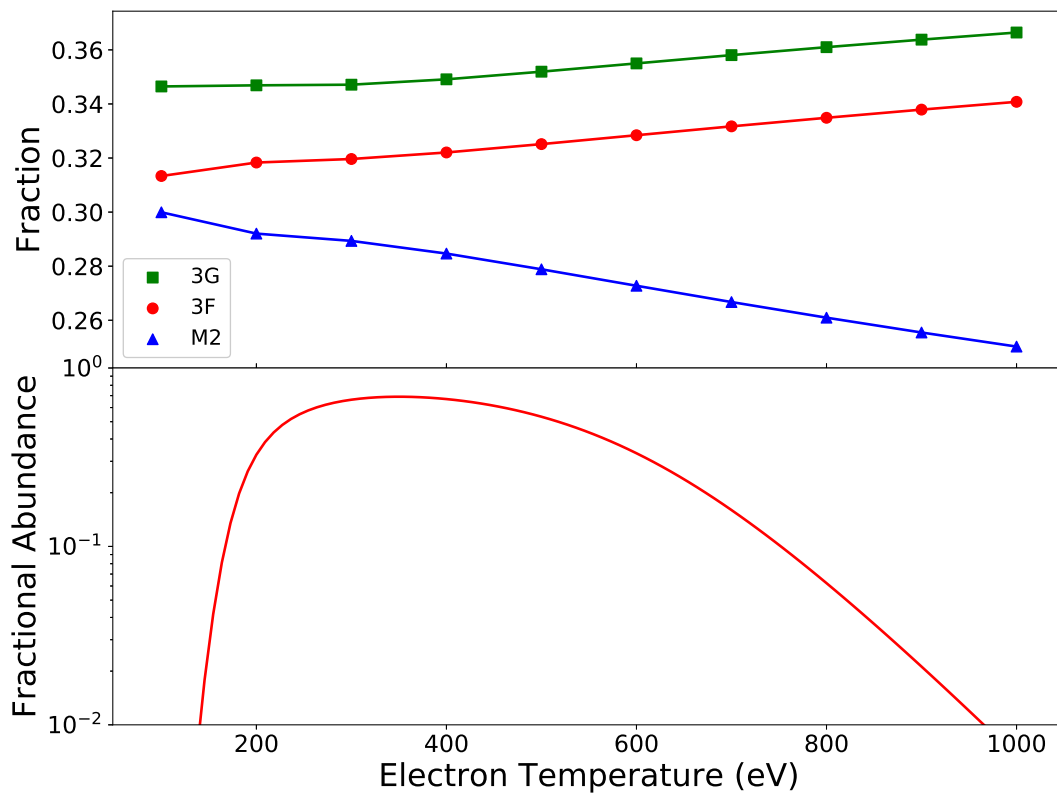


Figure 2.3: Top: fractional line strengths as a function of electron temperature in the low-density limit ($n_e = 10^4 \text{ cm}^{-3}$) and in the absence of UV photoexcitation for the $3F$ (red), $3G$ (green), and $M2$ (blue) transitions. The fractions vary only weakly with temperature. Bottom: neon-like ion fraction as a function of electron temperature.

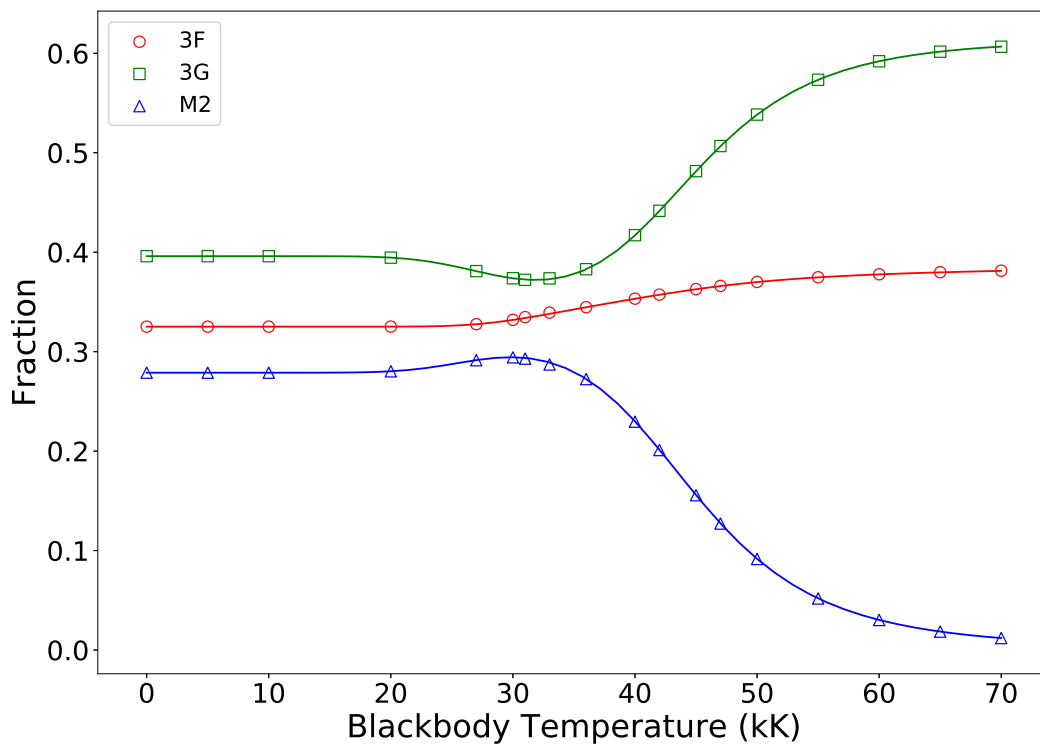


Figure 2.4: Comparison of predicted Fe XVII 3G (green), 3F (red), and M2 (blue) fractions as a function of blackbody temperature for $W = 0.5$. The circles represent the FAC-CRM-predicted ratio values, and the lines represent the corresponding analytic model ratio values.

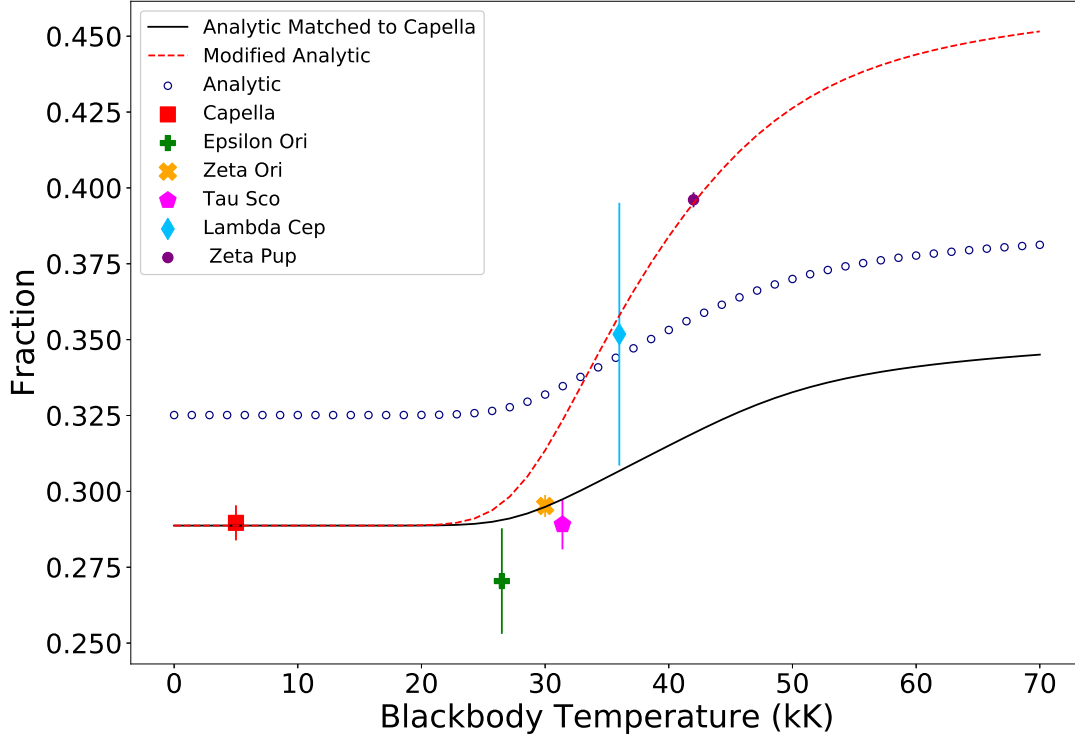


Figure 2.5: Comparison of observed and calculated Fe XVII $3F$ fractions as a function of photospheric blackbody temperature, evaluated at dilution $W = 0.5$, and with electron density $n_e = 10^4 \text{ cm}^{-3}$ and electron temperature $kT_e = 500 \text{ eV}$. The analytical model fraction (red circles) did not match the observed fractions (points with error bars left to right) of Capella ($T_{\text{eff}} = 5 \text{ kK}$), ϵ Ori ($T_{\text{eff}} = 27 \text{ kK}$), ζ Ori ($T_{\text{eff}} = 30 \text{ kK}$), τ Sco ($T_{\text{eff}} = 31.4 \text{ kK}$), λ Cep ($T_{\text{eff}} = 36 \text{ kK}$), and ζ Pup ($T_{\text{eff}} = 42.5 \text{ kK}$). The analytical model was adjusted so that the model ratio at low temperature matched that of Capella by changing the parameter \mathcal{R}_4^0 (black solid line); however, the dynamic range of the ratio was not sufficient to explain the observed ratio of ζ Pup. We further adjusted the model to match the observed ratio of ζ Pup by increasing \mathcal{R}_3^0 by a factor of 4.125 at the expense of \mathcal{R}_2^0 (red dashed line). This degree of increase required in \mathcal{R}_3^0 is unrealistic.

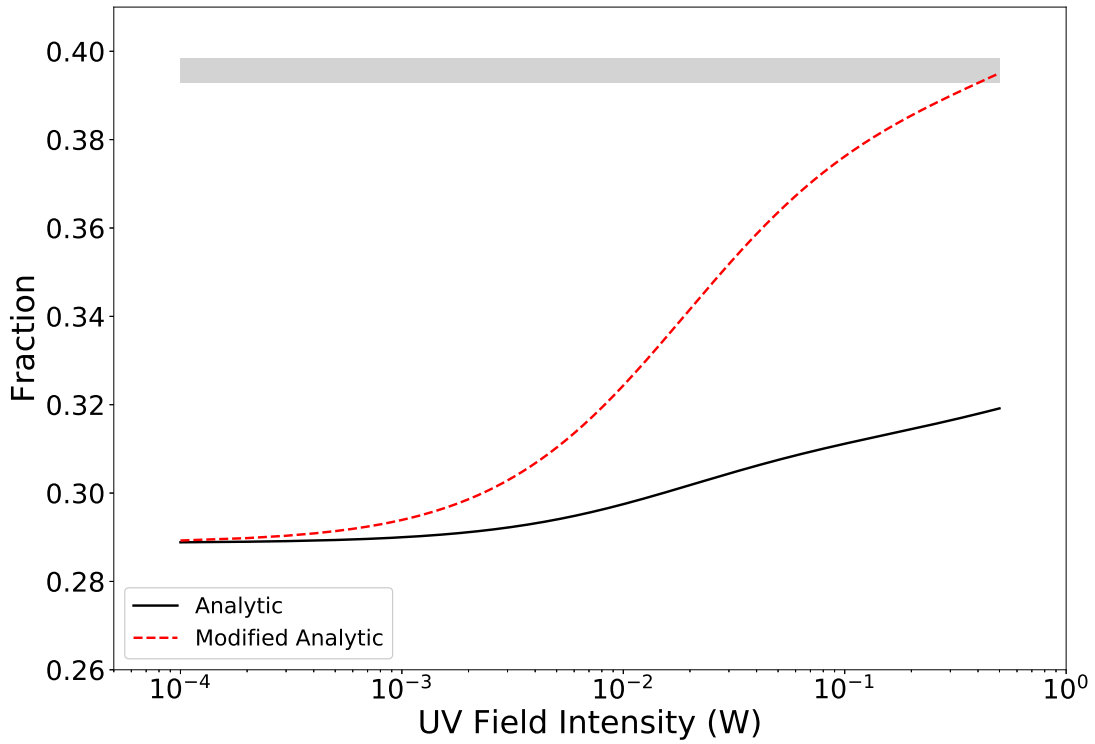


Figure 2.6: Fe XVII $3F$ fractions as a function of UV field intensity (W) for a 42,500 K blackbody (black solid line: analytic; red dashed line: analytic with ad hoc adjustment to \mathcal{R}_3^0). The gray stripe represents the envelope of the $3F$ fraction observed in ζ Pup.

Table 2.2: Most important $3s-3p$ transitions and their respective oscillator strengths f_{lu} and branching ratios R to levels other than the original lower level. The product $f_{lu}R$ gives the effective strength for changing the $2p-3s$ line ratios. The transitions with the largest $f_{lu}R$, that are therefore the most relevant for changing observed line ratios, are shown in bold.

Transition	f_{lu}	Energy (eV)	R	$f_{lu}R$
1→5	5.22E-02	30.318	0.0417	2.17E-04
3→5	2.30E-03	17.893	0.997	2.30E-03
1→6	5.35E-02	33.934	0.486	2.60E-02
1→7	1.68E-01	35.505	7.96E-10	1.33E-10
1→8	3.83E-03	36.705	0.939	3.60E-02
3→8	7.06E-04	24.076	0.999	7.05E-04
1→9	7.10E-02	38.510	0.424	3.01E-02
1→11	7.53E-05	46.023	0.998	7.51E-05
3→11	1.33E-01	33.394	0.572	7.61E-02
1→12	5.16E-03	49.234	0.878	4.54E-03
3→12	2.16E-01	36.605	0.438	9.47E-02
1→13	1.09E-03	49.639	0.983	1.07E-03

as a function of this potentially confounding variable.

Figure 2.4 compares the FAC CRM model and analytical model for the Fe XVII $3G$, $M2$, and $3F$ fractions as a function of temperature for a blackbody radiation field. The values of \mathcal{R}_i^0 in the analytical model were set from the FAC CRM calculations, but the dependence on UV flux was calculated using the FAC atomic data and blackbody flux. As expected, both plots exhibit an increase in the $3G$ line strength and a decrease in $M2$ line strength as temperature increases. In physical terms, UV photons are depopulating the upper $M2$ levels and therefore weakening it, while simultaneously enhancing the upper $3F$ and $3G$ levels. The small decrease in $3G$ around 30 kK is due to depopulation of level 3, the $J = 0$ metastable state, which has a lifetime about an order of magnitude longer than level 1. The dependence of the fractions from the analytical models on blackbody temperature is in excellent agreement with the FAC-calculated fractions.

Figure 2.5 shows a comparison of the same FAC CRM and analytical model $3F$ fractions as a function of blackbody temperature; the analytical model fractions were adjusted in two ways. First, the value of \mathcal{R}_4^0 was decreased to match the observed fraction of Capella, consistent with the findings of previous studies (Loch et al., 2006; Gu, 2008); then, we made a large ad hoc increase in the values of \mathcal{R}_3^0 , such that the dynamic range of the $3F$ fraction model would match that observed between Capella and ζ Pup. The factor of 4.125 increase in \mathcal{R}_3^0 required to produce such an effect is very unrealistic and is included to illustrate the point that theoretical uncertainties in the level populations at low UV flux are likely not sufficient to explain the observations.

Figure 2.6 compares the same analytic model curves as in Figure 2.5 to the observed ratio of ζ Pup, but as a function of geometrical dilution $W(r)$ for a blackbody with $T_{\text{eff}} = 42.5$ kK. The Fe XVII line emission from ζ Pup likely occurs throughout the wind over a range of dilution

factors, but with the strongest weighting for the relatively large dilution factors occurring within a few stellar radii, where the wind density is largest (Leutenegger et al., 2006).

2.3.3 Model Atmospheres

In § 2.3.2, we used the FAC CRM to calculate the strengths of the $3G$, $3F$, and $M2$ lines of Fe XVII for different values of geometrical dilution W for blackbodies with a range of temperature, and we derived fractional strengths for each line by dividing by the sum of all three line strengths (i.e., $3F / [3F + 3G + M2]$). Real stellar spectra are much more complex than the blackbodies typically used to model the effects of UV radiation fields on these ions in studies of atomic physics. We thus sought to further optimize our calculation by using UV field strength models more appropriate to OB stars.

Because most OB stars lie on sight lines having significant neutral interstellar gas, their EUV fluxes are not directly observable, and we must rely on model atmospheres. To this end, we utilized the TLUSTY OSTAR2002 and BSTAR2006 model atmosphere databases (Lanz & Hubeny, 2003, 2007). The OSTAR2002 grid contains datasets of spectral energy distributions (SEDs) typical of O stars covering a temperature range of 27.5 - 55 kK for the full set of frequency points used to calculate the model atmospheres. Similarly, the BSTAR2006 grid contains datasets of SEDs for B stars covering a 15 - 30 kK temperature range. UV fluxes from TLUSTY model atmospheres with effective temperatures ranging from 20 to 55 kK were used for the photoexcitation modeling. For $T_{\text{eff}} < 27$ kK, we used BSTAR2006 datasets with a surface gravity of $\log g = 3.00$, and for $T_{\text{eff}} > 27$ kK we used OSTAR2002 datasets with a surface gravity $\log g = 4.00$.

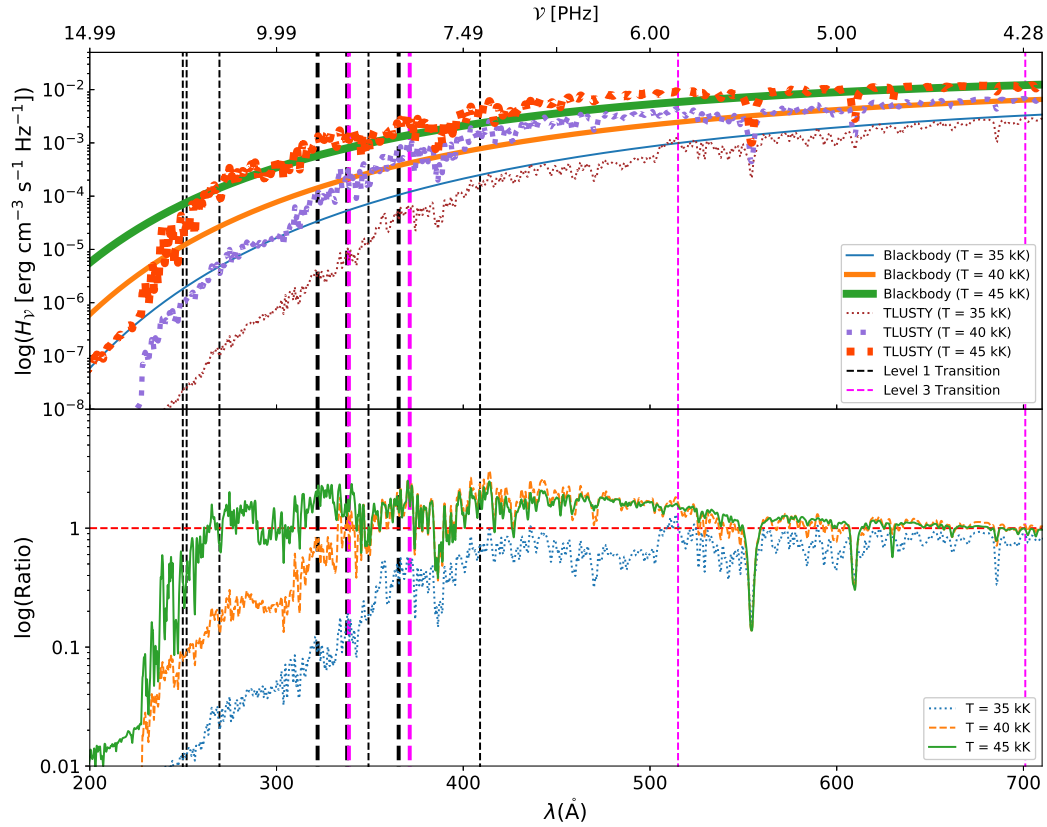


Figure 2.7: Top: comparison of $T = 35, 40, 45$ kK blackbody models (blue, orange, green respectively) and $T = 35, 40, 45$ kK, $\log g = 3.50$, Gaussian-broadened ($v = 10 \text{ km s}^{-1}$) stellar atmosphere models from TLUSTY (red, purple, brown, respectively) as a function of wavelength (\AA). Bottom: ratio of TLUSTY models to blackbody models with the same effective temperature as a function of wavelength. The vertical lines represent the wavelength of the Fe XVII $3s\text{--}3p$ transitions, with those originating from level 1 in black and those from level 3 in pink. The most important transitions are in boldface. The top axis shows the corresponding frequency range.

The top panel of Figure 2.7 illustrates the comparison between the blackbodies at various effective temperatures as a function of wavelength (\AA), while the bottom panel shows the ratio of the TLUSTY models to blackbody models for each effective temperature. The important $3s-3p$ transition wavelengths calculated with FAC are shown on the figure as vertical lines, with the most important subset shown in bold face. There are significant differences between the TLUSTY models and blackbody models of the same temperature, particularly in the 200 - 228 \AA range (shortward of the He II ionization edge). However, the relevant $3s-3p$ transition wavelengths are all longward of the He II edge. For 45 kK, the TLUSTY models have up to a factor of two more flux than the corresponding blackbody at the relevant wavelengths, while for 35 kK, the fluxes range from comparable to more than an order of magnitude less than the blackbody. Because of these differences, we compared both FAC CRM calculations and our analytical model using both blackbodies and TLUSTY model atmospheres, as shown in Figure 2.8. While the $3F$ fraction does show a somewhat steeper temperature dependence for TLUSTY models than for blackbodies, the basic behavior of the ratio as a function of temperature is unchanged.

2.4 Line Profile Model

The X-ray emission-line Doppler profiles of O stars have been successfully modeled by Owocki & Cohen (2001), with applications to *Chandra* and *XMM-Newton* spectra in, e.g., Cohen et al. (2010) and Cohen et al. (2014). The key parameter in this model is the characteristic optical depth $\tau_* \equiv \kappa \dot{M} / 4\pi v_\infty R_*$; here κ is the opacity of the dominant unshocked part of the wind, mainly due to continuum photoelectric absorption in few times ionized metals, \dot{M} is the mass-loss rate, v_∞ is the wind terminal velocity, and R_* is the stellar radius.

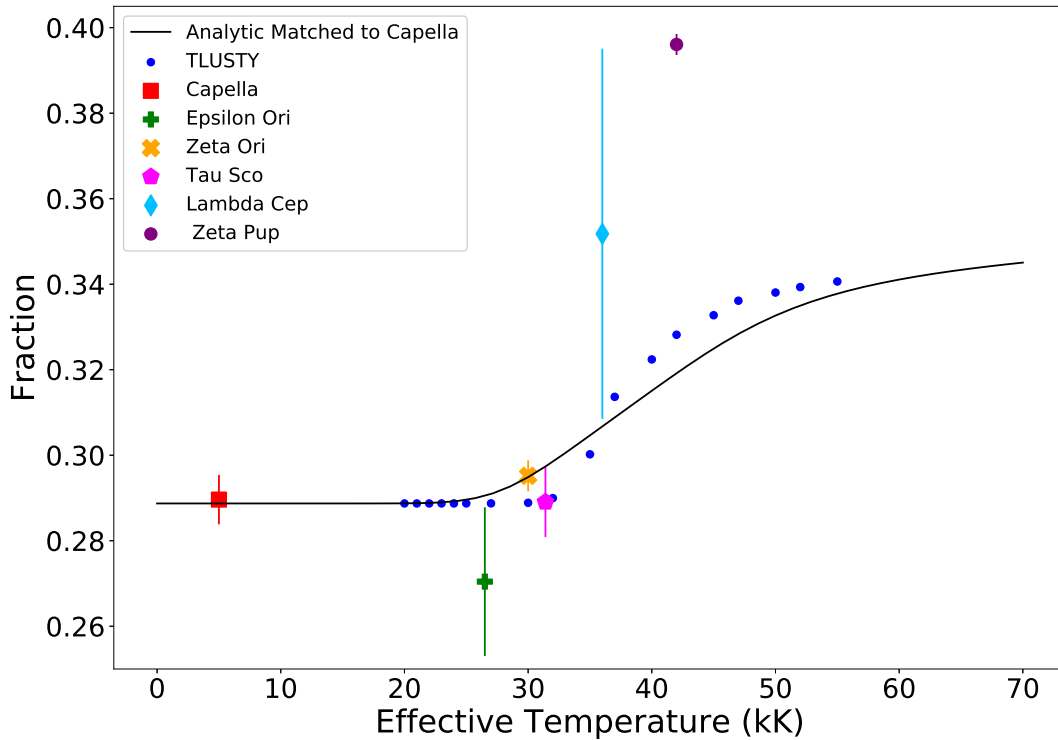


Figure 2.8: Comparison of observed and calculated Fe XVII $3F$ fractions as a function of stellar effective temperature. The black solid line represents the analytical model fraction from a blackbody, as previously shown in Figure 2.5, while the blue points represent the fractions calculated using TLUSTY model atmospheres. The TLUSTY fractions match the trends predicted by the UV flux ratios shown in Figure 2.7, as they are less than the analytical model ratios for $T < 35$ kK and are greater for $T > 40$ kK.

Leutenegger et al. (2006) extended this model to the $K\alpha$ transitions of helium-like ions by incorporating the radial dependence of the forbidden-to-intercombination line ratio as affected by UV photoexcitation, as in Equation 2.1.

We implemented a similar model to calculate line profiles for neon-like ions while including the radial dependence of the $3F$, $3G$, and $M2$ fractions. As in the case of the `windprof` and `hewind` models based on Owocki & Cohen (2001) and Leutenegger et al. (2006), the new `newind` model is implemented as an additive XSPEC local model.

`newind` can be used in one of two modes. In the first mode, the fractions are computed using a lookup table calculated directly with the FAC CRM module. In the second mode, the fractions are computed analytically, as in § 2.3.2.

Figure 2.9 shows comparisons of `newind` models with the same nominal parameters but different effective temperatures. The top panel compares a line profile with no UV field to a 70 kK blackbody calculated using the `newind` analytic model mode. We used the following fiducial parameters: $\tau_* = 1$, which is the characteristic continuum optical depth of the wind as defined in Owocki & Cohen (2001); X-ray emission onset radius $R_0 = 2R_*$; and wind terminal velocity $v_\infty = 2000 \text{ km s}^{-1}$. The bottom panel compares the same line profile with no UV field to TLUSTY model atmospheres with typical O-star effective temperatures: 27.5, 35, and 42.5 kK. For each TLUSTY model, we used $\log g = 4.00$.

As can be seen in the top panel, there is a noticeable but modest effect on the line profiles for the 70 kK blackbody, particularly in the $M2 + 3G$ blend. However, the UV field from typical O stars has only a weak effect on the line profiles and ratios, as shown in the bottom panel.

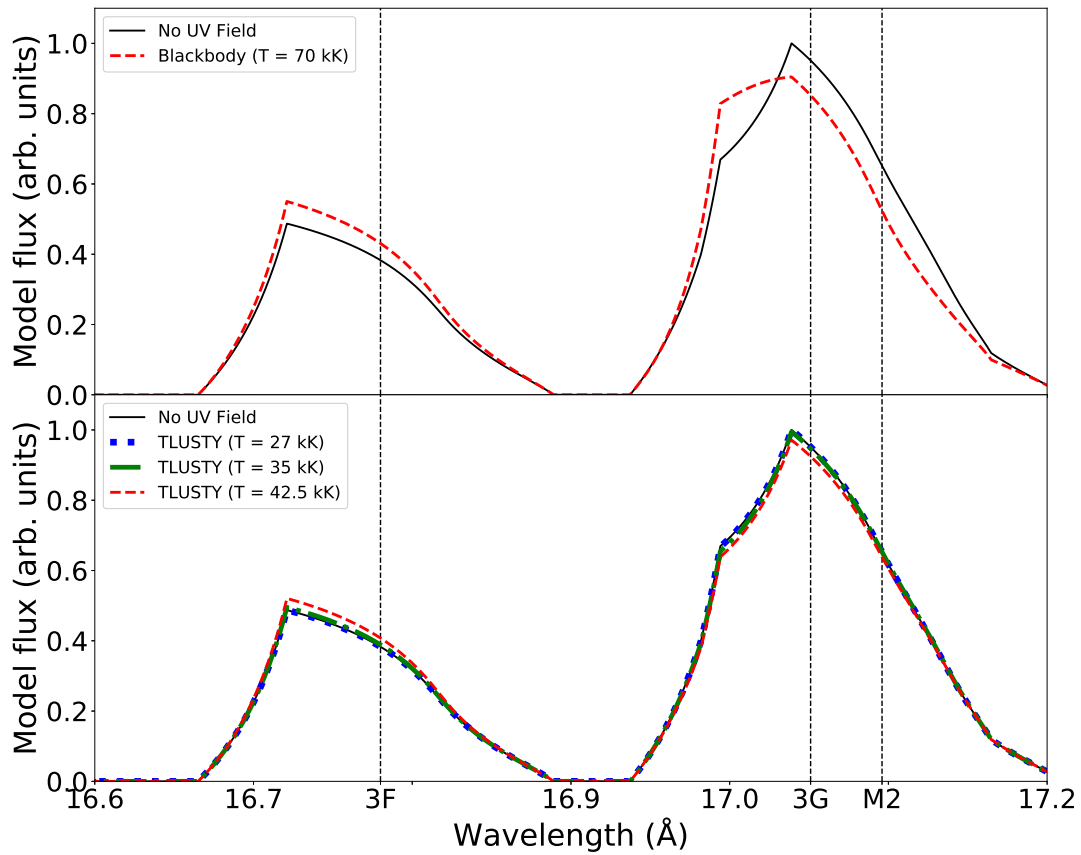


Figure 2.9: Comparisons of *newind* models with differing effective temperatures. Top: comparison of line profile with no UV field versus a blackbody with an effective temperature of 70 kK. Bottom: comparison of line profile with no UV field versus line profiles of TLUSTY model atmospheres with typical O-star effective temperatures (27.5, 35, 42.5 kK).

2.5 Model Fitting and Results

2.5.1 Observations and Data Reduction

We compared our model calculations to archival observations of coronal and hot stars taken by the *Chandra* HETGS and *XMM-Newton* RGS. We obtained archival X-ray spectra of the stars Capella, τ Scorpii, and EX Hydra as they provide well-resolved spectral lines and are statistically robust. We also obtained spectra of the O stars ζ Orionis, ϵ Orionis, ζ Puppis, and λ Cephei for the purpose of investigating the anomalous Fe XVII $2p - 3s$ line ratios in OB supergiants.

HETGS spectra of Capella, τ Sco, EX Hya, ζ Ori, and ϵ Ori were obtained from the *Chandra* archive and reprocessed using CIAO (*Chandra* Interactive Analysis of Observations) version 4.11 and CALDB (calibration database) version 4.8.4.1. RGS spectra of ζ Ori, τ Sco, ϵ Ori, λ Cep and ζ Pup were obtained from the *XMM-Newton* Science Archive and reduced using SAS (Science Analysis System) version 18.0. Table 2.3 shows a log of every star with their respective key physical parameters. The full list of spectral OBSIDs with corresponding exposure times is shown in Table A.1 in Appendix A. The spectra were fit using XSPEC version 12.10.1f (Dorman et al., 2003) using the `migrad` minimizer and the `cstat` fit statistic (Cash, 1979), which is appropriate for data following Poisson statistics.

We fit the archival spectra with a series of Gaussian models in order to derive values for the line strengths of the Fe XVII $3F$ (16.777 Å), $3G$ (17.051 Å), and $M2$ (17.096 Å) $2p - 3s$ transitions (Brown et al., 1998; May et al., 2005). We used 16.777 Å as the rest wavelength for the $3F$ transition, rather than the value of 16.780 Å given in Brown et al. (1998), as it agrees better with the observed wavelength of the transition in Capella.

Table 2.3: Log of key stellar parameters. The list of OBsIDs with corresponding exposure times is shown in Appendix A.1. ^ - UV flux of EX Hya may be higher than indicated by effective temperature (Mauche et al., 2001). Effective temperatures and surface gravities are taken from sources cited in the last column: N2003: Ness et al. (2003); P2016: Puebla et al. (2016); R2008: Raassen et al. (2008); M2001: Mauche et al. (2001), D2006: Donati et al. (2006); R2015: Rauw et al. (2015); L1993: Lamers & Leitherer (1993).

Star	T_{eff} (kK)	$\log g$ (cm s^{-2})	Ref.
Capella	5	-	N2003
ϵ Orionis	27	3.00	P2016
ζ Orionis	29.5	3.25	R2008
EX Hydrae	30 [^]	-	M2001
τ Scorpii	31.4	4.24	D2006
λ Cephei	36	3.50	R2015
ζ Puppis	42.5	3.75	L1993

The fits of Capella, τ Sco, and EX Hya act as a benchmark of the FAC calculations; Capella benchmarks FAC in the limit of low density and UV flux; τ Sco provides a check of the line ratios at modest UV flux; and EX Hya benchmarks the high-density regime (although the UV flux may also be nonnegligible). The four OB supergiants test the $3F$ line strength as a function of photospheric UV flux.

§ 2.5.2.1 describes the fitting results for Capella, τ Sco, and EX Hya, and § 2.5.2.2 describes the results for ζ Ori, ϵ Ori, ζ Pup, and λ Cep.

2.5.2 Fitting Results

2.5.2.1 Capella, τ Sco, and EX Hya

Figure 2.10 shows the Gaussian fits to X-ray spectra of the coronal star Capella from *Chandra* observations. Capella is a coronal star ($T_{\text{eff}} = 5000$ K) that has low UV flux and sufficiently low densities to serve as a benchmark for Fe XVII line ratios. We fit the spectra of three different *Chandra* observations of Capella in order to estimate the line strengths of the $3F$, $3G$, and $M2$ transitions. The results are mutually consistent, and the ratio we used in this work is a weighted average of these results.

τ Sco is a massive magnetic (Donati et al., 2006) B0V star ($T_{\text{eff}} = 31400$ K) with well-resolved spectral lines (Cohen et al., 2003; Mewe et al., 2003), making it a robust benchmark source. Furthermore, because of its nonnegligible UV flux, it is a good candidate to search for a possibly heretofore-overlooked weak effect on the line ratios. However, upon comparison, the star yielded very similar line ratios to Capella.

We also obtained line strengths from the spectra of the intermediate polar EX Hydra to

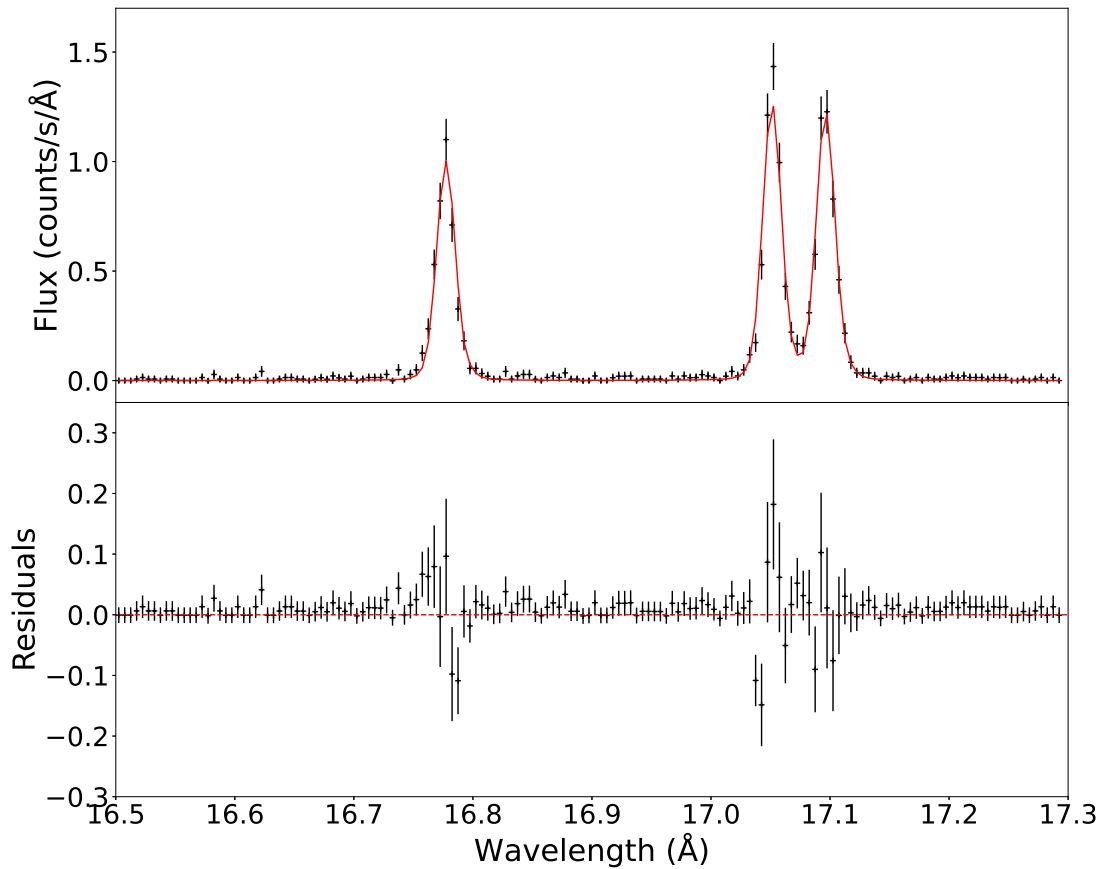


Figure 2.10: Capella MEG spectrum (black) fit with Gaussian models (red). The line strengths at 16.777, 17.051, and 17.096 Å were used to derive the Fe XVII $2p - 3s$ line ratios. There is no UV photoexcitation effect on the line strengths of Capella, making it a robust benchmark of this limit.

benchmark our fraction calculations in the limit of high electron density ($n_e \geq 3 \times 10^{14} \text{ cm}^{-3}$) and high UV field intensity. There was indeed good agreement between the FAC-predicted fraction calculations and the observed EX Hya $3F$, $3G$, and $M2$ fractions at high density, thus reaffirming the results of [Mauche et al. \(2001\)](#).

2.5.2.2 ζ Pup, λ Cep, ζ Ori, and ϵ Ori

Figure [2.11](#) shows our fits to the *XMM-Newton* RGS spectra of ζ Pup using `newind`. For this, we used the closest TLUSTY model to the estimated stellar parameters of ζ Pup, with $T_{\text{eff}} = 42.5 \text{ kK}$ and $\log g = 4.00$. We also used values for \mathcal{R}_i° fixed to the values of Capella. As expected, the model underpredicted the flux of $3F$ while overpredicting the blend of $3G$ and $M2$.

We also estimated the line strengths using Gaussian fits for comparison to predicted ratios in Figures [2.5](#) and [2.13](#). Figure [2.12](#) shows our fits to the *XMM-Newton* RGS spectra of ζ Pup using Gaussian models.

For comparison to stars of similar spectral type, we also fit Gaussians to the spectra of the OB supergiants ϵ Ori, ζ Ori, and λ Cep. [Rauw et al. \(2015\)](#) previously found a similar but weaker anomaly in the $2p - 3s$ line ratios of λ Cep as in ζ Pup. ζ Ori and ϵ Ori are statistically consistent with Capella, and our model predicts only a slight deviation with respect to Capella. λ Cep does have a somewhat stronger best-fit $3F$ fraction, but as it is also much fainter due to its larger distance, the statistical uncertainties on the fractions are large, and the spectrum is marginally consistent with the $3F$ fractions observed in both Capella and ζ Pup.

The uncertainties shown in Figures [2.5](#) and [2.13](#) are statistical only. A few systematic effects are possible, and we consider those here.

First, the weak continuum flux, mainly due to bremsstrahlung, is estimated by fitting nearby spectral regions that are free of lines. We tried changing the estimated continuum flux by $\pm 25\%$ and found systematic effects no larger than the statistical uncertainties.

Second, weak, blended lines might contaminate the ratio measurements. The most likely such lines would be from the Rydberg series of helium-like oxygen. We did not make a quantitative estimate of this effect, although given the strengths of the unblended lower- n lines in the series, it cannot be too important. We note that this should affect all of the massive stars about equally, so the difference in $3F$ fraction observed between ζ Pup and the other stars is still a robust conclusion.

Third, the line shapes of massive stars are not Gaussian but have a skewed shape resulting from differential absorption of distributed X-ray emission in their supersonic winds (Owocki & Cohen, 2001; Cohen et al., 2006). Nevertheless, the error in *total line flux* resulting from fitting a Gaussian to such lines is actually quite small, as can be seen in the residuals in Figure 2.12.

Finally, we have not accounted for differential wind absorption effects due to slightly different photoelectric continuum opacities at the respective wavelengths of $3F$, $3G$, and $M2$ (Leutenegger et al., 2010). Stars with higher wind optical depths at these wavelengths, such as ζ Pup, can be treated approximately in the exospheric limit, where the emergent flux at a given wavelength scales approximately inversely with the opacity. This scaling holds for arbitrarily high optical depth and thus gives an upper limit to the correction to the observed line ratios. We estimate this effect at approximately 5% between $3F$ versus $3G$ and $M2$. While this is a significant correction that partially mitigates the observed discrepancy, we stress that, by itself, it cannot solve the issue.

In Figure 2.13, we compare the fractions for ϵ Ori, ζ Ori, λ Cep, and ζ Pup to the

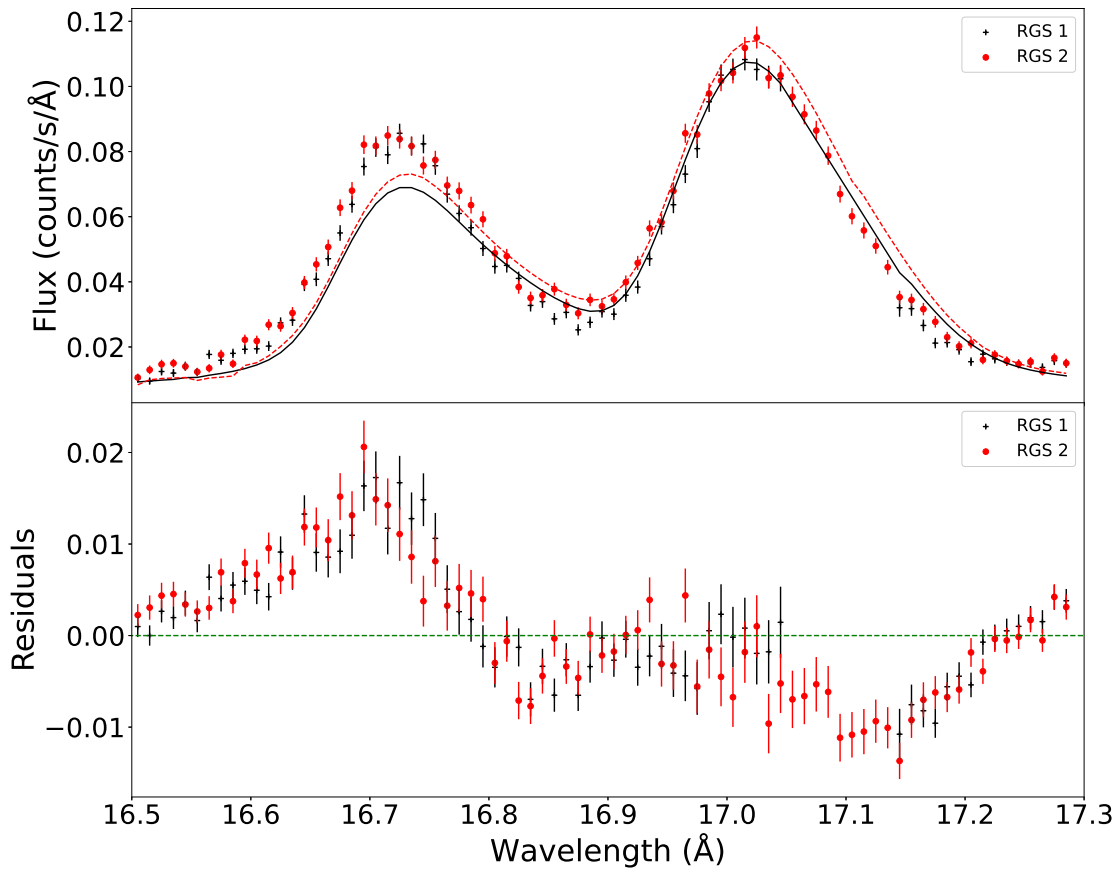


Figure 2.11: ζ Pup spectra from the *XMM-Newton* RGS fit with the `newind` model in analytical mode. The black plus signs represent the spectra from RGS1, and the red circles represent the spectra from RGS2.

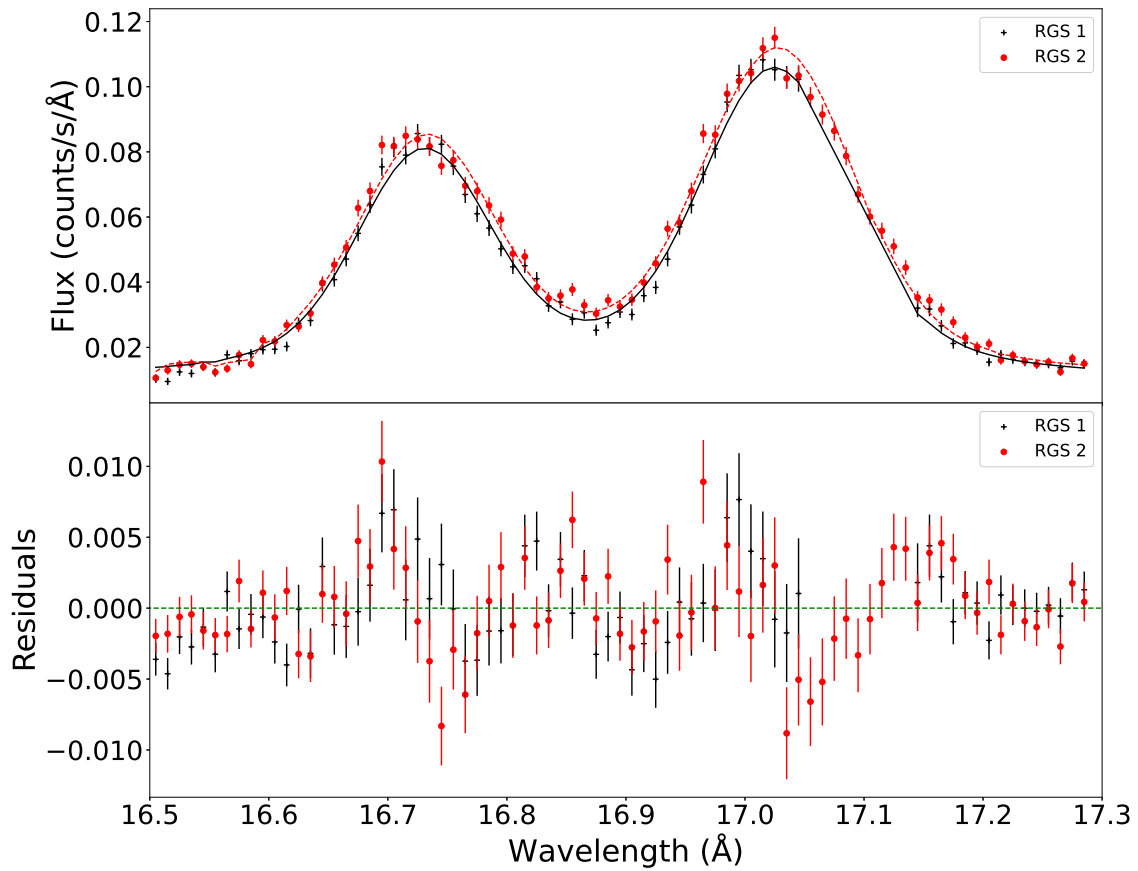


Figure 2.12: ζ Pup spectra from the *XMM-Newton* RGS fit with Gaussian models. The black plus signs represent the spectra from RGS1, and the red circles represent the spectra from RGS2.

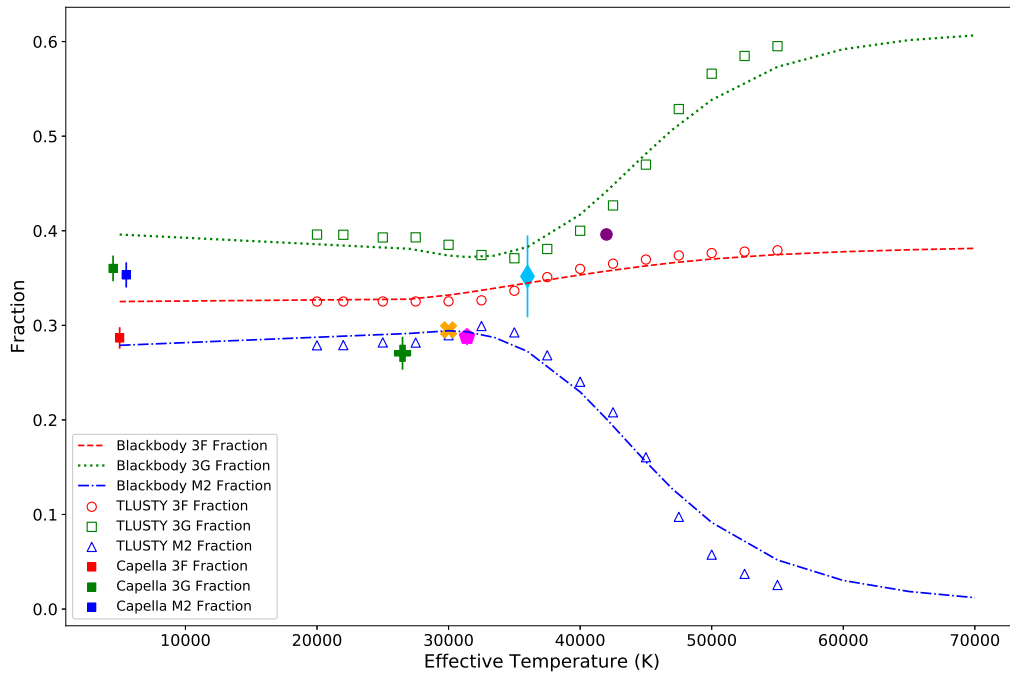


Figure 2.13: Fe XVII fractional line strengths as a function of UV field temperature. The dashed lines represent the FAC-calculated fractions; the open points represent the fractions calculated using TLUSTY model atmospheres (combination of BSTAR2006 and OSTAR2002 data sets); the leftmost points represent the observed 3*F*, 3*G*, and *M2* fractions of Capella ($T_{\text{eff}} = 5000$ K), and the larger symbols represent (left to right) the observed 3*F* fractions of ϵ Ori ($T_{\text{eff}} = 27000$ K), ζ Ori ($T_{\text{eff}} = 30000$ K), τ Sco ($T_{\text{eff}} = 31400$ K), λ Cep ($T_{\text{eff}} = 36000$ K), and ζ Pup ($T_{\text{eff}} = 42500$ K).

FAC-predicted fractions at maximum UV photoexcitation ($W = 0.5$) as a function of blackbody temperature. The fractional values for Capella are shown in Figure 2.13 to represent points in the limit of no photoexcitation. We examined the $M2 / (3F + 3G + M2)$ fraction as a diagnostic of the quality of our line intensity calculations. We observed a $\sim 20\%$ model-data discrepancy for the $M2$ fraction, which is consistent with the discrepancies found in similar previous studies (see § 2.2).

However, the FAC-predicted $3F$ fraction calculation does not accurately reproduce the observed ratios. As stated in § 2.3, the FAC-predicted dynamic range for the $3F$ fraction (as a function of temperature) is not large enough to explain the observed ratio difference between Capella and ζ Pup.

2.6 Discussion

The discrepancy between the measured Capella and τ Sco $M2$ fractions and our FAC CRM fraction calculations is approximately 20%, which is consistent with several previous studies that examined these line ratios (Loch et al., 2006; Gu, 2008). However, the discrepancy between the $3F$ fractions of Capella and ζ Pup is both significant and surprising.

We were unable to reproduce the observed difference between the ratios of the two stars in the FAC-predicted dynamic range of the ratios as a function of UV field intensity. As illustrated in Figure 2.13, the dynamic range of the calculated $3F$ fraction is less than what we observed between Capella and ζ Pup.

We considered several other possible atomic and astrophysical processes in attempts to potentially explain the discrepancy in the $3F / (3F + 3G + M2)$ fraction in ζ Pup.

We considered possible contamination from fluorine lines, as the wavelengths of the strongest hydrogen-like and helium-like fluorine lines are very close to the wavelengths of the $2p - 3s$ and $2p - 3d$ Fe XVII transitions (Beiersdorfer et al., 2017). Fluorine typically has a very low abundance in most astrophysical objects, and its lines are thus usually negligible in X-ray spectra. But as ζ Pup is known to show strong surface enhancement of nitrogen from CNO processed material (e.g., Bouret et al., 2012), one might speculate that fluorine could also be enhanced through higher-temperature analogs of the CNO cycle. We tried including the lines of helium-like F VIII using the `hewind` model in conjunction with the $2p - 3s$ lines of Fe XVII in our model fitting, but we found that the model fit strongly preferred to have zero intensity for fluorine lines, and forcing the fluorine line flux to be nonnegligible produced clearly unacceptable model fits. We thus conclude that the fluorine abundance is indeed negligible, and fluorine lines cannot explain the anomalous $3F$ line strength in ζ Pup.

We also considered resonant Auger destruction (Liedahl, 2005) of the $3G$ and/or $M2$ lines by $2p - 3d$ transitions in the low charge states of Fe dominant in the bulk of the wind, likely Fe IV-VI, as proposed in Leutenegger et al. (2012). The $2p - 3d$ transition energies for these charge states are in the range 17.0-17.2 Å, but are not sufficiently well known to evaluate the degree of coincidence with $3G$ and $M2$ (Gu et al., 2006; Blancard et al., 2018), so it is not possible to confirm or rule out this possibility. For this effect to explain the observed ratio of Fe XVII $2p - 3s$ lines in ζ Pup while having a negligible effect for other OB stars, the relevant transition would have to be in a charge state of iron that is more prevalent in the wind of ζ Pup than for other stars.

Beiersdorfer et al. (2003) showed that strong magnetic fields can induce direct decay of the $J = 0$ $3s$ excited state to ground; the transition wavelength of 16.804 Å is close enough to the wavelength of $3F$ that for the velocity broadened winds of OB stars, the flux of this transition

would blend with $3F$. Thus, this could effectively remove photons from $3G$ and appear to feed $3F$. This is unlikely to be relevant for ζ Pup, since the required magnetic field to produce an effect is ~ 50 kG, while observational limits to the photospheric magnetic field strength of ζ Pup are at the level of ~ 30 G for a global dipole configuration (David-Uraz et al., 2014), or \sim kG for small-scale disordered fields (Kochukhov & Sudnik, 2013). Furthermore, as we showed in § 2.3, the rate of feeding of the $J = 0$ $3s$ excited state is not sufficient to explain the enhanced strength of $3F$.

We showed in § 2.3 that strongly adjusting the relative rate of population of the $J = 0$ $3s$ excited state could produce a sufficient dynamic range in the strength of $3F$ to explain the observed ratio in ζ Pup. There is no reason to think that FAC should strongly underestimate this rate, but one might suspect that perhaps inadequate treatment of configuration mixing might cause such an issue. We therefore tested the impact of including mixing between the ground state and singly excited states with $n = 3, 4$ and $n = 3, 4, 5$, such that the calculation includes the levels arising from the $2s^22p^6$, $2s2p^6nl$, and $2s^22p^5nl$ configurations. The calculations including more mixing had only a very small effect on the dynamic range of $3F$ and the population of the $J = 0$ $3s$ excited state. Although configuration mixing is known to converge rather slowly, the most important effects should occur when including the levels we studied, so the absence of a significant improvement in agreement with observations indicates that this is not the origin of the discrepancy.

Pollock (2007) has suggested that charge exchange (CX) could be important in O-star winds. One might suppose that this could alter the line ratios of Fe XVII in a way that might reproduce the observations, although it would not be clear why this should preferentially affect ζ Pup over other O stars. Betancourt-Martinez et al. (2018) have measured X-ray spectra of neon-

like Ni, which can be taken as a crude proxy for the expected spectrum of neon-like Fe. Their measurements show that the $M2$ line is dominant and that this is a simple consequence of cascade probabilities for most of the highly excited states populated by CX. If CX were important in the wind of ζ Pup, this would thus only enhance the discrepancy between modeled and observed $2p - 3s$ line ratios. We thus conclude that CX is likely negligible, and in any case cannot explain the anomalous strength of $3F$ in ζ Pup.

Considering the thorough measures incorporated by previous studies (see § 2.2), we believe that using a more comprehensive model would not significantly change the dynamic range of $3F / (3F + 3G + M2)$. A better model would likely enhance feeding of $3G$ and $M2$ (for all UV fluxes) and thus produce better agreement for, e.g. Capella, as shown in Gu (2008). However, these improvements would not completely mitigate the model-data discrepancy.

In terms of future directions, laboratory astrophysics experiments could be the key to solving the model-data discrepancy. A potential future study could improve the FLASH-EBIT measurements (Shah et al., 2019) to derive better constraints for the Fe XVII $3s$ cross section by using, for example, a high-resolution wide-band X-ray microcalorimeter. Furthermore, a potential future laboratory experiment could use simultaneous EUV and X-ray spectroscopy to benchmark the importance of the $3s J = 0$ level in feeding the upper level of the $3G$ line, as well as the relative strengths of the $3s - 3p$ transitions. If the modeled rate of the feeding of the $3s J = 0$ level were strongly underestimated, this may potentially reconcile the discrepancy.

2.7 Conclusions

We used the FAC collisional-radiative model to model the effect of UV photoexcitation from O stars on the Fe XVII $2p-3s$ line ratios. We solved the rate equations, deriving an analytical model to calculate the ratios as a function of UV field intensity using parameters derived from the FAC CRM, experiments, and astrophysical observations. Using these models, we demonstrated that the UV field intensities of O stars have at most a marginal effect on the line ratios. We also implemented a line profile model for Fe XVII in the spectra of O stars, called `newind`, in analogy with the `hewind` model of [Leutenegger et al. \(2006\)](#), where the profiles are calculated including the radial dependence of the $2p-3s$ ratios.

We compared our model calculations to archival observations of coronal and hot stars taken by *Chandra* and *XMM-Newton*. The comparison with Capella showed model-data discrepancies consistent with ones found in previous studies. More importantly, the dynamic range of the model $3F$ fraction as a function of UV field intensity was not large enough to explain the observed difference in this ratio between Capella and ζ Pup. We conclude that UV photoexcitation has only a weak effect on the line ratios of Fe XVII in O stars and that it cannot explain the observed strength of $3F$ in ζ Pup. Future laboratory experiments could potentially use simultaneous EUV and X-ray spectroscopy both to place constraints on the Fe XVII $3s$ cross sections and to benchmark the importance of the $3s J = 0$ level in feeding the upper level of the $3G$ line by measuring the strength of the 1153 \AA line relative to the strengths of the $2p-3s$ lines.

2.8 Acknowledgments

We thank Ming Feng Gu for stimulating discussions. We thank Ehud Behar and an anonymous referee for their helpful comments. We acknowledge support from NASA's Astrophysics division. G.G. acknowledges support under NASA award No. 80GSFC21M0002. C.S. acknowledges the support by an appointment to the NASA Postdoctoral Program at the NASA Goddard Space Flight Center, administered by Universities Space Research Association under contract with NASA, by the Lawrence Livermore National Laboratory (LLNL) Visiting Scientist and Professional Program Agreement No.s VA007036 and VA007589, and by Max-Planck-Gesellschaft (MPG).

Chapter 3: Laboratory Benchmark of $n \geq 4$ Dielectronic Recombination Satellites of Fe XVII¹

3.1 Introduction

Some of the strongest features in the X-ray spectra of many collisional plasma sources, including coronal and massive stars, galaxy clusters, the interstellar medium, and X-ray binaries (Parkinson, 1973; Smith et al., 1985; Schmelz et al., 1992; Waljeski et al., 1994; Phillips et al., 1996; Behar et al., 2001a; Mauche et al., 2001; Doron & Behar, 2002; Xu et al., 2002; Gu, 2003; Paerels & Kahn, 2003; Werner et al., 2009; Pradhan & Nahar, 2011; Beiersdorfer et al., 2018; Gu et al., 2020) are due to the Fe-L complex. It encompasses radiative transitions from $n = 2$ states of Na-like (Fe XVI) to Li-like (Fe XXIII) Fe ions, primarily excited by electronic impact, recombination, and ionization (Gu et al., 2019). Within this complex, and due to its closed-shell configuration and correspondingly high ionization potential (Smith et al., 1985), neon-like Fe XVII displays some of the brightest spectral signatures of any highly charged ion seen in hot astrophysical plasmas. Their spectra at temperatures of a few MK are dominated by the L-shell transitions of Fe XVII ions in the 15 – 18 Å range, and specifically the $3d - 2p$ and $3s - 2p$ transitions (Parkinson, 1973; Canizares et al., 2000; Behar et al., 2001a; Xu et al., 2002; Paerels

¹Published in *The Astrophysical Journal* Vol. 971 as "Laboratory Benchmark of $n \geq 4$ Dielectronic Recombination Satellites of Fe XVII" by G. J. Grell, M. A. Leutenegger, P. Amaro, J. Crespo López-Urrutia, and C. Shah

& Kahn, 2003).

These transitions also provide very useful diagnostics of the physical conditions in such plasmas, including electron temperature as well as density, velocity turbulence, and X-ray opacity (Behar et al., 2001a; Mewe et al., 2001; Paerels & Kahn, 2003; Kallman et al., 2014; Beiersdorfer et al., 2018; Grell et al., 2021). Decades of laboratory measurements have yielded accurate wavelengths, cross sections, and intensity ratios of those transitions (Brown et al., 1998; Brown et al., 2001; Brown et al., 2001; Beiersdorfer et al., 2002; Beiersdorfer et al., 2004; Brown et al., 2006; Gillaspy et al., 2011; Beiersdorfer et al., 2017a; Shah et al., 2019, 2024). However, their diagnostic utility is hampered by the clear discrepancies between observations, laboratory measurements, and theoretical calculations of their relative line intensities that were found. One of the key line formation mechanisms for Fe XVII in hot plasmas, direct electron-impact excitation (DE), has exhibited 10 – 20% model-data disparities for the $3d - 2p$ cross sections in numerous studies over several decades (Brown et al., 1998; Laming et al., 2000; Brown et al., 2001; Beiersdorfer et al., 2002; Beiersdorfer et al., 2004; Brown et al., 2006; Gillaspy et al., 2011; Beiersdorfer et al., 2017b; Shah et al., 2019). This suggests measuring other key line formation processes such as dielectronic recombination with better constraints in order to find a plausible explanation for these persistent discrepancies.

Dielectronic recombination (DR) is the strongest electron-ion recombination process for Fe XVII in most photoionized and collisionally ionized astrophysical plasmas (Burgess, 1964), producing satellite lines to the $3d - 2p$ transition lines through resonant electron capture and subsequent radiative decay. As shown by Zatsarinny et al. (2004), the DR process for Fe XVII can be represented as

$$\begin{aligned}
2s^2 2p^6 + e^- &\Leftrightarrow \begin{cases} 2s^2 2p^5 n l n' l' \\ 2s 2p^6 n l n' l' \end{cases} \\
&\rightarrow \begin{cases} 2s^2 2p^5 3l + e^- \text{ (autoionization)} \\ 2s^2 2p^6 n'' l'' \text{ (DR)} \end{cases}
\end{aligned} \tag{3.1}$$

For the Fe XVII *LMM* ($2p^5 3l 3l'$) channel, an electron is captured into the vacant M ($n = 3$) shell while an electron is simultaneously excited from the L ($n = 2$) shell to the M ($n = 3$) shell. The resulting doubly excited state is denoted as *LMM* to reflect the intermediate-state configuration of the Na-like Fe ion. Understanding whether its contributions to Fe XVII line formation are causing the model-data discrepancy is essential for improving plasma diagnostics. Validations of these contributions also benchmarking state-of-the-art collisional-radiative models and atomic databases such as SPEX (Kaastra et al., 1996b), AtomDB (Foster et al., 2012), and CHIANTI (Del Zanna, G. et al., 2015), which themselves will be needed to interpret observations from the Athena X-IFU (Barret et al., 2016), LEM (Bandler et al., 2023), and Arcus (Smith et al., 2016) high-resolution X-ray imaging spectrometers.

In this work, we use the Flexible Atomic Code (FAC) to calculate line emission cross sections for the Fe XVII DR, DE, and resonant excitation (RE) channels with configurations including principal and orbital angular momentum quantum numbers up to $n \leq 7$, $n' \leq 100$, and $l, l' \leq 8$ respectively, and we benchmark these predictions using experimental cross sections in Fe XVII ions that were mono-energetically excited in an electron beam ion trap (EBIT) (Levine et al., 1988). In particular, we focus on the cross sections for the higher X-ray energy $n \geq 4$

satellites of Fe XVII observable in the experimental data. § 3.2 describes the EBIT experiment and previous analyses of our measurements. § 3.3 describes our atomic model calculations. § 3.4 describes the data calibration and shows the theory-experiment comparison and analysis. In § 3.5 we further discuss our results and future directions.

3.2 Experiment

We used FLASH-EBIT (Epp et al., 2010) at the Max Planck Institute for Nuclear Physics in Heidelberg, Germany (MPIK) to produce a high-purity ion population mainly consisting of Fe XVII ions (Shah et al., 2019). A molecular beam of iron pentacarbonyl was injected into the trap through a differentially-pumped injection system, ionized to high charge states by successive electron impact using a mono-energetic and unidirectional electron beam, and compressed by a 6-T magnetic field produced by superconducting Helmholtz coils. The resulting ions were radially trapped by the negative space charge of the compressed electron beam and electrostatically confined in the axial direction by potentials applied to the surrounding cylindrical drift tubes.

For this experiment, the electron-beam energy was swept over the range containing the Fe XVII dielectronic capture resonances. The ion population was optimized by applying a charge-breeding time of 0.5 seconds at 1150 eV, followed by a 40 ms-long ramp-down to 300 eV and a symmetric ramp-up. This maximizes the Fe XVII purity by efficiently suppressing lower charges states. The electron-beam current was synchronously varied following the relation $n_e \propto I_e/\sqrt{E_e}$ (Savin et al., 2000) in order to maintain a constant electron density in the trap. The electron current was set to 20 mA at the breeding period, and 10 mA at the lowest energy. The radiative decay of the excited states generated X-ray photons, which were then collected at 90° to the

electron-beam axis using a silicon-drift detector (SDD) with a photon-energy resolution of ~ 120 eV FWHM at 1000 eV. The unidirectional electron beam causes anisotropic, polarized X-ray emission from the trapped ions (Beiersdorfer et al., 1996; Shah et al., 2015; Shah et al., 2018).

In previous works, we measured line emission cross sections for the $3s - 2p$ and $3d - 2p$ channels of Fe XVII ions formed through DR, RE, DE, and radiative cascades following RR, as well as intensities and cross sections of Fe DR L-shell satellites for the $LMn (2p^5 3lnl' \rightarrow 2p^6 3l)$ series for Fe XVII (Shah et al., 2019). These measurements improved on previous experiments (Brown et al., 1998; Beiersdorfer et al., 2017b) by reducing the collision-energy spread to only 5 eV full-width-at-half-maximum (FWHM) at 800 eV. We also obtained experimental resonant strengths and rate coefficients for the DR $LMM (3l3l')$ satellites of Fe XVII (Grilo et al., 2021). The calculated rate coefficients were compared with those available in the OPEN-ADAS and AtomDB (Foster et al., 2012) databases, both of which are frequently used in spectral analyses, ultimately unveiling disparities of 9 – 12% and $\sim 5\%$ respectively.

3.3 Electronic-Structure Calculations

We extend the work of Shah et al. (2019) by calculating cross sections for all DR satellite lines of Fe XVII observable in the FLASH-EBIT experiment. We used the Flexible Atomic Code (FAC) (Gu, 2008) to obtain the electronic structure for the initial, intermediate, and final states of Fe XVII ions, as well as their transition and autoionization rates. In order to match the polarized experimental emission, we fed these atomic data into the line-polarization module of FAC (FAC-*pol*), which computes line polarizations resulting from the uni-directional electron beam, to then calculate the differential (observed at 90°) and total line emission cross sections for

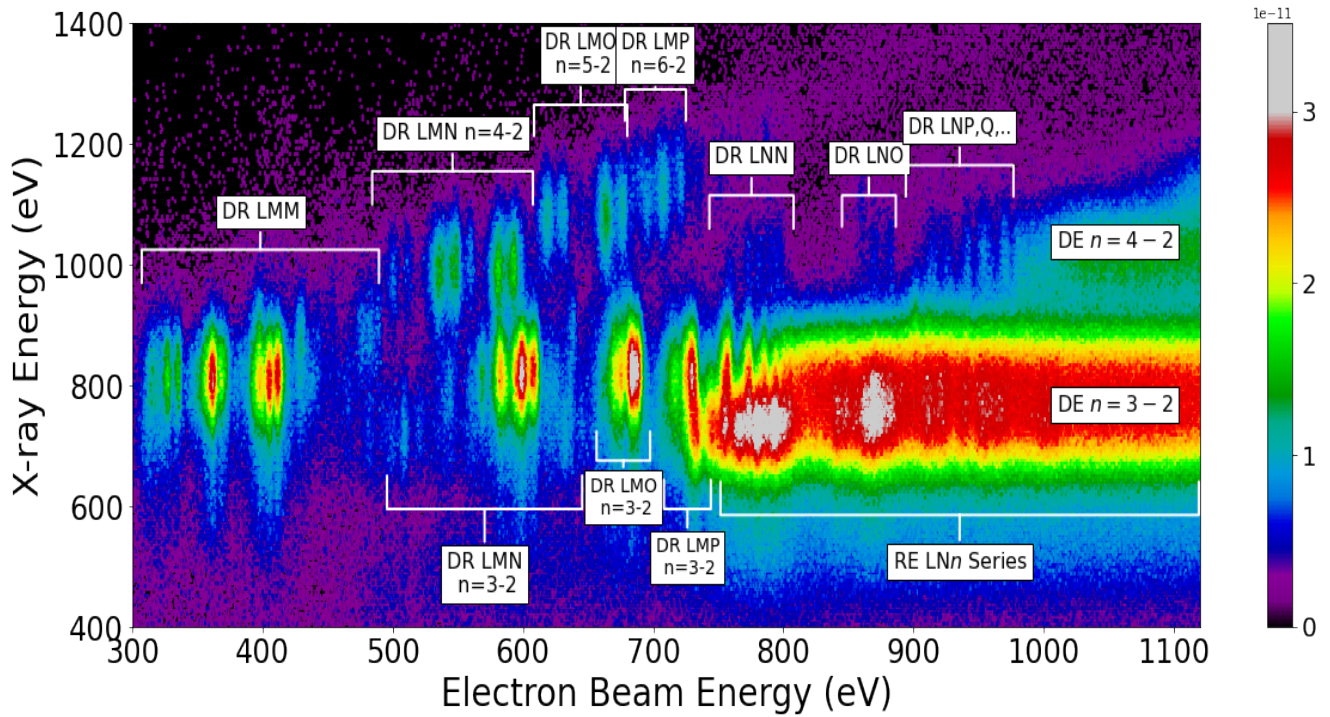


Figure 3.1: X-ray photon flux from the FLASH-EBIT experiment as a function of photon energy and electron-beam energy. The labelled features represent resonances formed through dielectronic recombination (DR), resonant excitation (RE), and direct electron-impact excitation (DE) at Fe XVII transition lines. The LMn and LNn series represent the $3lnl'$ and $4lnl'$ L-shell satellites of Fe XVII respectively. For clarity of visualizing all peaks, the color-bar scales represent the square root of the differential cross section values for the experimental data.

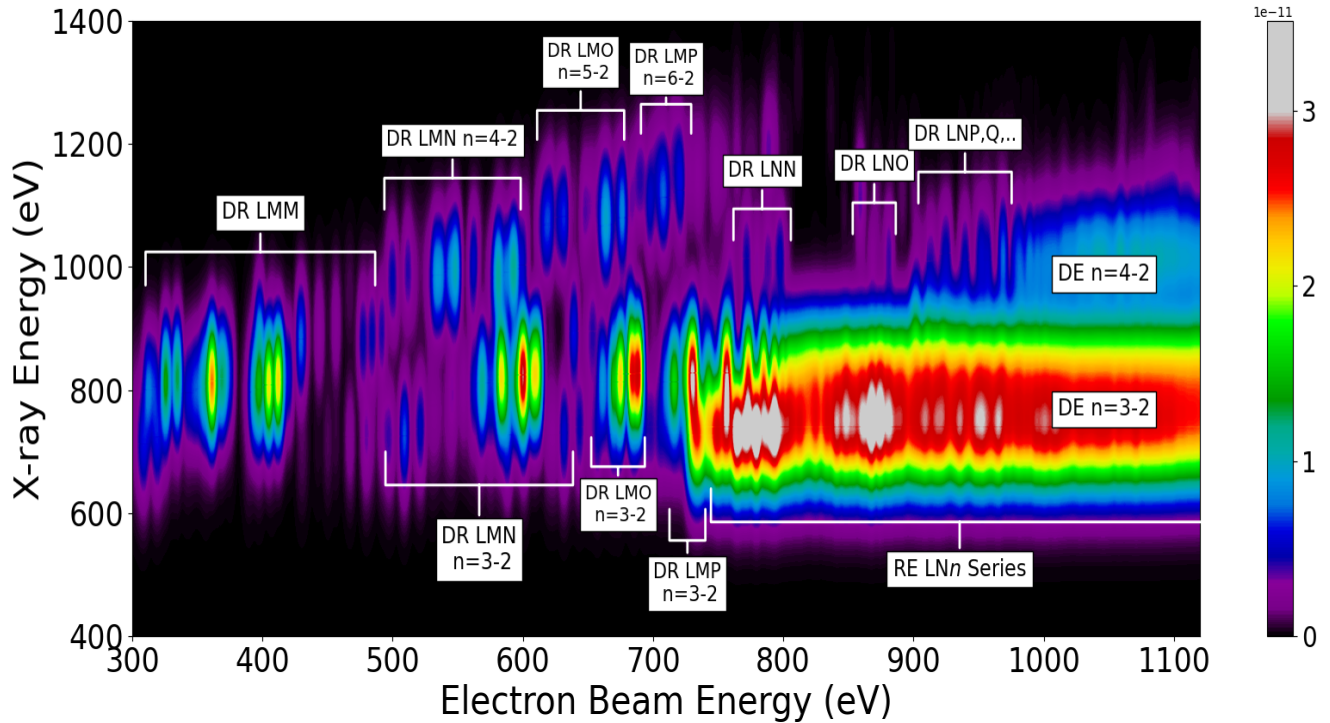


Figure 3.2: X-ray photon flux from the doubly convolved FAC calculations as a function of photon energy and electron-beam energy. The labelled features represent resonances formed through dielectronic recombination (DR), resonant excitation (RE), and direct electron-impact excitation (DE) at Fe XVII transition lines. The LMn and LNn series represent the $3ln'$ and $4ln'$ L-shell satellites of Fe XVII respectively. For clarity of visualizing all peaks, the color-bar scales represent the square root of the differential cross section values for the doubly convolved theoretical data. For direct comparison with the experimental spectrum, FAC-calculated cross sections were convolved along both the electron-beam energy and photon-energy axes to match the resolution of the nearly mono-energetic electron beam of FLASH-EBIT (~ 5 eV FWHM) and the photon-energy resolution of the used silicon-drift detector (~ 120 eV FWHM). See Section 3.4.3 for further details.

each region-of-interest (ROI).

We performed calculations for the dielectronic capture channels of DR, RE, and DE by including $2s^22p^5nl n'l'$ configurations with principal quantum numbers and orbital angular momentum quantum numbers up to $n \leq 7$, $n' \leq 100$, and $l, l' \leq 8$ respectively, and allowing full-order configuration mixing. In doing so, we accounted for all DR LMn and LNn ($2p^54lnl' \rightarrow 2p^64l$) satellites resolvable in our experiment. We calculated the DR resonant strengths in the isolated resonance approximation as in previous studies (Shah et al., 2019; Grilo et al., 2021), meaning we assumed no quantum interference between DR resonances or with non-resonant recombination channels (Pindzola et al., 2006; Zatsarinny et al., 2005). In this approximation, the DR strength is

$$S_{idf}^{DR} = \int_0^\infty \sigma_{idf}^{DR}(E_e) dE_e = \frac{\pi^2 \hbar^3}{m_e E_{id}} \frac{g_d}{2g_i} \frac{A_{di}^a A_{df}^r}{\sum_{i'} A_{di'}^a + \sum_{f'} A_{df'}^r} \quad (3.2)$$

where $\sigma_{idf}^{DR}(E_e)$ is the DR cross section as a function of the free-electron kinetic energy E_e , m_e is the electron mass (in units MeV/c^2), \hbar is the reduced Planck constant, and E_{id} is the resonant energy of the electron-ion recombination between the initial state i and intermediate doubly excited state d with statistical weights g_i and g_d . A_{di}^a and A_{df}^r represent the autoionization rate between states d to i and radiative transition rate between state d and the final state f respectively, which were both calculated with FAC.

3.4 Data Analysis and Results

3.4.1 Data Calibration

We calibrated the experimental data first by correcting for the filter transmission resulting from the 1 μm carbon foil in front of the SDD, which shields it from UV light but also blocks a part of the X-ray radiation from the trap. We calculated the transmission using optical constants from [Henke et al. \(1993\)](#). [Shah et al. \(2019\)](#) verified the filter transmission through Ly α and radiative recombination emission measurements of well-known ions O VIII and Ne X, finding agreement within 3%. We include this uncertainty in our error budget.

As described in § 3.2, the beam current I_e was adjusted while the electron-beam energy E_e was changed in order to maintain a constant electron density n_e . Since the X-ray intensity is proportional to the electron beam current density j_e , which in turn depends on the product of beam current and the square root of its energy ([Wong et al., 1995](#)), we corrected the observed X-ray count rate by dividing by a factor of $\sqrt{E_e}$.

We also calculated a correction for the nominal SDD energy scale. Using calculated centroid-photon energies for both the FAC-calculated and FLASH-measured resonances, we fit a linear model to calculate the gain correction. We used the centroid-photon energies for the $3s$, $3d$, and $4d$ manifolds for the linear fit in addition to the origin. We calibrated the electron-beam energy using the *LMM* and *LMN* $n = 3 - 2$ DR resonant energies ([Beiersdorfer et al., 2014](#)), both of which are well known theoretically.

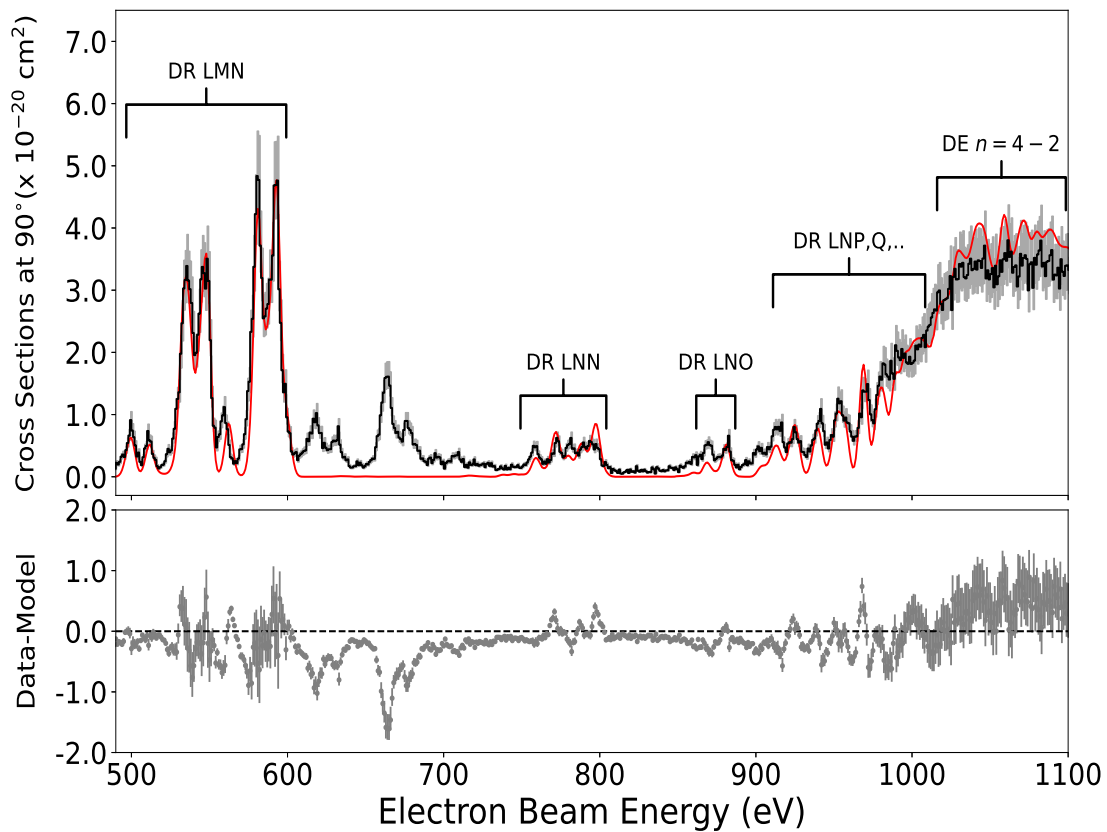


Figure 3.3: Experimental cross sections observed at 90° (black curve) versus FAC-calculated absolute cross sections (red curve) as a function of electron-beam energy for the Fe XVII *LMN* $n = 4 - 2$ channels within the 980 - 1030 eV photon-energy range. The shaded gray bands represent the 1σ uncertainty (systematic and statistical) for the experimental cross sections.

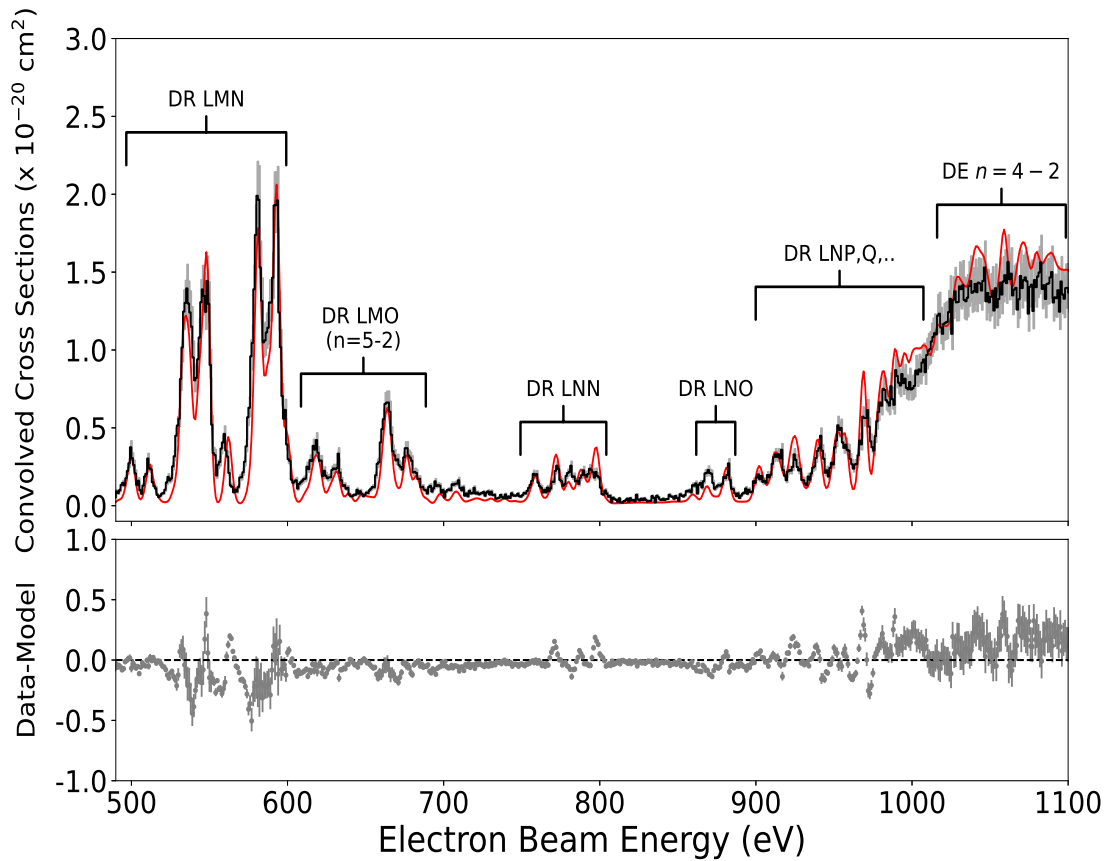


Figure 3.4: Experimental cross sections observed at 90° (black curve) versus doubly convolved theoretical FAC cross sections (red) for the Fe XVII *LMN* $n = 4 - 2$ channels within the 980 - 1030 eV photon-energy range. The features missing in the absolute cross section plot (mostly due to *LMO* $n = 5 - 2$ transitions) at 600 - 700 eV are now visible after matching the photon-energy resolution of the FLASH-EBIT silicon-drift detector. These *LMO* cross section values are arbitrary since the ROI is not centered on those photon energies. The shaded gray bands represent the 1σ uncertainty (systematic and statistical) for the experimental cross sections.

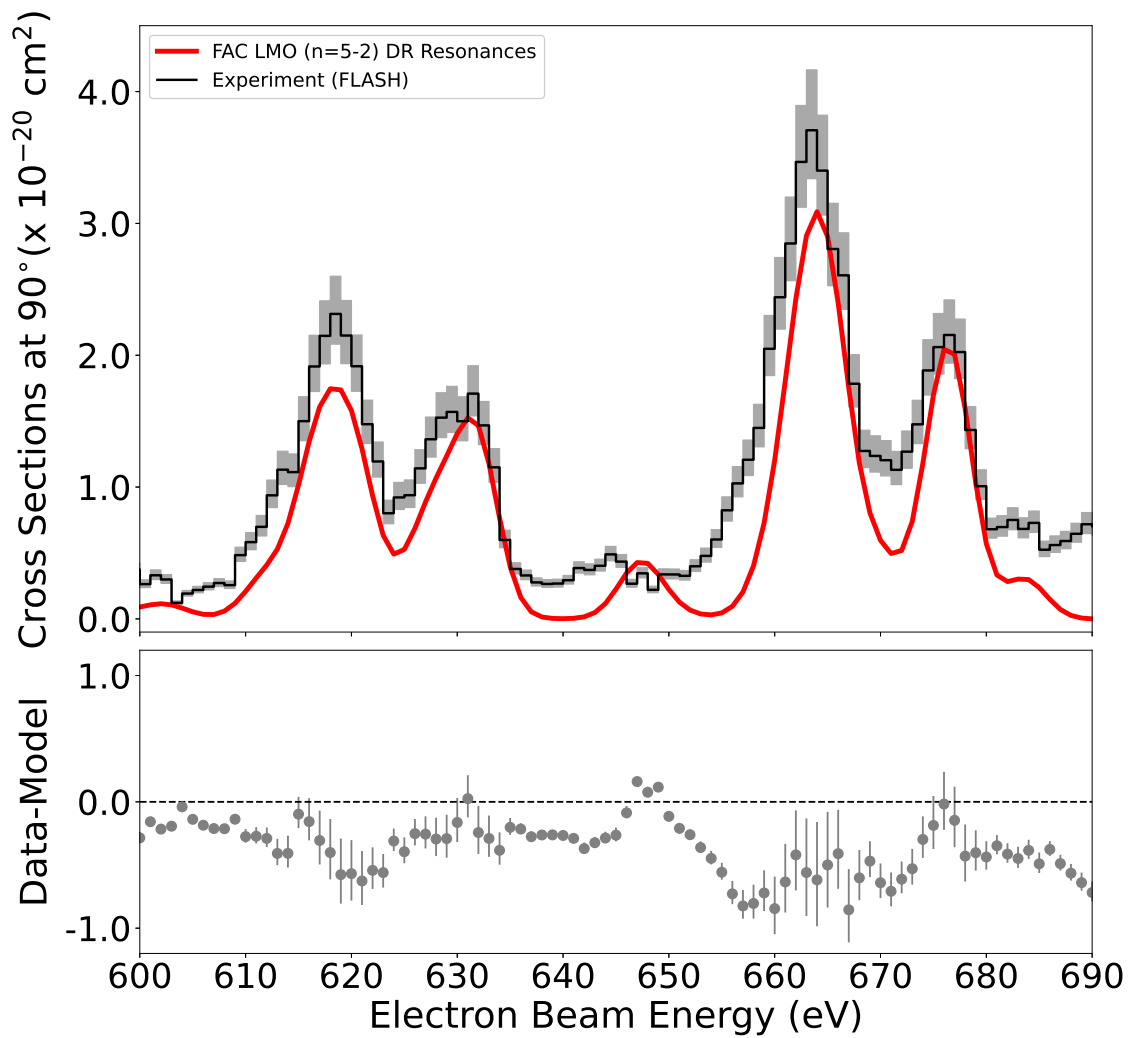


Figure 3.5: Experimental cross sections observed at 90° (black curve) versus FAC-calculated absolute cross sections (red curve) for the Fe XVII *LMO* $n = 5 - 2$ resonances within the 1050 - 1120 eV photon-energy range.

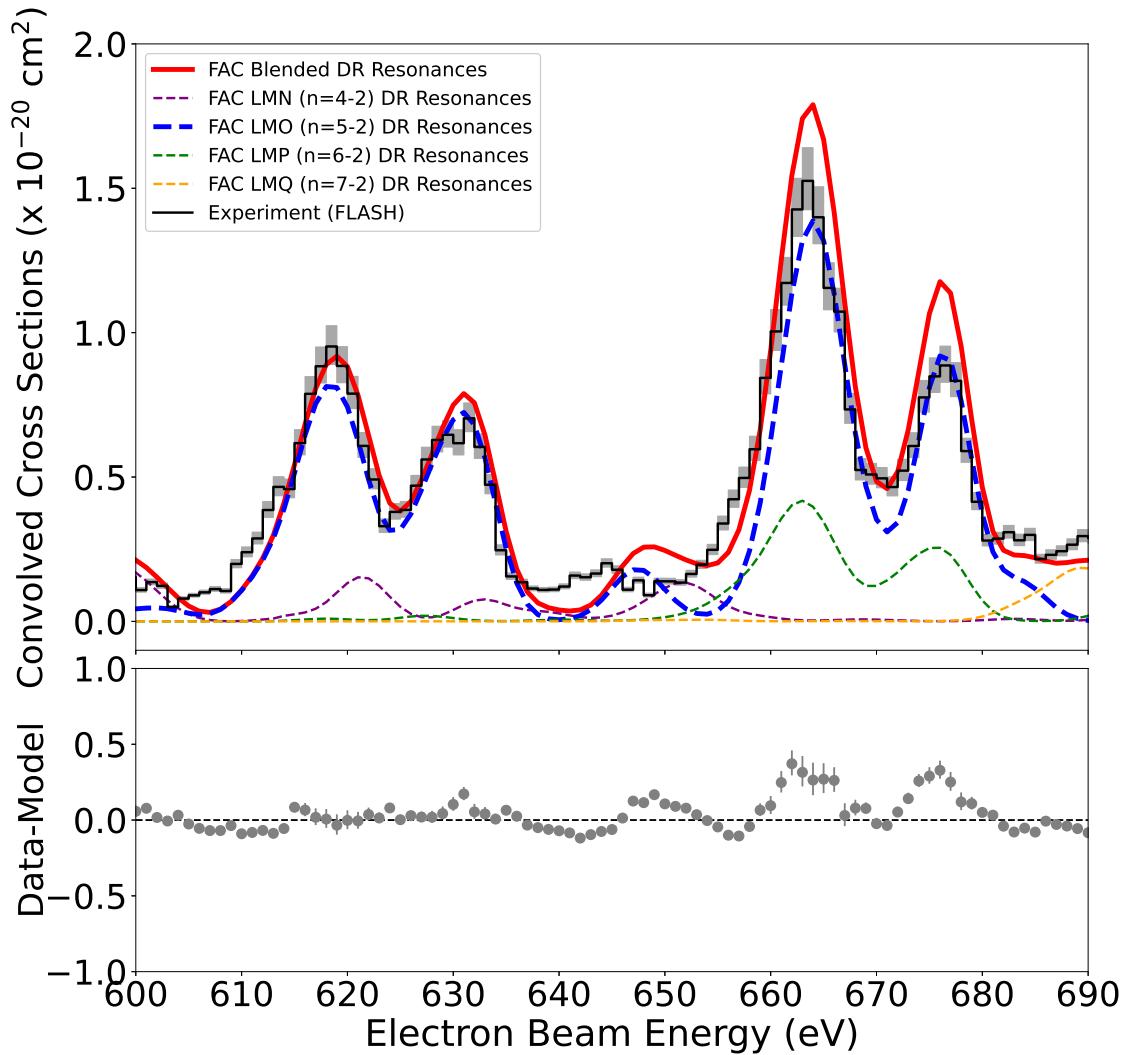


Figure 3.6: Experimental cross sections observed at 90° (black curve) versus doubly convolved theoretical FAC cross sections within the 1050 - 1120 eV photon-energy range, with the red curve representing the sum of all resonances and the dashed curves representing the predicted contributions from each resonance. The blue dashed curve represents the contribution from the *LMO* $n = 5 - 2$ resonances, while the other colored dashed curves show the contributions in this ROI from other DR channels.

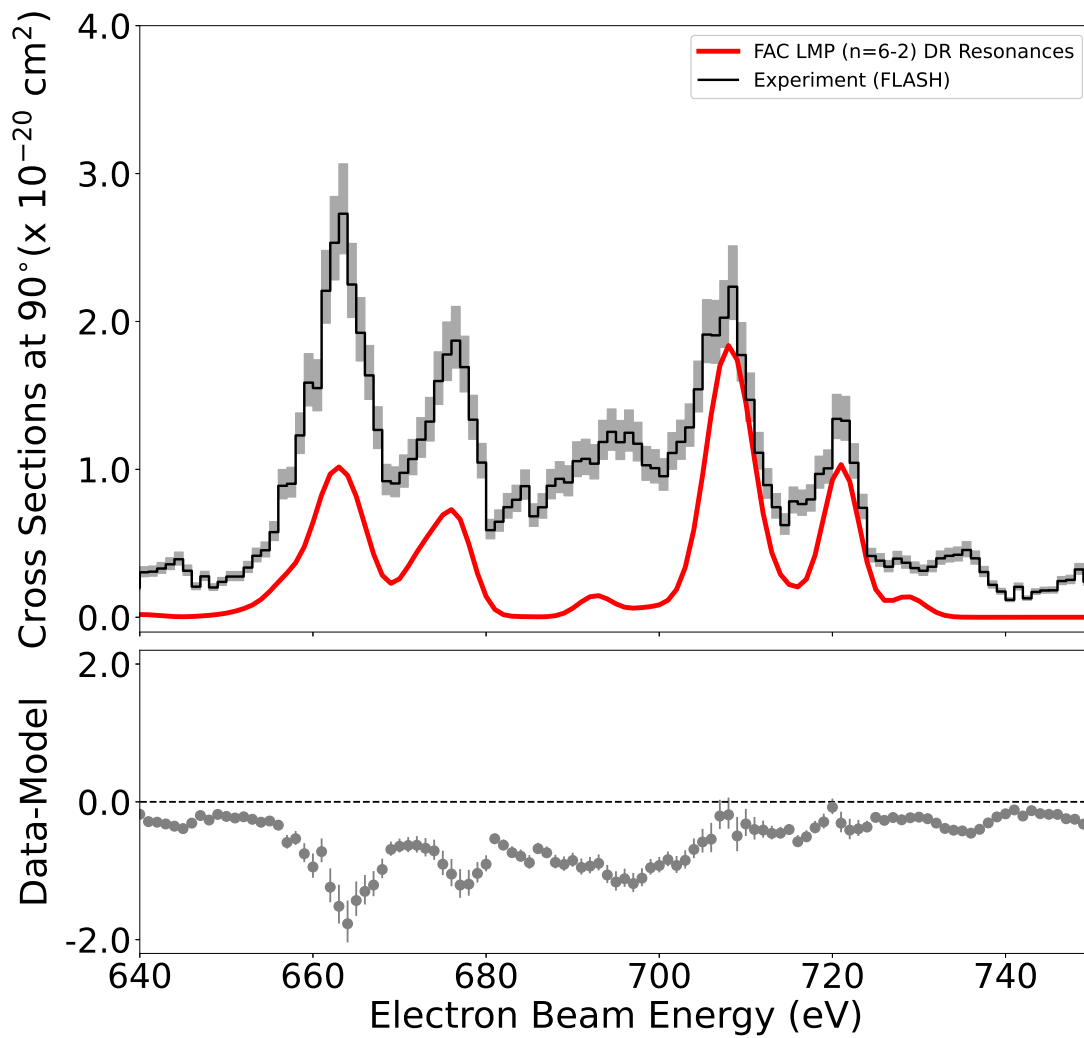


Figure 3.7: Experimental cross sections observed at 90° (black curve) versus FAC-calculated absolute cross sections (red curve) for the Fe XVII *LMP* $n = 6 - 2$ resonances within the 1090 - 1170 eV photon-energy range.

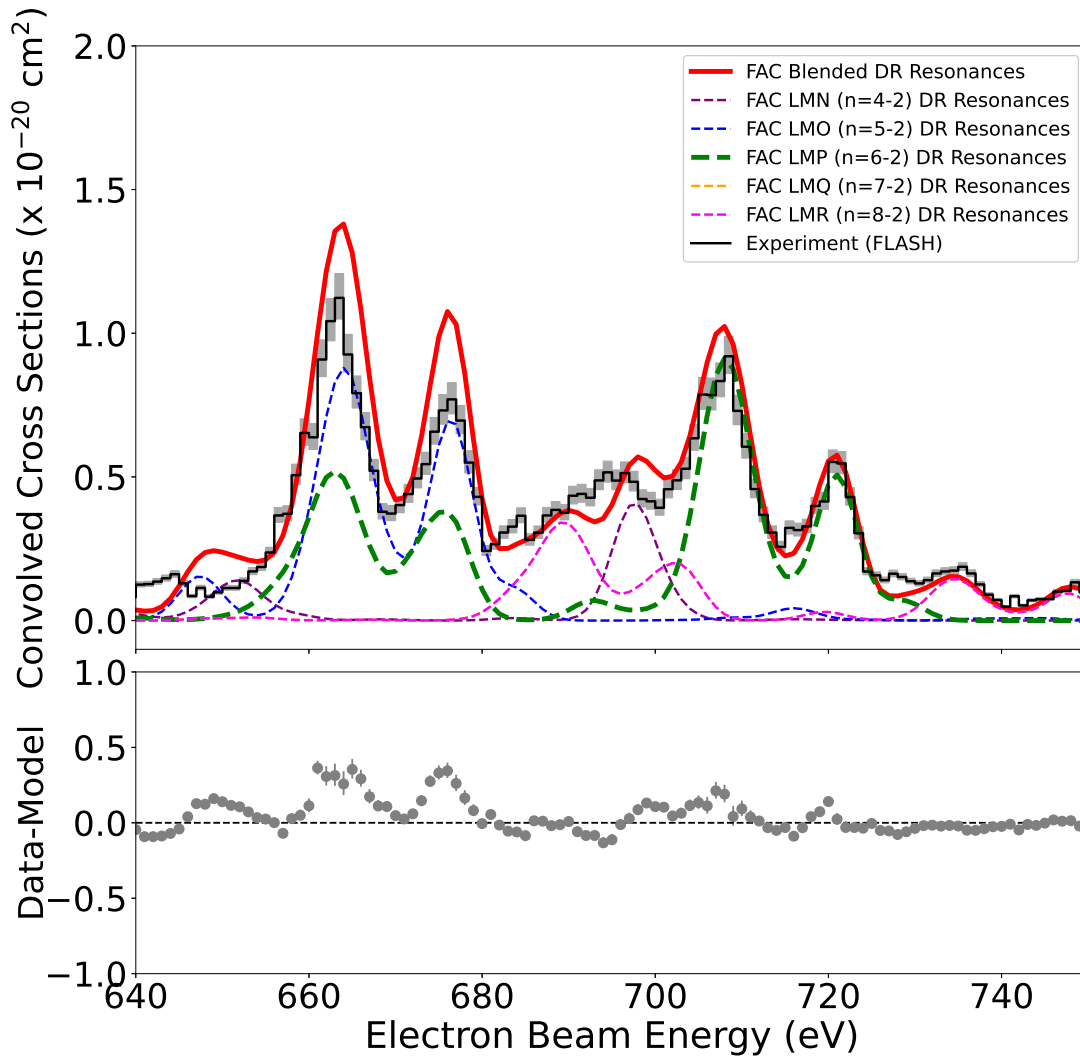


Figure 3.8: Experimental cross sections observed at 90° (black curve) versus doubly convolved theoretical FAC cross sections for the Fe XVII resonances within the 1090 - 1170 eV photon-energy range, with the red curve representing the sum of all resonances and the dashed curves representing the separated contributions from each resonance. The green dashed curve represents the contribution from the *LMP* $n = 6 - 2$ resonances, while the other colored dashed curves show the contributions in this ROI from other DR channels.

3.4.2 Absolute Cross Section Calibration

We selected an ROI along the photon-energy axis ranging from 800 - 860 eV and centered on the $3d$ centroid peak, and chose a single DR resonance at 412 eV electron beam energy to normalize the experimental counts to our theoretical cross sections, as in [Shah et al. \(2019\)](#). We calculated a normalization factor of 1.42×10^{21} counts per cm^2 with a $\sim 2\%$ fitting error. We checked the effect of our ROI selection by shifting the range by ± 15 eV, leading to effects on the normalization factor on the order of $\sim 9\%$. We estimated a total uncertainty of 10% for the $n = 3$ experimental cross sections, the sources of which included: $\sim 2\%$ from counting statistics, $\sim 3\%$ from the carbon-foil transmission correction, $\sim 3\%$ from statistical fitting error, and $\sim 9\%$ from the ROI selection uncertainty. This uncertainty is included in the integrated resonant strength and rate coefficient calculations in [Tables 3.1](#) and [3.2](#) respectively.

For the $n = 4$ cross-section comparison, we selected an ROI along the photon-energy axis ranging from 980 - 1030 eV in order to include every relevant DR and DE contribution in the complex. We applied the same 412 eV peak normalization for obtaining the higher- n DR cross sections, but re-scaled the factor based on the relative fraction of the SDD counts captured in the $n = 4$ ROI given the ROI width relative to the FWHM photon-energy resolution. We assumed the energy resolution to scale with the square root of energy relative to the reference value of 120 eV FWHM at 1000 eV. We estimated a total uncertainty of 13% for the $n = 4$ experimental cross sections considering the same uncertainty sources as we have for $n = 3$, which are of order comparable except statistical uncertainties.

For the $n = 5$ and $n = 6$ cross-section comparisons, we selected photon-energy ROIs of 1050-1120 eV and 1090-1170 eV respectively. Wider ROIs were necessary for these channels in

order to include all DR resonances, so we again applied a correction factor to the normalization of these resonances as a function of the ROI width relative to the FWHM photon-energy resolution of the SDD. We estimated a total uncertainty of 11% for both the $n = 5$ and $n = 6$ experimental cross sections.

Due to the finite energy resolution of the SDD, when selecting a ROI on the experimental data, the resulting spectral histogram loses some flux from the resonances of interest while gaining some flux from features meant to be excluded. This effect becomes more prominent at $n \geq 4$, as the DR resonances closely overlap along the photon-energy axis.

3.4.3 Doubly Convolved Cross Sections

To reproduce the effect of finite detector resolution on the spectrum from a given ROI on the photon-energy axis, we employed a double-convolution approach. In our previous work ([Shah et al., 2019](#); [Grilo et al., 2021](#)), we broadened the theoretical cross sections only on the electron beam energy axis to account for its Gaussian distribution. In the present approach, we also apply Gaussian broadening to the cross sections along the photon-energy axis to match the finite detector resolution. For this, we convolve the theoretical cross sections with the experimental response function. We neglect broadening due to natural linewidth and temperature, and consider only electron beam energy spread and photon-detector resolution, the dominant terms, so that

$$\sigma_i(E_e, E_\gamma) = \sigma_{i,total} G(E_e, E_{e,0}, w_e) G(E_\gamma, E_{\gamma,0}, w_\gamma) \quad (3.3)$$

where σ_i is the cross section of process i ; E_e and E_γ are the electron beam and photon energies, respectively; $\sigma_{i,total}$ is the total cross section for process i ; and $G(E, E_0, w_i)$ are Gaussian

distributions centered on E_0 , with widths w_e , w_γ representing the FWHM of electron-energy spread and photon-detector resolution respectively, and evaluated at E .

By convolving the theoretical cross sections through the detector response before applying the ROI cut, we are able to reproduce better experimentally blended features in the direct comparison of the higher n cross sections. This approach is not as useful when attempting to separate closely spaced line manifolds such as $3d - 2p$ and $3s - 2p$, as they are very sensitive to the exact choice of ROI.

Additionally, we use this approach to separate the contributions from each LMn DR resonance individually to observe the degree of blending within the spectral features in an ROI projection. In doing so, we gain a better understanding of the blends in the data and calculate an approximate contamination fraction for resonances outside of the n complex in question. We apply these corrections to our experimental resonant strength and rate coefficient calculations in Tables 3.1 and 3.2 respectively.

The electron beam energy resolution was set to match the energy spread of the rather monoenergetic electron beam ($w_e = 5$ eV) of FLASH-EBIT. The X-ray photon-energy resolution w_γ was set to ~ 120 eV to match that of the SDD. Figures 3.1 and 3.2 shows two-dimensional contour plots comparing the measured X-ray flux from the FLASH-EBIT experiment as a function of electron-beam energy and photon energy and the now doubly convolved FAC-calculated X-ray intensity respectively.

We determined the normalization factor by computing the amplitudes of the 412-eV peak in the $3d$ manifold for both the experimental and doubly convolved theoretical projections (with the same ROI selections) and taking the quotient. We shifted the $3d$ ROI by ± 15 eV for both the experimental and doubly convolved theoretical cross sections simultaneously before calculating

the effects on the normalization factor. In this way we effectively reduced the systematic error stemming from the ROI selection bias from 9% in our previous study (Shah et al., 2019) down to 3%. Total uncertainties (statistical and systematic) from counting statistics, carbon-foil transmission correction, and normalization factor were estimated at 10%, 7%, and 7% for the $n = 4$, $n = 5$, and $n = 6$ doubly convolved experimental cross sections respectively. These results represent $\sim 3\text{-}4\%$ improvements with respect to earlier absolute cross section uncertainties.

We then plotted one-dimensional histograms of each complex to represent the differential cross sections as a function of electron-beam energy. Figures 3.3 and 3.4 show a comparison between both the experimental $n = 4$ cross sections versus the absolute theoretical and doubly convolved $n = 4$ cross sections respectively. The doubly convolved cross sections agree much better with the experiment and exhibit previously hidden features that blend in due to the energy resolution of the SDD. Figures 3.5 and 3.6 show comparisons of the experimental cross-sections for the $n = 5$ complex versus the absolute and doubly convolved cross sections respectively, with the dashed curves representing the separated contributions from each DR channel. Similarly, Figures 3.7 and 3.8 show the same comparison for the $n = 6$ complex.

3.4.4 Rate Coefficients

We tabulate both the experimental and absolute (i. e., not doubly convolved) integrated resonant strengths in Table 3.1 for each defined electron beam energy region. We integrated each n complex over their respective beam-energy ranges. We estimated contamination fractions from our doubly convolved cross sections to correct for blending in the *LMO* $n = 5 - 2$ and *LMP* $n = 6 - 2$ calculations. We also inferred rate coefficients from both the experimental results and the

FAC-calculated absolute DR total cross sections, as they are convenient parameters for spectral modelling as well as collisional-radiative models of single-temperature and multi-temperature astrophysical plasmas.

As in [Grilo et al. \(2021\)](#), we converted the experimental cross sections observed at 90° (with respect to the electron beam) to total cross sections using the formula $S^{total} = 4\pi I^{90^\circ} / W(90^\circ)$, where I^{90° represents the observed DR intensity and $W(90^\circ) = 3/(3 - P)$ is a polarization correction factor in which P is the calculated polarization for a specific radiative transition ([Beiersdorfer et al., 1996](#)).

The DR rate coefficients were obtained by integrating the corresponding DR resonant strengths over a Maxwellian velocity distribution of the electrons ([Gu, 2003](#)) as shown in Equation 3.4 below

$$\alpha_{if}^{DR} = \frac{m_e}{\sqrt{\pi}\hbar^3} \left(\frac{4R_\infty}{k_B T_e} \right)^{3/2} a_0^3 \sum_d E_{id} S_{idf}^{DR} \exp\left(-\frac{E_{id}}{k_B T_e}\right), \quad (3.4)$$

where R_∞ is the Rydberg constant in eV, a_0 is the Bohr radius, k_B is the Boltzmann constant, and T_e is the electron temperature. We provide the inferred experimental and theoretical rate coefficients in Table 3.2 for each defined electron-beam energy region at different plasma-electron temperatures. For comparison, we include DR rates reported in the OPEN-ADAS online atomic database. The electron temperatures of 110.3 eV and 220.3 eV were used for direct comparison with the tabulated DR rates retrieved from OPEN-ADAS (files: `nrb00#ne_fe16ls24.dat` (nrbLS), `nrb00#ne_fe16ic24.dat` (nrbIC)). These calculations were provided by author N. Badnell in both LS and intermediate couplings (IC).

Table 3.1: Experimental and FAC-calculated integrated cross sections ($10^{-20}\text{cm}^2 \text{ eV}$) with deviations (relative data-model disagreement \pm experimental uncertainty).

Channel	Energy (eV)	S_{FLASH}	FAC	S_{FAC} Deviation
<i>LMM</i> ($3s \rightarrow 2p$)	300-340	86 ± 10	81	(6% \pm 13%)
<i>LMM</i> ($3p \rightarrow 2p$)	340-380	200 ± 30	199	(1% \pm 18%)
<i>LMM</i> ($3d \rightarrow 2p$)	380-420	300 ± 40	264	(14% \pm 15%)
<i>LMN</i> ($3l \rightarrow 2p$)	560-620	430 ± 60	508	(-15% \pm 16%)
<i>LMN</i> ($4l \rightarrow 2p$)	490-610	150 ± 30	138	(9% \pm 25%)
<i>LMO</i> ($3l \rightarrow 2p$)	650-700	370 ± 50	424	(-13% \pm 16%)
<i>LMO</i> ($5l \rightarrow 2p$)	740-810	64 ± 9	59	(8% \pm 16%)
<i>LMP</i> ($3l \rightarrow 2p$)	700-750	320 ± 40	340	(-6% \pm 14%)
<i>LMP</i> ($6l \rightarrow 2p$)	850-890	31 ± 4	32	(-3% \pm 15%)
<i>LNN</i> (total)	740-810	21 ± 3	19	(11% \pm 17%)
<i>LNO</i> (total)	850-890	12 ± 2	4.9	(145% \pm 20%)

3.5 Discussion

For the $n = 4$ absolute cross sections, there are several noticeable discrepancies between the theoretical and experimental data in Figure 3.3. Most prominently, the DR features observed in the experimental data between 600 - 750 eV appear to be missing in the theoretical cross sections. For the LNn cross sections, the observed peak at 797 eV is smaller than predicted. The predicted LNO peaks (blends of $5p$, $5d$, and $5f$) at 859 and 868 eV are both slightly smaller than the measured ones, which contributes to the disparity with the calculated resonant strengths and rate coefficients for this region. The uncertainty for the $n = 4$ channels is also large, as shown by the shaded gray band.

However, in Figure 3.4, we see improved overall agreement between the experimental and doubly convolved theoretical cross sections for the $n = 4$ comparisons over a wide range of electron energies, particularly the lower features observed between 600 - 750 eV. These features, which appear due to the high-energy tail of the LMO $n = 5 - 2$ DR resonances, are now visible and match the experimental data. We also reduce the total (statistical and systematic) uncertainty stemming from counting statistics, carbon-foil transmission correction, and normalization factor calculation by 3% on account of the lower systematic error from the ROI selection. We again emphasize that the normalization for the $n \geq 4$ cross sections is based on a single theoretical value of the DR resonance at 412 eV electron beam energy within the $3d$ manifold.

For the $n = 5$ absolute cross sections in Figure 3.5, there is reasonable agreement for the LMO DR channels at 631 and 677 eV, but discrepancies for the channels at 619 and 664 eV. However, for the doubly convolved theoretical cross sections in Figure 3.6, we see agreement within $\leq 10\%$ for the separated LMO DR channels. We also see better line ratio agreement

between the 664 and 677 eV peaks for the doubly convolved cross sections when compared to the absolute cross sections as a direct result of adjacent *LMP* DR contributions blending into the ROI, thus exhibiting another example of improved agreement of theory with experiment. For both approaches, however, the DR channel observed at 648 eV appears shifted by 1-2 eV.

For the $n = 6$ absolute cross sections, there are significant discrepancies for the *LMP* DR channels at 664 eV and 677 eV, as shown in Figure 3.7, due to blending with the *LMO* resonances. The complex observed at 680 - 700 eV in the experimental data also does not appear in the absolute cross sections. However, when doubly convolved as shown in Figure 3.8, we observe reasonable agreement for the 680 - 700 eV complex, and we see that is primarily a blend of DR resonances from *LMN* $n = 4 - 2$ and *LMR* $n = 8 - 2$. We also see excellent agreement within $\leq 10\%$ for the separated *LMP* $n = 6 - 2$ resonances at 708 and 721 eV.

We reasonably agree within 2σ when comparing most of the experimentally estimated rate coefficients to both our absolute theoretical predictions and data compiled in OPEN-ADAS. Disparities become more noticeable for the higher n complexes, particularly the *LNO* resonances. However, the total integrated cross sections are smaller for these resonances, and therefore less consequential.

Regarding other atomic databases, we do not compare our results to AtomDB, as the rates for the $n \geq 4$ channels are not yet available, nor with SPEX, as the Fe XVII rates available are from FAC calculations done by [Shah et al. \(2019\)](#); [Gu et al. \(2020\)](#) which made nearly identical calculations to ours for up to $n' \leq 60$, making such a comparison pointless.

Determining accurate rate coefficients for these DR satellite lines is therefore crucial for reliable diagnostics of hot astrophysical plasmas. This has been shown e. g., in Refs. ([Gabriel, 1972](#); [Beiersdorfer et al., 2018](#)), where plasma-electron temperatures in range 200 - 600 eV were

obtained from the intensity ratio of the satellite lines over the $3C$ resonance transition.

3.6 Conclusions

In the present work, we compared our dedicated FAC cross-section calculations for the dielectronic recombination satellites of Fe XVII to those extracted from our experiment using FLASH-EBIT. We thereby extended the experimental benchmark to higher electron energies to excite $n \geq 4$ DR resonances of Fe XVII. We improved on previous work by doubly convolving our theoretical cross sections with the experimental values of photon-energy resolution and electron beam energy spread. Moreover, by combining our calculations and experimental data, we inferred DR rate coefficients. This allows us to benchmark those compiled in the OPEN-ADAS database, which were found to agree within 2σ with our improved results.

Performing the same experiment with a high-resolution wide-band X-ray microcalorimeter instead of an SDD would much reduce systematic uncertainties on our DR cross sections. That instrument would enable a far more clear selection of regions of interest in the data, in most cases encompassing individual resonances. Improving DR cross sections for those is a critical task in the perspective of the wealth of observational data expected from X-ray observations with *XRISM*, *ATHENA*, *LEM*, and *Arcus*, as we will not be able to extract the full diagnostic information that their high-resolution would afford without experimentally benchmarked atomic data for collisional excitation cross sections and DR rates.

Table 3.2: FAC-calculated rate coefficients ($10^{-13} \text{ cm}^3 \text{ s}^{-1}$) for different electron temperatures (eV) compared to those reported from OPEN-ADAS.

Channel	T_e	FLASH	FAC		OPEN-ADAS			
			FAC	Deviation	nrbLS	Deviation	nrbIC	Deviation
<i>LMM</i>	110.3	44 ± 6	39	(13% \pm 16%)	43.3	(2% \pm 16%)	41.2	(7% \pm 16%)
(total)	220.3	84 ± 10	75	(12% \pm 14%)	95.2	(-12% \pm 14%)	96.2	(-13% \pm 14%)
	300	83 ± 10	75	(11% \pm 14%)	-	-	-	-
	2000	14 ± 2	13	(8% \pm 17%)	-	-	-	-
<i>LMN</i>	110.3	7 ± 1	7.9	(-11% \pm 17%)	7.27	(-4% \pm 17%)	7.27	(-4% \pm 17%)
(3 <i>l</i> →2 <i>p</i>)	220.3	35 ± 5	41	(-15% \pm 17%)	38.3	(-10% \pm 17%)	39.5	(-13% \pm 17%)
	300	46 ± 6	53	(-13% \pm 15%)	-	-	-	-
	2000	14 ± 2	17	(-18% \pm 17%)	-	-	-	-
<i>LMN</i>	110.3	3 ± 0.5	2.7	(11% \pm 20%)	-	-	-	-
(4 <i>l</i> →2 <i>p</i>)	220.3	14 ± 2	12	(17% \pm 17%)	-	-	-	-
	300	17 ± 2	15	(13% \pm 13%)	-	-	-	-
	2000	5 ± 1	4.4	(14% \pm 25%)	-	-	-	-
<i>LMO</i>	110.3	3 ± 0.5	3.5	(-14% \pm 20%)	2.94	(2% \pm 20%)	2.98	(1% \pm 20%)
(3 <i>l</i> →2 <i>p</i>)	220.3	24 ± 3	27	(-11% \pm 14%)	22.9	(5% \pm 14%)	23.7	(1% \pm 14%)
	300	34 ± 4	38	(-11% \pm 13%)	-	-	-	-
	2000	13 ± 2	15	(-13% \pm 18%)	-	-	-	-
<i>LMO</i>	110.3	0.7 ± 0.1	0.6	(17% \pm 17%)	-	-	-	-
(5 <i>l</i> →2 <i>p</i>)	220.3	5 ± 1	4.1	(25% \pm 22%)	-	-	-	-
	300	6 ± 1	5.6	(7% \pm 20%)	-	-	-	-

	2000	2 ± 0.3	2.1	$(-5\% \pm 18\%)$	-	-	-	-
<i>LMP</i>	110.3	1.8 ± 0.2	2.0	$(-10\% \pm 13\%)$	1.52	$(18\% \pm 13\%)$	1.48	$(22\% \pm 13\%)$
($3l \rightarrow 2p$)	220.3	17 ± 2	19	$(-11\% \pm 13\%)$	14.4	$(18\% \pm 13\%)$	14.4	$(18\% \pm 13\%)$
	300	26 ± 4	28	$(-6\% \pm 18\%)$	-	-	-	-
	2000	12 ± 2	13	$(-7\% \pm 20\%)$	-	-	-	-
<i>LMP</i>	110.3	0.2 ± 0.03	0.2	$(0\% \pm 18\%)$	-	-	-	-
($6l \rightarrow 2p$)	220.3	2 ± 0.2	1.9	$(5\% \pm 11\%)$	-	-	-	-
	300	3 ± 0.3	2.8	$(7\% \pm 11\%)$	-	-	-	-
	2000	1 ± 0.2	1.2	$(-17\% \pm 25\%)$	-	-	-	-
<i>LNN</i>	110.3	0.1 ± 0.02	0.07	$(43\% \pm 25\%)$	0.089	$(12\% \pm 25\%)$	0.079	$(27\% \pm 25\%)$
(total)	220.3	1 ± 0.2	0.9	$(11\% \pm 25\%)$	1.25	$(-20\% \pm 25\%)$	1.10	$(-10\% \pm 25\%)$
	300	2 ± 0.3	1.4	$(43\% \pm 18\%)$	-	-	-	-
	2000	1 ± 0.2	0.8	$(25\% \pm 25\%)$	-	-	-	-
<i>LNO</i>	110.3	0.02 ± 0.003	0.01	$(100\% \pm 18\%)$	0.011	$(82\% \pm 18\%)$	0.009	$(122\% \pm 18\%)$
(total)	220.3	0.4 ± 0.1	0.2	$(100\% \pm 14\%)$	0.209	$(91\% \pm 14\%)$	0.201	$(99\% \pm 14\%)$
	300	0.7 ± 0.1	0.3	$(133\% \pm 17\%)$	-	-	-	-
	2000	0.5 ± 0.07	0.2	$(150\% \pm 16\%)$	-	-	-	-

3.7 Acknowledgments

Research was funded by Max Planck Society (MPS), Germany. We acknowledge support from NASA's Astrophysics Program. G.G. acknowledges support under NASA award No. 80GSFC21M0002. P. A. acknowledges the support from Fundação para a Ciência e a Tecnologia (FCT), Portugal, under Grant No. UID/FIS/04559/2020(LIBPhys) and High Performance

Computing Chair - a R&D infrastructure based at the University of Évora (PI: M. Avillez). C.S. acknowledges support from NASA under award number 80GSFC21M0002 and by Max Planck Society (MPS), Germany.

Chapter 4: Investigating Resonant Auger Destruction of Fe XVII $3s - 2p$ Lines in O Stars

4.1 Introduction

Radiation from massive hot stars has a significant influence on their surrounding environment and the interstellar medium through their winds and radiation fields. These stellar winds also have a strong effect on the evolution of the star itself, as the fractional losses of the star's initial mass through its winds have significant consequences on the stellar chemical profile and surface abundances. O- and B-type stars are known to produce stellar winds with mass-loss rates as high as $10^{-5} M_{\odot} \text{yr}^{-1}$ (Morton, 1967; Puls et al., 2006), which are driven by radiation pressure from scattering in UV transitions as a result of their high luminosity in the $10^5 - 10^6 L_{\odot}$ range (Castor et al., 1975). The winds are further multiplied by the effect of line-deshadowing instabilities (Sundqvist et al., 2018), which result from the displacement of optically thick driving transitions from their shadow in frequency space due to their Doppler shift in the wind.

The mass-loss rate is a key parameter for studies of the physical conditions of stellar winds as well as the evolutionary and ISM feedback effects in massive stars. Different diagnostics across the electromagnetic spectrum, such as $H\alpha$ optical line emission and absorption, free-free radio continuum emission (Puls et al., 2006), and UV resonance line absorption (Fullerton et al.,

2006), are useful as they sample different parts of the wind. However, these diagnostics typically suffer from systematic uncertainties related to small-scale density inhomogeneities or "clumping" in the wind, which limits spectral interpretation.

Hydrodynamic simulations show that the line-deshadowing instabilities lead to the wind clumping as well as embedded wind shocks (EWS), which have been confirmed as the source of soft X-ray emission in OB stars (Feldmeier et al., 1997; Cassinelli et al., 2001; Kahn et al., 2001b; Kramer et al., 2003). The X-ray emission lines and their optical thickness have valuable utility as an alternative diagnostic for wind mass-loss rate measurements, as X-ray line profiles are insensitive to density inhomogeneities. The degree of the wind absorption, which is characterized by the optical depth of the wind to X-rays, can be also used as a diagnostic of the wind mass-loss rate as well as the distribution of the shock-heated plasma, particularly in terms of its effect on X-ray line profile shapes (Owocki & Cohen, 2001; Leutenegger et al., 2010).

The X-ray spectra of OB stars are mainly thermal in nature, as they are dominated by discrete lines from metals with ionization stages skewed toward lower temperatures (Guedel & Naze, 2009). The spectral lines are particularly dominated by the L-shell $3d - 2p$ and $3s - 2p$ transitions of Fe XVII (Fe^{16+}) ions in the $15 - 17 \text{ \AA}$ range (Parkinson, 1973; Canizares et al., 2000; Mauche et al., 2001; Doron & Behar, 2002; Xu et al., 2002; Paerels & Kahn, 2003). The $3s - 2p$ transitions known as the $3F$, $3G$, and $M2$ lines are produced by decay from $[2p_{1/2}2p_{3/2}^43s_{1/2}]_{J=1} \ ^3P_1$, $[2p_{1/2}^22p_{3/2}^33s_{1/2}]_{J=1} \ ^1P_1$, and $[2p_{1/2}^22p_{3/2}^33s_{1/2}]_{J=2} \ ^3P_2$ to the $[2p^6]_{J=0} \ ^1S_0$ ground state, and are observed at 16.776 \AA , 17.052 \AA , and 17.096 \AA respectively (Brown et al., 1998; Shah et al., 2024). These lines provide potentially valuable diagnostics of the physical conditions in hot astrophysical plasmas, including electron temperature, electron density, and velocity turbulence (Behar et al., 2001a; Mewe et al., 2001; Kallman et al.,

2014; Beiersdorfer et al., 2018). However, significant disparities between the astrophysical observations, laboratory experiments, and theoretical calculations of the intensity ratios for these lines have limited their diagnostic use (Beiersdorfer et al., 2002; Xu et al., 2002; Beiersdorfer et al., 2004; Brown et al., 2006; Gillaspy et al., 2011; de Plaa et al., 2012; Ogorzalek et al., 2017; Shah et al., 2019).

As a result of its high atomic number, lower charge states of iron are also prevalent in high temperature plasmas (Behar et al., 2001b). These are predominantly Fe M-shell ions, for which the L-shell is fully occupied and the valence transitions become inner-shell transitions in Fe I–XVI (neutral Fe⁰⁺ - sodium-like Fe¹⁵⁺) ions. Strong $3d - 2p$ absorption lines produced by Fe M-shell transitions were observed by the *XMM-Newton* RGS in the form of unresolved transition arrays (UTA) in the quasar outflow IRAS 13349+2438 (Sako et al., 2001; Holczer et al., 2007) as well as the Seyfert 1 galaxy NGC 3783 (Blustin et al., 2002). The $3d - 2p$ transition energies of the lower Fe charge states (Fe IV–VI) are so strongly shifted by the considerable presence of $n = 3$ spectator electrons that they appear in the range of $17.0 - 17.2 \text{ \AA}$, which is within the same range as the $3s - 2p$ transition energies of Fe XVII. The UTA is a potentially useful diagnostic for conditions such as ionization structure, column density, and outflow kinematics for the X-ray absorbing material. However, due to the high systematic uncertainties of model-calculated wavelengths for these ions (Gu et al., 2006), current theoretical models must be benchmarked by high-precision experimental measurements of these ion charge states and their transition energies.

Improving both theoretical models and experimental measurements of both Fe-L and Fe-M lines are vital for further interpreting spectral observations of X-ray emitting sources such as OB stars. An anomalous ratio observed in the Fe XVII $3s - 2p$ lines of the O4 supergiant star ζ Puppis remains unexplained (Leutenegger et al., 2012; Hervé et al., 2013). The ratio $(3G + M2) / 3F$ is

typically found to be approximately 2.4 for all O stars as well as a range of other astrophysical sources, but it was found to be only ~ 1.4 for ζ Pup. Grell et al. (2021) conjectured that the strong UV field of ζ Pup produces the observed ratio by de-population of metastable $3s$ excited states, and attempted to use the $3F / (3F + 3G + M2)$ fraction as an independent diagnostic of plasma formation radius because the $M2 + 3G$ blend is typically unresolved in hot star spectra. However, it was found that UV photoexcitation has only a weak effect on the line ratios of Fe XVII in O stars and it cannot explain the observed strength of the $3F$ fraction in ζ Pup. The possibility of resonant Auger destruction (RAD) (Ross et al., 1996; Liedahl, 2005) of the $3G$ and / or $M2$ lines by photoionizing $3d - 2p$ transitions in Fe IV–VI charge states dominant in the bulk of the wind was discussed because of the proximity of their transition energies to the Fe XVII transition energies. However, the lower iron charge state transition energies were not sufficiently well known to evaluate the degree of coincidence with $3G$ and $M2$, as theoretical calculations do not reach the sufficient accuracy of $\Delta E/E \leq 10^{-5}$ (Gu et al., 2006; Blancard et al., 2018) and few experiments have been performed on the lower charge state transitions. Understanding whether the effect of RAD is relevant for the ζ Pup line ratio anomaly requires precise knowledge of the relevant transition energies due to the dependence on wavelength coincidence.

Electron beam ion trap (EBIT) measurements at the high spectral resolution P04 beamline at the German Electron Synchrotron (DESY) determined that the $3d - 2p$ transitions of the lower scandium-like iron charge state Fe VI (Fe^{5+}) are nearly coincident in transition energy with the Fe XVII $3G$ line (C.Shah, *private communication*), thus enabling the possibility of RAD of Fe XVII $3G$ photons. The possibility of Auger decay arises when a photon emitted by an ion could be absorbed in a neighboring cooler part of the stellar wind by near-coincident inner-shell transitions of lower charge state ions. The inner-shell excited ion then undergoes Auger decay, in

which the energy is transferred to an outer electron that is subsequently ejected from the atom by autoionization. As a result, the emitted photon is effectively "destroyed". The two-step process is given by

$$X^{q+} + \gamma \rightarrow X^{(q+)**} \quad (4.1)$$

$$X^{(q+)**} \rightarrow X^{(q+1)+} + e^{-} \text{ (Auger decay)} \quad (4.2)$$

where X represents the ion, q represents the charge state, γ represents the absorbed photon, e^{-} represents the emitted electron, and $X^{(q+)*}$ and $X^{(q+)**}$ represents the singly and doubly excited states of the ion respectively. Resonant Auger destruction has been predicted to have a considerable weakening effect on $K\alpha$ lines from intermediate iron ionization stages Fe XVII–XXII, making these lines difficult to detect in the highly ionized accretion disks of Galactic black hole candidates (Ross et al., 1996).

In this work, we conjecture that the anomalous Fe XVII ratio in ζ Pup is caused by the process of resonant Auger destruction as a result of the near-coincidence in transition energy between Fe VI $3d - 2p$ photoionization transitions and the Fe XVII $3G$ line. ζ Pup and other massive hot stars feature supersonic winds with temperatures in the few kK range, with instabilities producing a large number of shocks distributed throughout the wind with temperatures in the 1 - 10 MK range. Under these conditions, it is feasible that the $3G$ photons emitted by Fe XVII ions in the X-ray emitting plasma of ζ Pup are being absorbed in a neighboring cooler parcel by $3d - 2p$ transitions of Fe VI, with the inner-shell excited ion subsequently undergoing Auger decay and emitting an electron. This results in a net destruction

of Fe XVII 3G photons and thus is a potential explanation of the lower line intensity ratio found in ζ Pup.

We derive the predicted optical depth of the absorbing Fe VI lines and we incorporate the calculation into a line profile model for O-star X-ray spectra accounting for the potential effect of RAD. § 4.2 of this paper briefly describes the EBIT experiment and key parameters measured. § 4.3 describes the line optical depth derivation for Fe VI. § 4.4 describes the line profile model, which incorporates the effect of RAD on the Fe XVII emission lines, and shows the model results and calculations. In § 4.5 we discuss our results and future work.

4.2 Experiment

PolarX-EBIT (Micke et al., 2018) was used at the P04 beamline (Viefhaus et al., 2013) of the PETRA III synchrotron-radiation facility to produce and trap the lower Fe M-shell charge states. A molecular beam of iron pentacarbonyl was injected into the trap through a differentially-pumped injection system and subsequently ionized to the Fe M-shell charge states by successive electron impact using a mono-energetic and unidirectional electron beam. The resulting ions were radially trapped by the negative space charge of the electron beam and electrostatically confined in the axial direction by potentials applied to the cylindrical drift tubes. The monochromatic photon beam of the P04 beamline resonantly excited the iron ions produced by PolarX-EBIT. The $n = 2 \rightarrow 3$ inner-shell transitions of Fe IV–VI were measured with state-of-the-art energy resolution by simultaneously recording resonantly excited fluorescence and Auger ionization yields for a given photon beam energy. The P04 beamline is equipped with a high-resolution monochromator, which enabled full resolution of the natural linewidth of transitions. A silicon

drift detector (SDD) mounted on top of the EBIT was used to simultaneously observe the X-ray fluorescence yield following photoexcitation of the ions. The monochromator was calibrated with well-known transitions of hydrogen-like and helium-like oxygen, fluorine, and neon. This calibration technique permitted an accuracy of $\Delta E/E = 10^{-6}$, allowing most of the Fe M-shell UTA features to be resolved.

Using an ion extraction beamline, the abundance of each iron charge state inside the EBIT was observed nearly simultaneously with the observed fluorescence. The signal produced by each ion charge state was measured by a channeltron detector mounted at the end of the extraction beamline. During extraction, the different iron ions are separated according to their charge-to-mass ratio q/m . This allows for a time-of-flight spectrum to be recorded which is used to determine the yield of each ion charge state as a function of photon energy.

From the experiment, both the energy splitting ΔE between the emitter (Fe XVII 3G) and absorber (Fe VI) transitions and the natural linewidth Γ of the Fe VI line were measured as preliminary results for the purposes of this study (C.Shah, *private communication*). Figure 4.1 shows model spectra illustrating the coincidence in the measured transition energies for the Fe XVII 3G transition line and Fe VI line.

4.3 Optical Depth Model Calculations

We calculated the predicted optical depth of the Fe VI line in an O star in order to probe the potential significance of resonant Auger destruction. We derived a function for the absorption line optical depth using radiative transfer and line profile model equations. The optical depth τ is given by

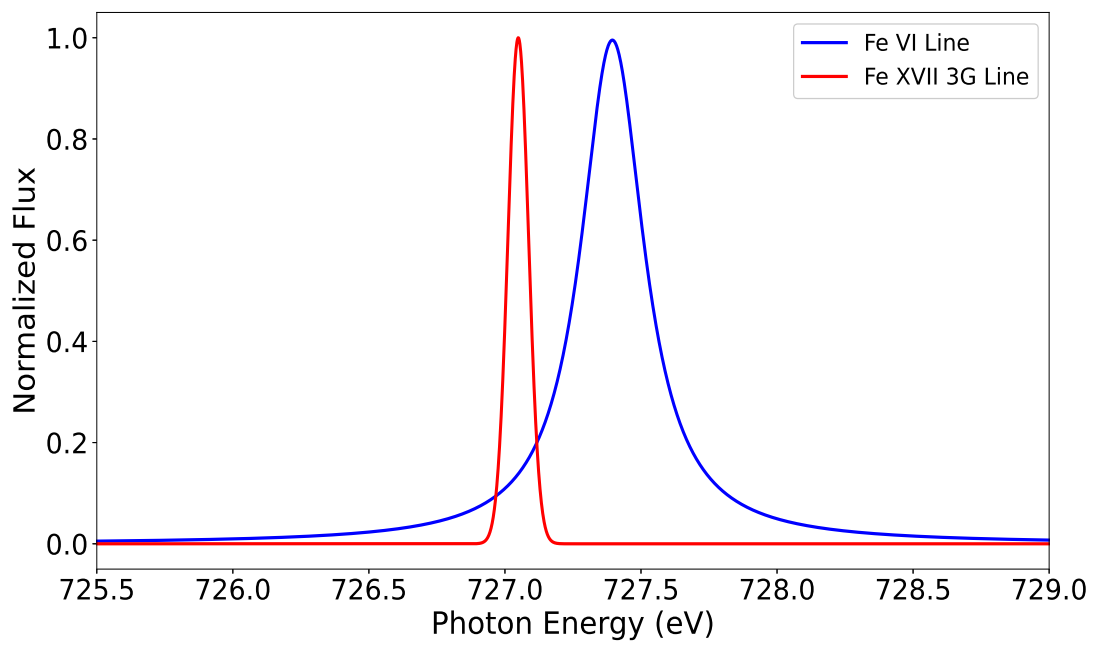


Figure 4.1: Model spectra produced using transition energies and linewidths from the PolarX-EBIT experiment showing the near coincidence of the Fe XVII 3G line (red curve) and Fe VI line (blue curve).

$$\tau = \int_0^z \alpha_\nu dz, \quad (4.3)$$

as the integral of the absorption coefficient α_ν along the line-of-sight coordinate z . Substituting in the equation for the absorption coefficient

$$\alpha_\nu = \frac{h\nu}{4\pi} n_l B_{lu} \phi(\nu) \quad (4.4)$$

and Einstein coefficient B_{lu} for absorption

$$B_{lu} = \frac{4\pi^2 e^2}{h\nu m_e c} f_{lu}, \quad (4.5)$$

we can write the optical depth as

$$\tau = \int_0^z \alpha_\nu dz = \int_0^z n_l \frac{\pi e^2}{m_e c} f_{lu} \phi(\nu) dz \quad (4.6)$$

where $\phi(\nu)$ is the line profile function of the absorbing ion, and f_{lu} represents the oscillator strength of the transition. We further evaluate the optical depth $\tau(p, z)$ to X-rays for a stellar wind along a ray with impact parameter p from point z . Figure 4.2 shows a diagram of the $p - z$ ray coordinate system.

We substituted the radial profile $r \equiv (p^2 + z^2)^{1/2}$ and velocity profile $v(r) = v_\infty (1 - R_*/r)^\beta$, where v_∞ represents terminal wind velocity, R_* represents stellar radius, and β determines the degree of outflow velocity (i.e. $\beta = 0$ implies constant velocity). We also define the ion density $n_l = n_e * A_i$, where n_e represents the electron density (cm^{-3}) and A_i represents the abundance of

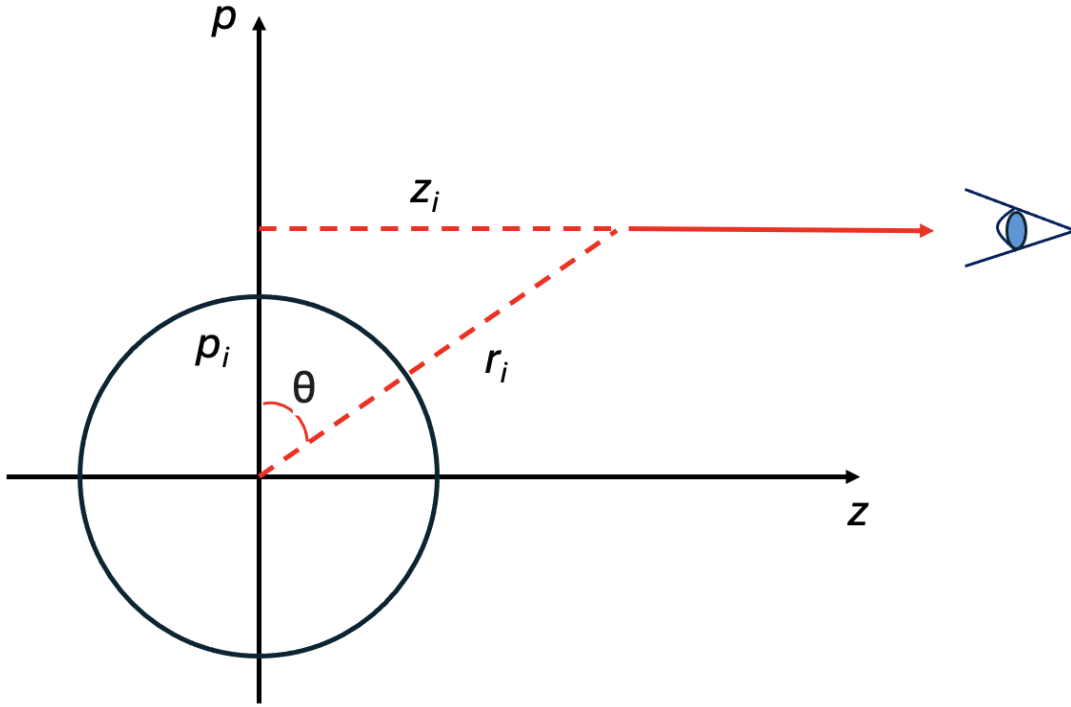


Figure 4.2: Ray coordinate system to evaluate X-ray opacity for a stellar wind along a ray with impact parameter p over distance z .

iron. We further evaluate n_e as

$$n_e = \frac{\rho}{\mu m_p} = \frac{\dot{M}}{4\pi r^2 v \mu m_p} = \frac{\dot{M}}{4\pi R_*^2 v_\infty \mu m_p} \frac{R_*^2 v_\infty}{r^2 v} \quad (4.7)$$

where ρ represents mass density ($g\text{ cm}^{-3}$), μ represents the mean mass per particle, m_p represents proton mass, and \dot{M} represents the stellar mass-loss rate. We also define a characteristic wind number column density N_* (cm^{-2}) as

$$N_* = \frac{\dot{M}}{4\pi R_* v_\infty \mu m_p}. \quad (4.8)$$

Finally, we substitute $u \equiv R_*/r$ as the inverse radial coordinate, and $w \equiv v/v_\infty \equiv (1-u)^\beta$ as the scaled velocity parameter to evaluate the line optical depth as

$$\tau(p, z) = \int n_i \left(\frac{\pi e^2}{m_e c} f_{lu} \right) \phi(\nu) dz = \left(\frac{\pi e^2}{m_e c} f_{lu} \right) (A_i N_*) \int \frac{u^2}{w} \phi(\nu) \frac{dz}{R_*}. \quad (4.9)$$

Approximating the line profile $\phi(\nu)$ as a Lorentzian, therefore neglecting thermal and turbulent Doppler broadening which has a small FWHM compared to Γ , we implemented the following components. The Doppler-shifted frequency of the emitting Fe XVII 3G line is given by

$$\nu_{em} = \nu_{3G} \left(1 - \frac{\Delta v_z}{c} \right) = \frac{E_{3G}}{h} \left(1 - \frac{v_\infty (\Delta w_z)}{c} \right) \quad (4.10)$$

where

$$\Delta v_z = v_{z,abs} - v_{z,em} = v_\infty (\mu_{abs} w_{abs} - \mu_{em} w_{em}) = v_\infty \Delta w_z, \quad (4.11)$$

and $\mu \equiv z/r$ is defined as the direction cosine to the observer. We define the rest frequency of the absorbing Fe VI line as $\nu_{abs} = E_{Fe^{5+}}/h$, and the Lorentzian component HWHM $\Gamma_\nu = \Gamma_{Fe^{5+}}/h$. These components yield the line profile function

$$\phi(\nu) = \frac{1}{\pi} \frac{(\Gamma_\nu/2)}{(\nu_{abs} - \nu_{em})^2 + (\Gamma_\nu/2)^2} = \frac{1}{\pi} \frac{(\Gamma_\nu/2)}{\left(\frac{E_{Fe^{5+}}}{h} - \frac{E_{3G}}{h} \left(1 - \frac{\Delta v_z}{c} \right) \right)^2 + (\Gamma_\nu/2)^2} \quad (4.12)$$

We first conducted a curve-of-growth analysis to estimate the column densities needed for significant absorption by calculating the equivalent width of transmission for the Fe VI lines as a function of column density N_{ion} , in order to predict the total absorption. In Figure 4.3 we plot curves of growth for various turbulent velocities ranging from $v_{turb} = 1 - 2000 \text{ km s}^{-1}$. For the

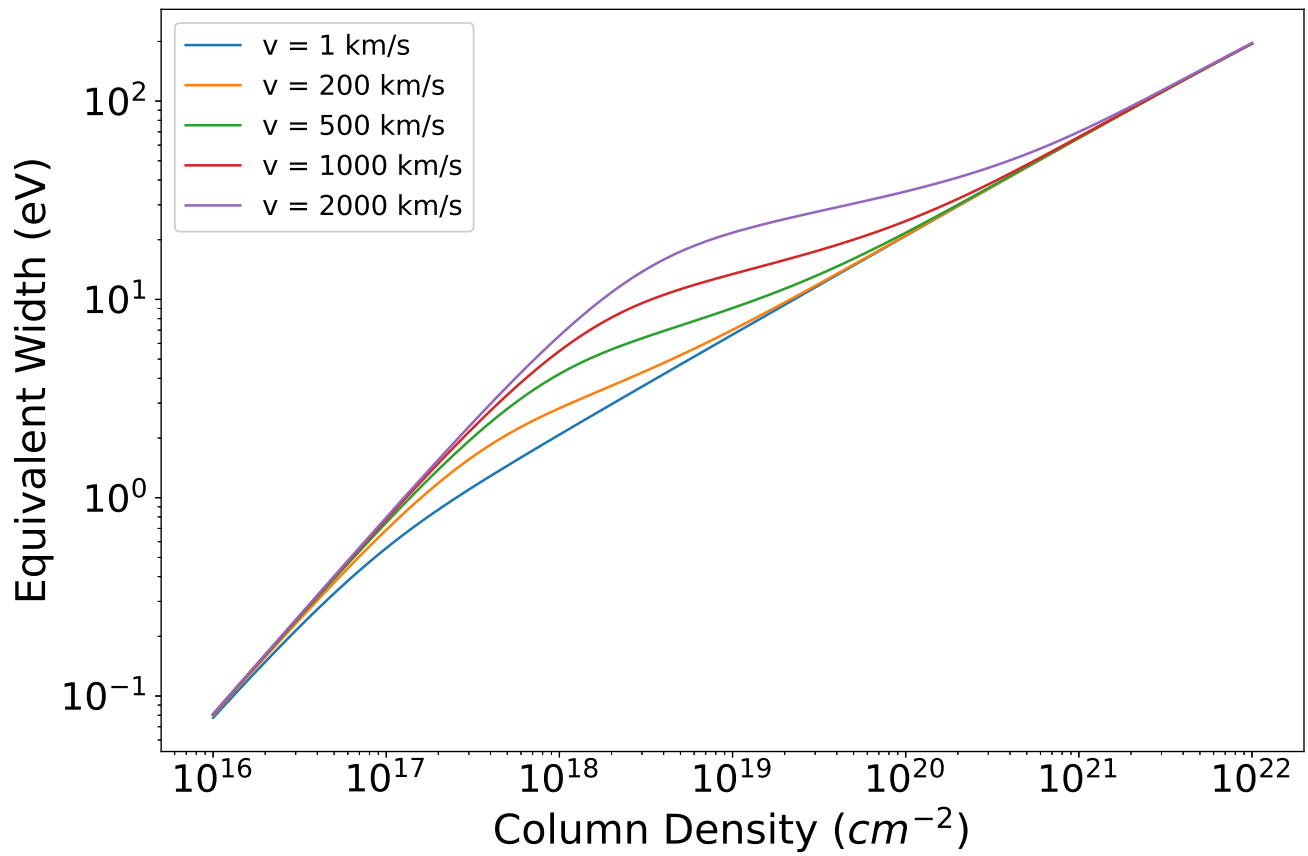


Figure 4.3: Curves of growth for Fe VI ions as a function of column density for selected turbulent velocity values.

higher velocity curves, saturation begins to occur around 10^{17} cm^{-2} .

We then calculated the numerical integral ($z \rightarrow \infty$) of $\tau(p, z)$ at selected p values and measured EBIT values for $E_{Fe^{5+}}$ and $\Gamma_{Fe^{5+}}$. The oscillator strength for the Fe VI $3d - 2p$ transition was obtained from theoretical MBPT calculations done by [Gu et al. \(2006\)](#). Here we assume a terminal wind velocity $v_\infty = 1000 \text{ km s}^{-1}$, characteristic wind number column density $N_* = 7.2 \times 10^{22} \text{ cm}^{-2}$ for ζ Pup ([Leutenegger et al., 2010](#)), mean mass per particle $\mu = 1.2$, and iron abundance $A_i = 3.16 \times 10^{-5}$ ([Asplund et al., 2009](#)). In [Figure 4.4](#), we plotted our calculations as a function of the initial point z_i/R_* . Given that a noticeable amount of optical thickness is visible for $p < 1.5$, the possibility of RAD having an effect on the emitting Fe XVII line is plausible.

4.4 Line Profile Model

[Owocki & Cohen \(2001\)](#) calculated theoretical X-ray line Doppler profiles expected for OB stars when assuming that X-ray-emitting material follows the bulk motion of the wind, and successfully applied these models to derive wind optical depths and mass-loss rates from astrophysical spectra observed by *Chandra* and *XMM-Newton* ([Leutenegger et al., 2006](#); [Cohen et al., 2010](#); [Leutenegger et al., 2013](#); [Cohen et al., 2014](#)). The line emission occurs at a defined wavelength that is Doppler shifted by a stellar wind outflow parameterized by the velocity profile $v(r) = v_\infty(1 - R_*/r)^\beta$ highlighted above. The `windprof` model is a local XSPEC model ([Arnaud, 1996](#)) which implements these physics by calculating the line profiles expected for OB stars by computing the net transmission of X-rays from an emitting plasma distributed throughout a partially optically thick stellar wind.

We implemented the model `radwind` in the context of the `windprof` model to calculate

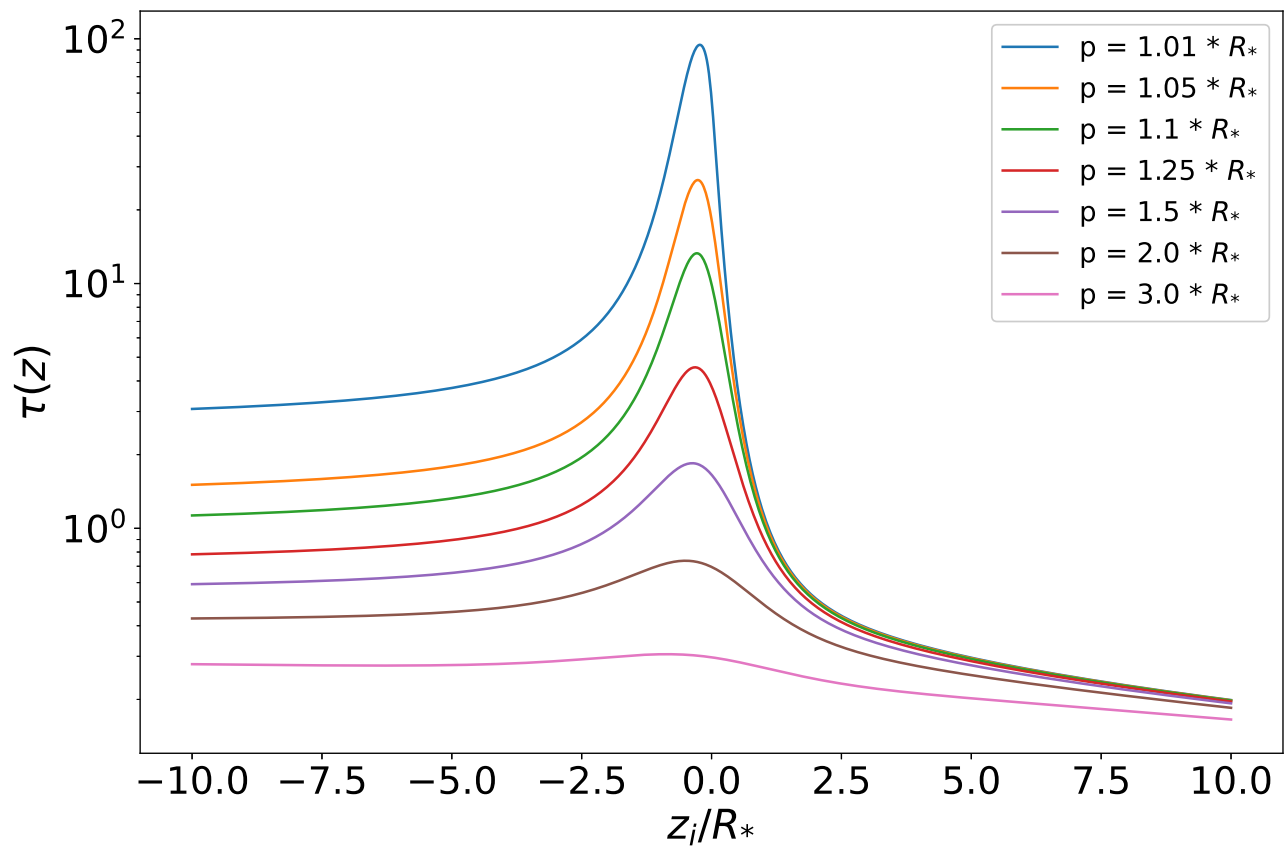


Figure 4.4: Optical depth τ calculation as a function of distance z for selected impact parameter p values. Most of the optical thickness is concentrated behind and close to the surface of the star.

the emission line profiles from O-star winds taking into account the distributed X-ray emission, the absorption by the cool component of the wind, and the transmitted fraction of the emission line strength that is reduced due to resonant Auger destruction by the absorption line. In doing so, we calculate both emission line profiles and line strengths for Fe XVII as a function of a characteristic optical depth τ_0 , the transition energy splitting between the emitter and absorber ΔE , and the linewidth of the absorber Γ . We define τ_0 as

$$\tau_0 = \left(\frac{\pi e^2}{m_e c} f_{lu} A_i N_* \right) \left(\frac{h}{E_{Fe^{5+}}} \right), \quad (4.13)$$

to include all constants, measured values from the experiment, and fiducial values for ζ Pup. We re-iterate that the oscillator strength f_{lu} value for the Fe VI line was obtained from calculations done by [Gu et al. \(2006\)](#). These values yielded a characteristic optical depth of $\tau_0 = 0.025$. The `radwind` model is implemented as an additive XSPEC local model.

RGS spectra of ζ Pup was obtained from the *XMM-Newton* Science Archive and reduced using SAS (Science Analysis System) version 18.0. In [Figure 4.5](#) we fit the archival spectra using `radwind` with the calculated Fe VI line parameters as inputs, in order to examine the degree of reduction in the *3G* line. For comparison, we also fit the spectra with `windprof` models for reference fits without RAD. For the `radwind` models and the solid `windprof` curve, the *3G* / *3F* and *M2* / *3G* line intensity ratios were fixed to yield the (*M2* + *3G*) / *3F* ratio value of 2.4, which is the typical value found in the Fe XVII spectra of other O stars. The dashed curve represents a `windprof` fit in which the line strengths were not linked. As can be seen in the top panel, we see no reduction in the *M2* + *3G* blend for the `radwind` fit with the calculated characteristic optical depth of $\tau_0 = 0.025$. Additionally, even ramping up τ_0 to 0.5 has only a

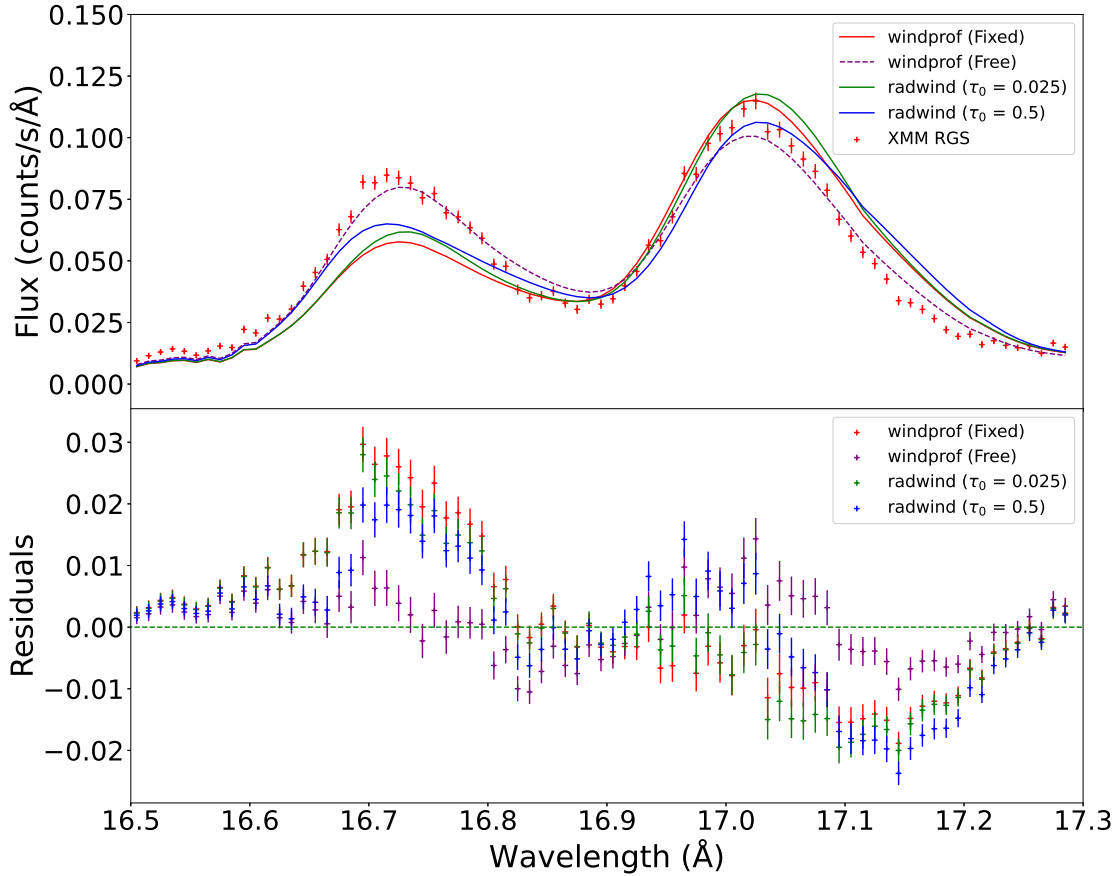


Figure 4.5: ζ Pup spectra of Fe XVII $3s - 2p$ transitions from the *XMM-Newton* RGS fit (red plus signs) using the *radwind* model with Fe VI line parameters, and *windprof* models as references. The green curve represents the calculated *radwind* line profile with a characteristic optical depth $\tau_0 = 0.025$, and the blue curve represents the calculated *radwind* line profile with $\tau_0 = 0.5$. The Fe XVII line strengths were fixed for the *radwind* fits and the solid *windprof* fit (red curve) to yield the common $(M2 + 3G) / 3F$ ratio value of 2.4. The dashed purple curve represents a *windprof* fit in which the line strengths were not linked.

marginal reduction on the $M2 + 3G$ blend line strength.

4.5 Discussion and Future Work

From the `radwind` model fit of ζ Pup, the reduction of the $3G + M2$ blend is marginal even when ramping up the characteristic optical depth. We observe that the $M2 + 3G$ blend also appears shifted to the higher-wavelength side, suggesting that while $3G$ is reduced, $M2$ remaining unaffected prevents significant reduction of the blend. Due to the lack of reduction in the blend, the fixed-ratio model fits must reduce the $3F$ line strength in order to keep the 2.4 value, hence the noticeable model-data disagreement for $3F$.

These results suggest that the Fe VI transition line is not causing a significant amount of resonant Auger destruction that would explain the line ratio anomaly. For RAD to be the cause of the lower line ratio in ζ Pup, the absorption line likely has to be affecting both the Fe XVII $3G$ and $M2$ lines. Though the Fe VI line are nearly coincident with $3G$, it is not close enough to $M2$ to have a considerable effect on its line strength.

We are now considering possible coincidence between the $3s - 2p$ Fe XVII transitions and photoionizing $3d - 2p$ transitions from titanium-like Fe V (or Fe⁴⁺), as these wavelengths are also very close to the wavelengths of the $3G + M2$ blend. We fit the archival spectra using `radwind` with ad hoc Fe V line parameters as inputs, which we estimated from measurements of photoionizing Fe III and IV $3d - 2p$ cross sections by [Schippers et al. \(2021\)](#) and [Beerwerth et al. \(2019\)](#) respectively. In this case, we considered the RAD effect for both the $3G$ and $M2$ lines as the approximated Fe V transition energies fall between the Fe XVII transitions. As shown in the top panel of [Figure 4.6](#), we see a more noticeable reduction in the $3G + M2$ blend

for $\tau_0 = 0.025$ relative to the Fe VI fits. Ramping up the characteristic optical depth τ_0 to 0.1 has a more pronounced reduction on the line strength of the blend. These preliminary results show initial promise, but more comprehensive calculations and / or measurements of the input parameters for Fe V must be completed.

In terms of further future directions, we will investigate possible stellar mechanisms for why RAD may have a significant effect on the Fe XVII ratio in ζ Pup while having a negligible effect for other OB stars. We hypothesize that this can be attributed to ζ Pup having a more optically thick stellar wind than other O stars due to its higher luminosity. The preliminary Fe V results suggest that ramping up the optical thickness of the absorbing lines can considerably reduce the $3G + M2$ blend, indicating that the thickness of the wind is relevant. Another possibility is that the ζ Pup winds have a higher iron ionization balance compared to other O star winds. This will involve conducting an ionization balance simulation of an O star stellar wind. For the RAD effect to definitively explain the ratio in ζ Pup, the ionization balance simulation would have to yield a greater prevalence of Fe IV–VI ions in the wind of ζ Pup than for other stars. The $3d$ metastable level populations for Fe IV–VI must also be considered, as the lower charge states of iron have a numerous amount of $3d$ metastable excited states that are highly populated in O star winds.

Determining the physical conditions that are perturbing the Fe XVII line ratio will have significant implications for studies of the stellar winds of massive stars. The ratio represents a potentially powerful diagnostic of wind optical depth in X-rays, which can be used for independent wind mass-loss rate estimates of massive stars. Measurements from the PolarX-EBIT experiment will also offer important diagnostics for X-ray astrophysics, as accurate inner-shell transition energies are crucial for studies of outflow velocity as a function

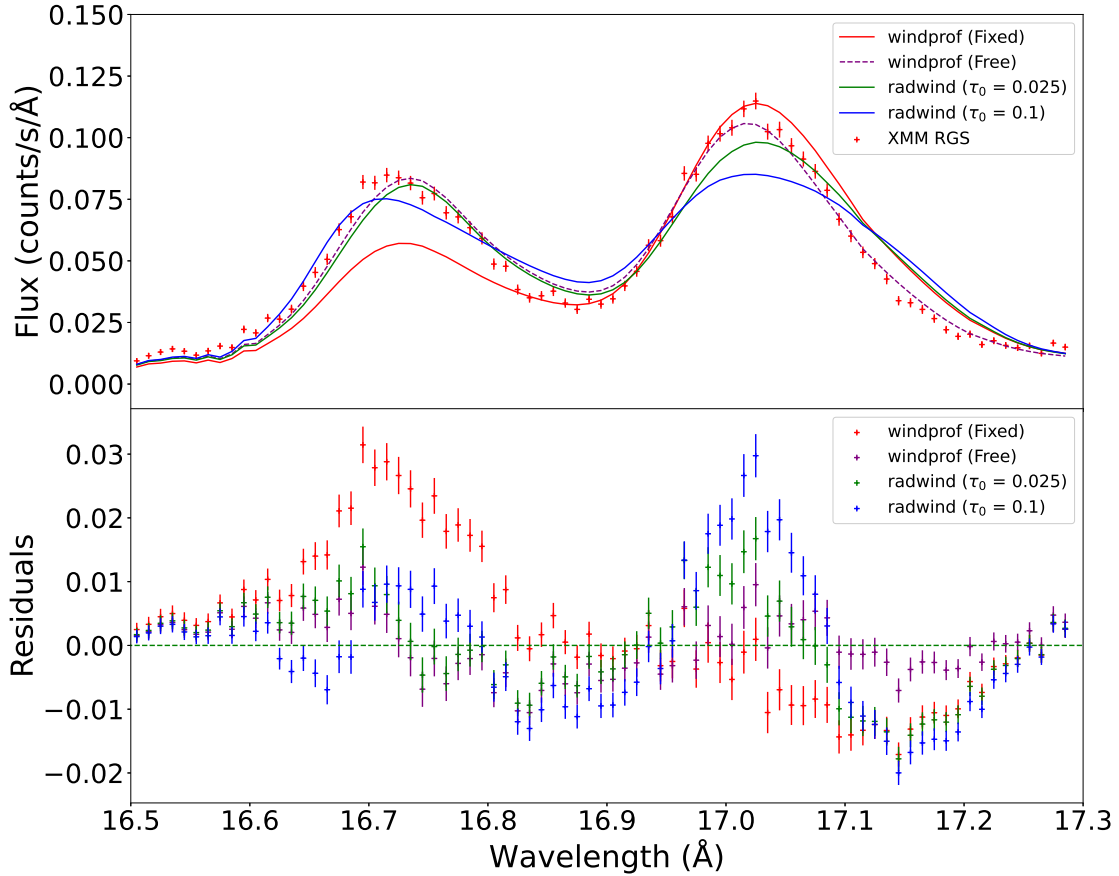


Figure 4.6: ζ Pup spectra of Fe XVII $3s - 2p$ transitions from the *XMM-Newton* RGS fit (red plus signs) using the *radwind* model with estimated Fe V line parameters, and *windprof* models as references. The green curve represents the calculated *radwind* line profile with a characteristic optical depth $\tau_0 = 0.025$, and the blue curve represents the calculated *radwind* line profile with $\tau_0 = 0.1$. The Fe XVII line strengths were fixed for the *radwind* fits and the solid *windprof* fit (red curve) to yield the common $(M2 + 3G) / 3F$ ratio value of 2.4. The dashed purple curve represents a *windprof* fit in which the line strengths were not linked.

of ionization state in outflows from supermassive black holes. Additionally, accurate radiative branching ratios can be derived which are required for calculations of the ionization balance in photoionized plasmas.

4.6 Conclusions

In the present work, we investigated the potential significance of resonant Auger destruction (RAD) resulting from the transition energy coincidence between Fe VI $3d - 2p$ photoionizing transitions and the Fe XVII $3G$ line, in an attempt to explain the anomalous Fe XVII ratio in ζ Pup. We completed model calculations of the optical depth of the Fe VI line using parameters derived from the PolarX-EBIT experiment at DESY. From these predictions, we demonstrated that there is a noticeable amount of optical thickness of the line close to the star, which suggested the possibility of RAD having an effect on the emitting Fe XVII line. We incorporated the predicted optical depth of the Fe VI absorption line into our line profile model `radwind` for O star X-ray spectra that accounts for the potential effect of resonant Auger destruction.

We compared our line profile model calculations to archival observations of ζ Pup taken by the *XMM-Newton* RGS. We fit the archival spectra using `radwind` with the calculated Fe VI line parameters as inputs, in order to examine the degree of reduction in the $3G$ line. We found that the reduction of the $3G + M2$ blend is weak even when ramping up the characteristic optical depth. We therefore conclude that the Fe VI transitions are not causing a significant amount of resonant Auger destruction and it cannot explain the ζ Pup line ratio anomaly. We are now considering the possibility of RAD by Fe V, as ad hoc calculations found that their transition energies fall between the energies of the Fe XVII $3G$ and $M2$ transitions. More comprehensive calculations

for Fe V as well as simulation of the iron ionization balance for O stars must be completed before further interpretation.

Chapter 5: Conclusions

5.1 Future Work

5.1.1 XRISM Spectral Analysis of Messier 82

Messier 82 (M82) is a prototype starburst-driven outflow galaxy that has been the focus of some of the most extensive studies of galaxy evolution across the electromagnetic spectrum (Schaaf et al., 1989; Strickland et al., 1997; Walter et al., 2002; Westmoquette et al., 2007; Zhang et al., 2014). Galactic outflows, which are theorized to result from thermalization of core-collapse supernovae forming pockets of superheated gas that escape the disk (Heckman et al., 1990; Hodges-Kluck et al., 2019), are an important feedback process of galaxy evolution (Lehnert & Heckman, 1996; Veilleux et al., 2005; Liu et al., 2014). The M82 galaxy is located at 3.6 Megaparsecs (Mpc), has powerful winds detected on scales up to 10 kiloparsecs (kpc), and has a disk inclination of 80° , making it a prime observation target for studies of outflows along its minor axis (McKeith et al., 1995). The outflow from the nuclear region of the galaxy extends at least 3 kpc away on both sides from the galactic disk along its minor axis (Figure 5.1 shows a composite image from the *Chandra* ACIS-S). This outflow is assumed to be driven by volume-filling hot plasma, with cold and warm gasses being carried within the flow (Chevalier & Clegg, 1985).

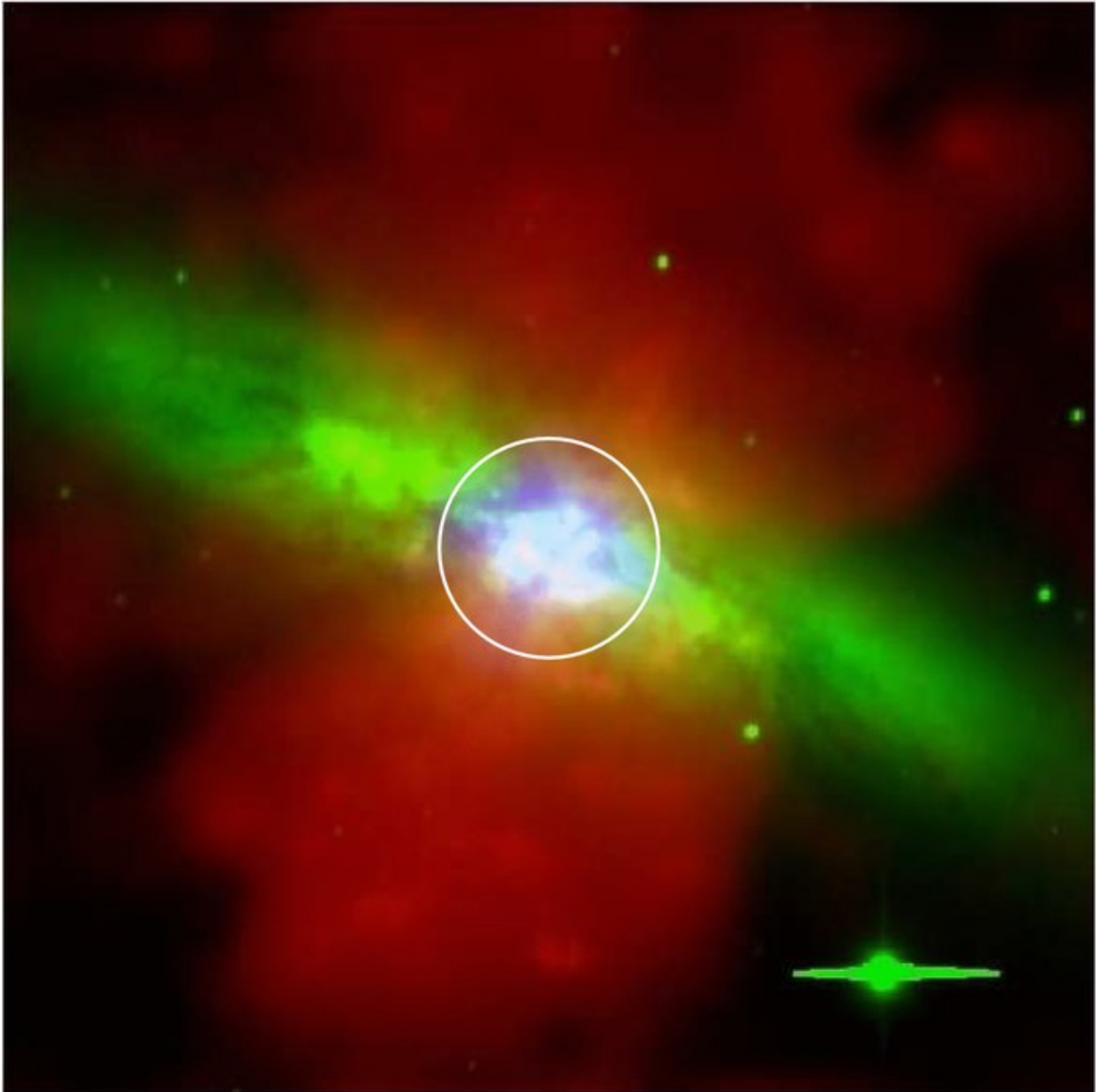


Figure 5.1: *Chandra* ACIS-S composite image of M82 with the white circle representing a region within a 500 parsec radius of the nucleus (scale is 5 kpc on a side). The diffuse hard X-ray emission (3 - 7 keV) energy band is shown in blue, the soft X-ray emission (0.3 - 2.8 keV) energy band is shown in red, and the optical emission is shown in green. Figure adopted from [Strickland & Heckman \(2009\)](#).

Investigations of M82's outflows have included tracing cold gas consisting of neutral hydrogen (H I) and carbon monoxide (CO) (Walter et al., 2002; Salak et al., 2013; Martini et al., 2018), the warm-ionized gas in H α emission (Westmoquette et al., 2007), the X-ray emitting hot gas (Strickland et al., 1997), and the Galactic dust in the UV and infrared wavebands (Marcum et al., 2001; Hoopes et al., 2005; Kaneda et al., 2010). The measured temperature of the hot wind is 9 keV ($\sim 10^8$ K), which corresponds to a wind velocity of ~ 2000 km s $^{-1}$ (Schaaf et al., 1989).

Resolved X-ray spectral observations of M82 from *Chandra* and *XMM-Newton* enabled studies measuring the properties of the hot gas. Ranalli et al. (2008) analyzed *XMM-Newton* observations to observe how the hot plasma properties vary along M82's minor axis, showing that a two-temperature plasma model consisting of a hot component temperature and warm-hot component temperature was necessary. They also found that oxygen, neon, magnesium, and iron had higher abundances within the outflows than in the disk. Lopez et al. (2020) analyzed deep *Chandra* observations of the diffuse X-ray emission from the starburst and outflows, finding that the intrinsic column densities, plasma temperatures, gas densities, and silicon and sulfur abundances all peak in the center of the galaxy. The O, Ne, Mg, and Fe abundances stay relatively constant between the starburst and outflows, indicating transport of the disk metals to the CGM. They also found that charge exchange (CX), a process in which ions capture bound electrons from a neutral atom into an excited state, contributes 8 – 25% of the total broadband flux, making it necessary to include a charge exchange and power-lower component in all regional fits.

The origin of the X-ray emission lines from M82 has many unanswered questions, with little known about the properties of the hot plasma and its interactions with the cool components. The hot wind contains most of the total wind energy and most of the metal abundances (Strickland

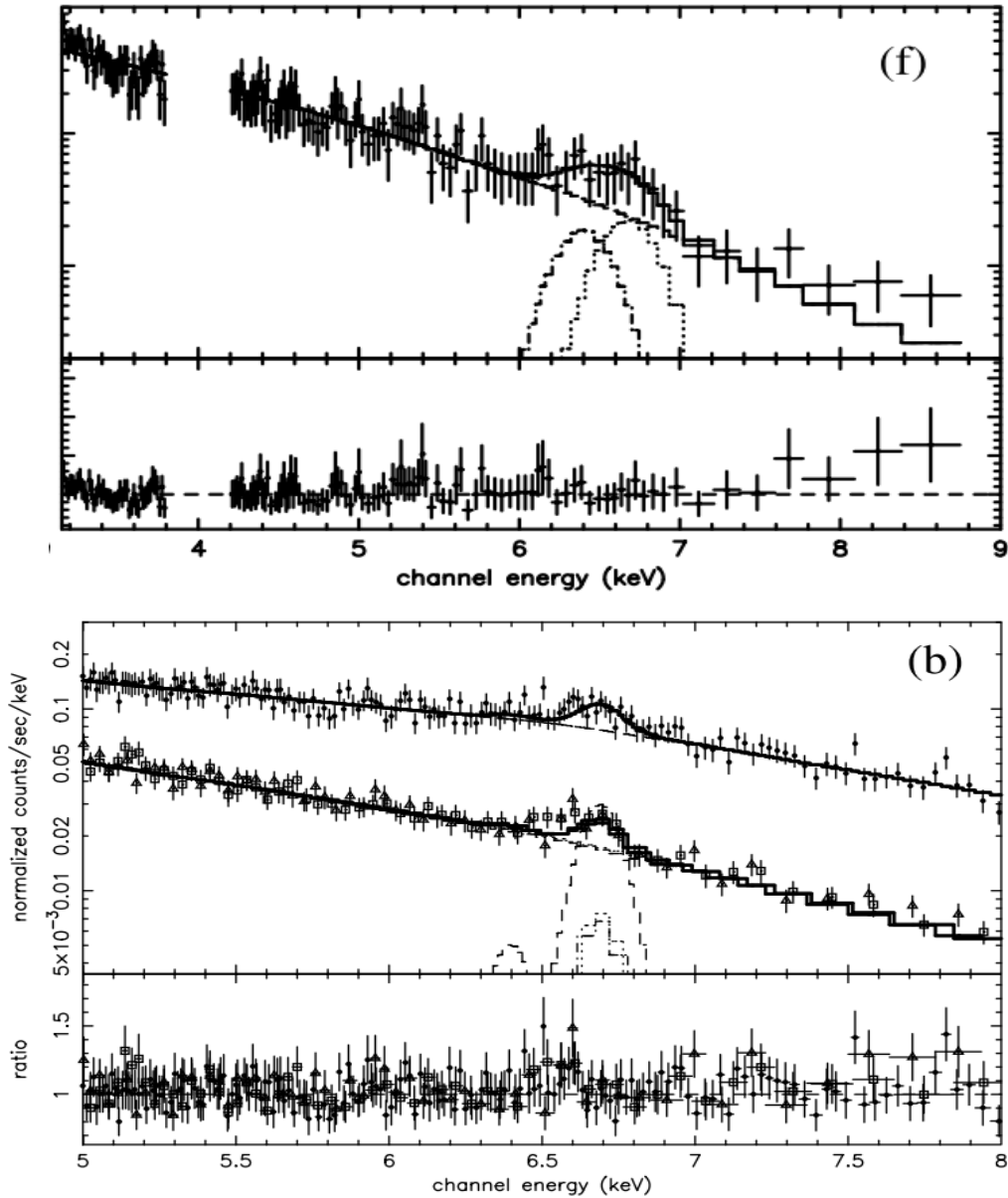


Figure 5.2: (**Top**) *Chandra* ACIS-S and (**Bottom**) *XMM-Newton* EPIC spectral fits of Fe XXV lines in the M82 nuclear region (Figures from [Strickland & Heckman \(2007\)](#)). Analysis found that 20 – 30% of the X-ray emission is diffuse and the continuum was better fit as a power law than with thermal bremsstrahlung models. The modest resolution of the lines limited interpretation of the non-thermal emission and the precision on measurements of the hot wind component velocity.

& Stevens, 2000), but it may not be the mechanism accelerating cool clouds to $v \sim 1000 \text{ km s}^{-1}$ without "shredding" them. Therefore, alternative sources have been theorized, including cosmic rays and radiation pressure (Zhang et al., 2017). There are also questions of whether the soft X-ray emission arises from either the volume-filling hot outflow (Bregman et al., 1995) or mostly from the cool-hot gas interface (Strickland & Stevens, 2000). These contributions must be effectively separated in order to determine the thermal and chemical properties of the hot plasma and therefore the potential role of the outflow in regulating the evolution of the galaxy and its environment (Zhang et al., 2014).

The presence and properties of the diffuse hard X-ray emission in M82 also remains debated. Griffiths et al. (2000) used the first *Chandra* observations of M82 to attribute the diffuse X-rays in the nuclear region to thermal bremsstrahlung from a 10^7 K plasma because of the presence of the Fe XXV $K\alpha$ line complex at 6.7 keV. The 6.7 keV Fe XXV line complex represents an important diagnostic for the driving plasma of galactic-scale outflows, as it is one of the most prominent emission lines in the hard X-ray temperature range. As a result, it represents a valuable diagnostic of the metal enrichment. Strickland & Heckman (2007) analyzed hard X-ray *Chandra* and *XMM-Newton* spectra in the nuclear region (central 500 parsecs) of M82 (see Figure 5.2), and found that the Fe XXV $K\alpha$ line luminosity is consistent with that expected from the enrichment of previous SN ejecta. They found that 20 – 30% of the X-ray emission originates from diffuse gas and the continuum was better fit as a power law than with thermal bremsstrahlung models. This power-law component in the outflows may arise from diffuse non-thermal X-rays, but observations with better resolution of the outflow regions with hard X-ray sensitivity are necessary to verify the nature of the non-thermal emission.

Answering these key unsolved questions requires more accurate measurements of its energy

content, which requires obtaining constraints for the density, temperature, and hot component velocity at the wind's base. Due to its high temperature, low density, and contamination of dense point sources residing in the star-forming region, the hot plasma driving the galactic winds is difficult to observe (Liu et al., 2014). Though superheated gas was detected through the diffuse Fe XXV emission, the energy resolutions of *XMM-Newton* and *Chandra* were too low to directly measure the hot component velocity. The 6.7 keV Fe XXV line width and center must be measured at a $\Delta E \leq 5$ eV FWHM energy resolution in order to sufficiently constrain the hot component velocity to a 25% precision, which will allow for more precise measurements of the total wind energy.

To this end, high-resolution X-ray measurements planned with the *XRISM* Resolve calorimeter array, which achieves a ≤ 5 eV FWHM energy resolution, will further our understanding of these properties. Because of this opportunity, M82 was selected as a priority "Performance Verification" target for the *XRISM* mission. This observation and subsequent analysis will 1) confirm whether hot gas pressure is the primary driver of the galactic wind by measuring the energy contained in the $T \sim 10^8$ K gas, and 2) constrain the mass-loading rate and thermalization efficiency by measuring the velocity of the superheated nuclear gas using the Fe XXV line width. Measuring the velocity to $\sim 30\%$ precision will determine if the velocity is consistent with the ~ 1000 km s⁻¹ value expected from the typical hot wind model, if the kinetic and thermal energy is consistent with the expected scaling from the star-formation rate, and if the energy represented is consistent with the energy of outflowing material > 1 kpc above the nucleus. Doing so will also allow for a constraint on the role of cosmic rays in wind acceleration via comparison to predictions of the velocity profile.

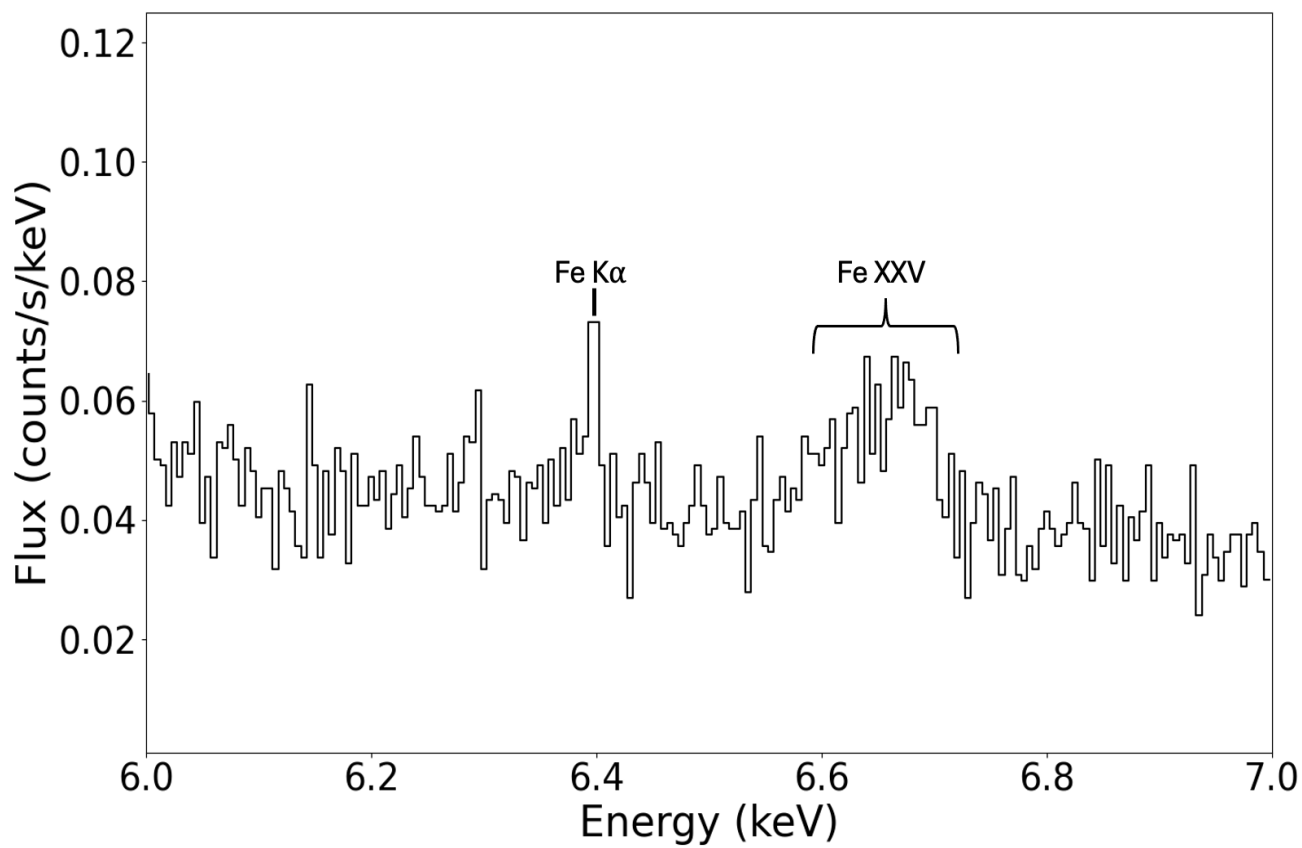


Figure 5.3: **Preliminary** *XRISM* Resolve Fe XXV spectra of M82 nuclear region.

5.1.2 Preliminary M82 XRISM Spectra

XRISM Resolve was pointed towards M82 for 3 days (~ 259 kiloseconds), which for the nominal 45% observing efficiency yielded 115 ks exposure time. Preliminary impressions of the M82 *XRISM* spectra shown in Figure 5.3 indicate that it has sufficient signal-to-noise to determine the line width and center of the Fe XXV $K\alpha$ line complex. The data will therefore allow the measurement of both the initial wind velocity in the nuclear region traced by the Fe XXV lines, and the velocity of the kpc-scale, mass-loaded wind where there are complementary velocities from cooler gas ($< 10^4$ K) traced by O, Ne, Mg, Si, and S lines.

M82 was also observed by the *Swift* X-ray telescope (Burrows et al., 2005) in order to constrain the relative contributions of the X-1 and X-2 X-ray binaries, both of which are variable and inside the Resolve field of view and whose emission is convolved with the diffuse emission in M82. This is necessary due to the nuclear diffuse emission from point sources and the ULX emission being very difficult to spectrally separate (Strickland & Heckman, 2007).

5.1.3 Extension of Previous Works

In terms of potentially extending Chapter 2, Chapter 4 is effectively a follow up of this work, as I hypothesize a new explanation for the ζ Puppis Fe XVII line ratio anomaly with the possibility of resonant Auger destruction. Future laboratory experiments could also potentially use simultaneous EUV and X-ray spectroscopy both to place constraints on the Fe XVII $3s$ cross sections and to benchmark the importance of the $3s$ $J = 0$ level in feeding the upper level of the $3G$ line by measuring the strength of the 1153 \AA line relative to the strengths of the $2p-3s$ lines.

For following up Chapter 3, performing the same experiment with a high-resolution

wide-band X-ray microcalorimeter instead of an SDD would significantly reduce systematic uncertainties on the DR cross sections. The microcalorimeter would enable a far clearer selection of regions of interest in the data by individually resolving the strongest transition lines $3C$ and $3D$ within $3d$ as well as the $3F$ transition line within $3s$. Now when selecting ROIs, I would be able to capture most of the counts associated with each transition and further reduce the uncertainty from the normalization.

Additionally, a miniature EBIT based on the existing HC-EBIT design is currently being assembled at MPI-K for on-site use at NASA GSFC. The planned timescale for the shipment of this EBIT is within the next year. Using the mini-EBIT would enable significantly better beam energy resolution for resolving radiative recombination peaks for the $3s$, $3p$, and $3d$ levels of Na-like Fe XVI, which [Brown et al. \(2006\)](#) used to normalize the $3C$ and $3D$ DE cross sections. Achieving better resolution of these peaks would reduce the uncertainty stemming from the background ions. Using the mini-EBIT would also allow for longer runtimes for experiments, as it does not require supplies of cryogenics such as liquid helium. Longer runtimes would increase the number of spectral counts and subsequently reduce the error stemming from counting statistics.

Improving DR and DE cross sections is a critical task for comprehensive interpretations of spectral data expected from X-ray observations with *XRISM*, *Athena*, *LEM*, and *Arcus*, as we will not be able to extract the full diagnostic information that their high energy resolution will afford without experimentally benchmarked atomic data for DE cross sections and DR rates.

5.2 Summary of Dissertation

The work discussed in this dissertation has contributed to the refinement and advancement of theoretical, laboratory, and observational X-ray studies of iron transition lines. The chapters of this dissertation follow a logical order that reflects the progression of my research over the course of my years in graduate school. By modelling the effects of UV photoexcitation and resonant Auger destruction in O-type star X-ray spectra, and benchmarking FAC atomic data predictions using experimental measurements from an electron beam ion trap, this dissertation has highlighted the primary components of the X-ray astrophysics pipeline and demonstrated the diagnostic utility of iron transition lines.

In Chapter 2, I used the FAC collisional-radiative model to model the effect of UV photoexcitation from O stars on the Fe XVII $2p - 3s$ line ratios. Solving the rate equations as shown in Appendix A.1 allowed for the derivation of an analytical model to calculate the ratios as a function of UV field intensity. Using these models, I demonstrated that the UV field intensities of O stars have only a minor effect on the line ratios. I also implemented a line profile model for Fe XVII in O star spectra for which the profiles are calculated including the radial dependence of the $2p-3s$ ratios, and I compared the model calculations to astrophysical data from coronal and hot stars observed by *Chandra* and *XMM-Newton*. Ultimately, I found that the dynamic range of the model $3F$ fraction as a function of UV field intensity was not large enough to explain the observed difference in this ratio between Capella and ζ Pup. Thus, UV photoexcitation has only a weak effect on the line ratios of Fe XVII in O stars and it cannot explain the observed strength of $3F$ in ζ Pup.

In Chapter 3, I compared FAC-calculated cross-sections for the dielectronic recombination

satellites of Fe XVII to those extracted from the experiment using FLASH-EBIT in order to benchmark the theoretical predictions. I extended the experimental benchmark from previous works to the $n \geq 4$ DR resonances of Fe XVII. I also improved on previous works by employing the approach of doubly convolving the predicted cross sections with both the spread of the electron-beam energy and the photon-energy resolution of the silicon drift detector. I found that the doubly convolved cross sections agree much better with the experiment and exhibit previously hidden features that blend in due to the energy resolution of the SDD. By combining our calculations and experimental data, I inferred DR rate coefficients for comparison to those compiled in the OPEN-ADAS database, which were found to agree within 2σ with our predictions.

In Chapter 4, I probed the significance of the process of resonant Auger destruction as a cause for the anomalous Fe XVII ratio in ζ Pup. EBIT experimental measurements confirmed the near coincidence in transition energy between transitions of the lower iron charge state Fe VI and the Fe XVII 3G line, which allows for the possibility of resonant Auger destruction of Fe XVII 3G photons. I derived the optical depth of the absorbing Fe VI line based on the EBIT measurements, and incorporated the calculation into a new line profile model for O-star X-ray spectra that accounts for the effect of resonant Auger destruction. From the model fit of ζ Pup, the reduction of the 3G + M2 blend, even when ramping up the optical depth, is weak, suggesting that the Fe VI transitions are not causing a significant amount of RAD that would explain the line ratio anomaly. However, possible coincidence between the $2p - 3s$ Fe XVII lines and transitions from titanium-like Fe V is now being considered to once again probe possible RAD. This work is ongoing, and will result in a peer-reviewed journal publication.

In Chapter 5, I highlighted the necessary steps for the analysis of Fe $K\alpha$ spectral lines

from *XRISM* observations of M82. High-resolution X-ray measurements with the *XRISM* Resolve calorimeter achieved the energy resolution necessary to observe the 6.7 keV Fe XXV line width and center with enough precision to sufficiently constrain the hot component velocity. Understanding the hot wind requires accurate measurements of its energy content, which will require obtaining accurate constraints for the temperature and velocity at the wind's base. Spectral analysis is currently ongoing in order to answer these questions.

Appendix A: Chapter 2 Appendix

A.1 Archival Observations

Table A.1: Log of archival observation data. OBSIDs with a * sign denote spectra obtained from the *Chandra* archive, and those with a + sign denote spectra obtained from the *XMM-Newton* Science Archive.

Star	OBSID	Exposure (ks)
Capella	1099*	14.6
Capella	3674*	28.7
Capella	6471*	29.6
ϵ Orionis	3753*	91.7
ϵ Orionis	0112400101 ⁺	12.9
ζ Orionis	610*	59.7
ζ Orionis	13460*	142.9
ζ Orionis	0112530101 ⁺	42.0
ζ Orionis	0657200101 ⁺	97.8
ζ Orionis	0657200201 ⁺	47.4
ζ Orionis	0657200301 ⁺	43.9
EX Hydra	1706*	150.6

τ Scorpii	638*	59.2
τ Scorpii	2305*	13.0
τ Scorpii	0112540101 ⁺	23.2
τ Scorpii	0112540201 ⁺	10.8
λ Cephei	0720090301 ⁺	75.8
λ Cephei	0720090401 ⁺	82.4
λ Cephei	0720090501 ⁺	94.7
λ Cephei	0720090601 ⁺	15.7
ζ Puppis	0095810301 ⁺	52.5
ζ Puppis	0095810401 ⁺	39.9
ζ Puppis	0157160401 ⁺	41.5
ζ Puppis	0095810501 ⁺	38.7
ζ Puppis	0095810901 ⁺	43.5
ζ Puppis	0157161101 ⁺	27.8
ζ Puppis	0159360101 ⁺	66.2
ζ Puppis	0159360301 ⁺	26.9
ζ Puppis	0159360501 ⁺	34.5
ζ Puppis	0159360701 ⁺	23.5
ζ Puppis	0159360901 ⁺	48.3
ζ Puppis	0159361101 ⁺	42.5
ζ Puppis	0159361301 ⁺	61.1
ζ Puppis	0163360201 ⁺	41.6

ζ Puppis	0414400101 ⁺	58.3
ζ Puppis	0561380101 ⁺	64.1
ζ Puppis	0561380201 ⁺	76.6
ζ Puppis	0561380301 ⁺	63.7
ζ Puppis	0561380501 ⁺	60.5
ζ Puppis	0561380601 ⁺	67.5
ζ Puppis	0561380701 ⁺	55.0

A.2 Solution of Rate Equations

In this appendix we solve the rate equations to obtain line ratios for the $3s - 2p$ transitions of Fe XVII as a function of UV field strength and density. The levels are labeled using the level numbers from FAC (as shown in Table 2.1) in ascending energy order, so that the ground state is 0, the four $2p^{-1}3s$ excited states are 1-4 (called $3s$ in this appendix for short), the 10 $2p^{-1}3p$ excited states are 5-14 (called $3p$), the 12 $2p^{-1}3d$ excited states are 15-26 (called $3d$), and the two $2s^{-1}3s$ states are 27 and 28 (called $3s'$; although note that level 28 has only very small oscillator and collision strengths connecting it to levels 1 and 3, so its participation is negligible). First, we give the equation for level 1 (upper level of the M2 line):

$$\begin{aligned} \frac{dN_1}{dt} &= n_e N_0 C_1 - N_1 A_{1,0} + \sum_{i=3p,3s'} (N_i A_{i,1} - N_1 \phi_{1,i}) - \sum_{j=3s,3p,3d,3s'}^{j \neq 1} n_e N_1 C_{1,j} + n_e N_3 C_{3,1} \\ &= R_1 - N_1 A_1 + \sum_{i=3p,3s'} (N_i A_{i,1} - N_1 \phi_{1,i}) - \sum_{j=3s,3p,3d,3s'}^{j \neq 1} n_e N_1 C_{1,j} + n_e N_3 C_{3,1}. \end{aligned} \quad (\text{A.1})$$

Here we use the following notation: n_e is the electron density (cm^{-3}); N_i is the density of ions in level i ; $C_{i,j}$ ($\text{cm}^3 \text{s}^{-1}$) is the collisional rate coefficient from level i to level j ; C_i ($\text{cm}^3 \text{s}^{-1}$) is the collisional rate coefficient from the ground state to excited state i , but using the shorthand that it includes *all* processes populating that level (i.e. cascades, etc.), other than those from the $3s$, $3p$, $3d$, and $3s'$ levels, which are all explicitly accounted for; R_i ($\text{cm}^{-3} \text{s}^{-1}$) is analogous to C_i , but includes the electron and ion ground-state densities, i.e., $R_i \equiv n_e N_0 C_i$; $A_{i,j}$ (s^{-1}) is the spontaneous decay rate from level i to level j , and A_i is the total decay rate from level i summed over all j ; and $\phi_{i,j}$ (s^{-1}) is the photoexcitation rate from level i to level j .

We include electron collisions within $n = 3$ excited states, including excitations from $3s$ states to $3s'$ states (i.e. $2s - 2p$ excitations), but we neglect collisions to $n = 4$ and higher. We also neglect photoexcitation between $3s$ states, since the oscillator strengths are very small. We neglect photoexcitation to $4p$ states, since the energies are much larger.

Thus, from left to right, the terms in Equation A.1 represent all direct collisions, as well as cascades that are not explicitly accounted for; decays to ground; decays from and photoexcitations to $3p$ and $3s'$; collisional excitation to $3s$, $3p$, $3d$, and $3s'$; and collisional de-excitation from level 3.

Similarly, these are the rate equations for the other $3s$ states, levels 2-4:

$$\frac{dN_2}{dt} = R_2 + N_3A_3 - N_2A_2 + \sum_{i=3p,3s'} (N_iA_{i,2}) + n_eN_1C_{1,2} + n_eN_3C_{3,2}; \quad (\text{A.2})$$

$$\frac{dN_3}{dt} = R_3 - N_3A_3 + \sum_{i=3p,3s'} (N_iA_{i,3} - N_3\phi_{3,i}) - \sum_{j=3s,3p,3d,3s'}^{j \neq 3} n_eN_3C_{3,j} + n_eN_1C_{1,3}; \quad (\text{A.3})$$

$$\frac{dN_4}{dt} = R_4 - N_4A_4 + \sum_{i=3p,3s'} (N_iA_{i,4}) + n_eN_1C_{1,4} + n_eN_3C_{3,4}. \quad (\text{A.4})$$

For each $3s$ level, the total A_i is dominated by decay to a single level: for level 3, the branching ratio to level 1 is just $\sim 10^{-4}$, and decay to ground is strictly forbidden, so level 2 is the dominant decay channel (leading to the term N_3A_3 in the equation for level 2); while for levels 1, 2, and 4, the ground state is the dominant decay channel. Photoexcitation and collisional excitation from levels 2 and 4 to the $3p$ manifold are neglected, since these states are

not metastable.

These are the rate equations for the $3p$ states, levels 5-14:

$$\frac{dN_i}{dt} = R_i - N_i A_i + \sum_{j=1,3} N_j (\phi_{j,i} + n_e C_{j,i}) + \sum_{k=3d} N_k A_{k,i}. \quad (\text{A.5})$$

For levels 6, 9, and 13, direct decay to the ground state is nonnegligible, although the branching fraction is still small. The final term accounts for $3d - 3p$ decays.

Similarly, for $3d$ states, levels 15-26:

$$\frac{dN_i}{dt} = R_i - N_i A_i + \sum_{j=1,3} N_j (n_e C_{j,i}), \quad (\text{A.6})$$

and for the $3s'$ states, levels 27-28,

$$\frac{dN_i}{dt} = R_i - N_i A_i + \sum_{j=1,3} N_j (\phi_{j,i} + n_e C_{j,i}), \quad (\text{A.7})$$

The $3d$ states that are relevant primarily radiatively decay to $3p$ states, although level 16 has a nonnegligible branching fraction to ground, but the $3s'$ states only radiatively decay to $3s$ states.

Since we assume a steady state, all of the derivatives on the left-hand side of the equations equal zero. Thus, we can solve for the population of $3d$ level i :

$$N_i = \frac{R_i + \sum_{j=1,3} N_j (n_e C_{j,i})}{A_i}, \quad (\text{A.8})$$

and $3s'$ level i :

$$N_i = \frac{R_i + \sum_{j=1,3} N_j (\phi_{j,i} + n_e C_{j,i})}{A_i}. \quad (\text{A.9})$$

We can similarly solve for the $3p$ levels, substituting the expressions for $3d$ level populations

$$N_i = \frac{R_i + \sum_{j=1,3} [N_j (\phi_{j,i} + n_e C_{j,i})] + \sum_{k=3d} [R_k + \sum_{j=1,3} N_j (n_e C_{j,k})] F_{k,i}}{A_i}, \quad (\text{A.10})$$

where $F_{i,j} = A_{i,j}/A_i$ is the branching ratio to lower level j from upper level i (in this case, from $3d$ to $3p$ levels).

We can then substitute the expressions for N_i of the $3p$ and $3s'$ levels in the equation for N_3 , again setting the derivative to zero:

$$\begin{aligned} N_3 A_3 = & R_3 + \sum_{i=3p} \left[(R_i + \sum_{j=1,3} \{N_j (\phi_{j,i} + n_e C_{j,i})\}) + \sum_{k=3d} [R_k + \sum_{j=1,3} N_j (n_e C_{j,k})] F_{k,i} \right] F_{i,3} - N_3 \phi_{3,i} \\ & + \sum_{i=3s'} \left[(R_i + \sum_{j=1,3} N_j (\phi_{j,i} + n_e C_{j,i})) F_{i,3} - N_3 \phi_{3,i} \right] - \sum_{j=3s,3p,3d,3s'}^{j \neq 3} n_e N_3 C_{3,j} + n_e N_1 C_{1,3}. \end{aligned} \quad (\text{A.11})$$

Define $R'_j = R_j + \sum_{i=3p} [R_i F_{i,j} + \sum_{k=3d} R_k F_{k,i} F_{i,j}] + \sum_{i=3s'} R_i F_{i,j}$; this adds to R_j the line strength from the $3p$ channel that is expected to go to level j in the absence of photoexcitation, including cascades through $3p$ originating in $3d$, as well as cascades to $3s$ from $3s'$ states. Then,

$$\begin{aligned}
N_3 A_3 &= R'_3 + \sum_{i=3p} \left[\sum_{j=1,3} \{N_j(\phi_{j,i} + n_e C_{j,i} + \sum_{k=3d} n_e C_{j,k} F_{k,i}) F_{i,3}\} - N_3 \phi_{3,i} \right] \\
&+ \sum_{i=3s'} \sum_{j=1,3} [N_j(\phi_{j,i} + n_e C_{j,i}) F_{i,3} - N_3 \phi_{3,i}] - \sum_{\substack{j \neq 3 \\ j=3s, 3p, 3d, 3s'}} n_e N_3 C_{3,j} + n_e N_1 C_{1,3} \\
&= R'_3 + \sum_{i=3p} \left[N_1 (\phi_{1,i} + n_e (C_{1,i} + \sum_{k=3d} C_{1,k} F_{k,i})) F_{i,3} - N_3 (\phi_{3,i} (1 - F_{i,3}) + n_e \{C_{3,i} (1 - F_{i,3}) \right. \\
&+ \left. \sum_{k=3d} C_{3,k} (1 - F_{k,i} F_{i,3}) \}) \right] \\
&+ \sum_{i=3s'} [N_1 (\phi_{1,i} + n_e C_{1,i}) F_{i,3} - N_3 (\phi_{3,i} + n_e C_{3,i}) (1 - F_{i,3})] - \sum_{\substack{j \neq 3 \\ j=3s}} n_e N_3 C_{3,j} + n_e N_1 C_{1,3}.
\end{aligned} \tag{A.12}$$

Moving terms with N_3 to the left, we have

$$\begin{aligned}
N_3 [A_3 + \sum_{i=3p} \{ \phi_{3,i} (1 - F_{i,3}) + n_e (C_{3,i} (1 - F_{i,3}) + \sum_{k=3d} C_{3,k} (1 - F_{k,i} F_{i,3})) \}] \\
+ \sum_{i=3s'} (\phi_{3,i} + n_e C_{3,i}) (1 - F_{i,3}) + \sum_{\substack{j \neq 3 \\ j=3s}} n_e C_{3,j} \\
= R'_3 + N_1 \left[\sum_{i=3p} (\phi_{1,i} + n_e (C_{1,i} + \sum_{k=3d} C_{1,k} F_{k,i})) F_{i,3} + \sum_{i=3s'} (\phi_{1,i} + n_e C_{1,i}) F_{i,3} + n_e C_{1,3} \right].
\end{aligned} \tag{A.13}$$

Now define

$$P_{i,j} \equiv \frac{1}{A_i} \sum_{k=3p, 3s'} \phi_{i,k} F_{k,j}, \tag{A.14}$$

and

$$P_i \equiv \frac{1}{A_i} \sum_{k=3p, 3s'} \phi_{i,k} (1 - F_{k,i}). \tag{A.15}$$

$P_{i,j}$ gives the effective photoexcitation rate from 3s level i to 3s level j , summed over all

intermediate $3p$ and $3s'$ states, and normalized to the decay rate from level i , A_i ; while P_i similarly gives the effective normalized photoexcitation rate from $3s$ level i to *all other* levels combined. For the latter, this also includes the small fraction of direct decays to ground from $3p$ levels. Photoexcitation via $3s'$ levels can usually be neglected, since the transition energies to these levels are much higher than to $3p$ levels, and the UV flux is thus much lower.

Similarly, define

$$\frac{1}{n_{i,j}} \equiv \frac{1}{A_i} \left[\sum_{k=3p} (C_{i,k} + \sum_{m=3d} C_{i,m} F_{m,k}) F_{k,j} + \sum_{k=3s'} C_{i,k} F_{k,j} + C_{i,j} \right], \quad (\text{A.16})$$

and

$$\frac{1}{n_i} \equiv \frac{1}{A_i} \left[\sum_{k=3p} (C_{i,k}(1 - F_{k,i}) + \sum_{m=3d} C_{i,m}(1 - F_{m,k}F_{k,i})) + \sum_{k=3s'} C_{i,k}(1 - F_{k,i}) + \sum_{\substack{k \neq i \\ k=3s}} C_{i,k} \right]. \quad (\text{A.17})$$

Parameters $n_{i,j}$ and n_i are effectively critical densities, with $n_e/n_{i,j}$ giving the effective rate of collisional feeding from level i to level j summed over all intermediate states, and normalized to A_i ; and with n_e/n_i summing over all states other than the initial state i .

Using the definitions for $P_{i,j}$, P_i , $n_{i,j}$, and n_i , we can write the expressions for N_3 and N_1 as

$$N_3 A_3 = \frac{R'_3 + N_1 A_1 [P_{1,3} + n_e/n_{1,3}]}{1 + P_3 + n_e/n_3}, \quad (\text{A.18})$$

$$N_1 A_1 = \frac{R'_1 + N_3 A_3 [P_{3,1} + n_e/n_{3,1}]}{1 + P_1 + n_e/n_1}. \quad (\text{A.19})$$

Then, solve the two equations to obtain independent expressions for N_3 and N_1 :

$$N_3A_3 = \frac{R'_3(1 + P_1 + n_e/n_1) + R'_1[P_{1,3} + n_e/n_{1,3}]}{(1 + P_1 + n_e/n_1)(1 + P_3 + n_e/n_3) - [P_{3,1} + n_e/n_{3,1}][P_{1,3} + n_e/n_{1,3}]}; \quad (\text{A.20})$$

$$N_1A_1 = \frac{R'_1(1 + P_3 + n_e/n_3) + R'_3[P_{3,1} + n_e/n_{3,1}]}{(1 + P_1 + n_e/n_1)(1 + P_3 + n_e/n_3) - [P_{3,1} + n_e/n_{3,1}][P_{1,3} + n_e/n_{1,3}]} . \quad (\text{A.21})$$

One can obtain similar expressions for levels 2 and 4, which are left in terms of the populations of levels 1 and 3:

$$N_2A_2 = R'_2 + N_1A_1(P_{1,2} + n_e/n_{1,2}) + N_3A_3(1 + P_{3,2} + n_e/n_{3,2}); \quad (\text{A.22})$$

$$N_4A_4 = R'_4 + N_1A_1(P_{1,4} + n_e/n_{1,4}) + N_3A_3(P_{3,4} + n_e/n_{3,4}). \quad (\text{A.23})$$

Next, consider the line strengths in the limit of zero photoexcitation and low density, i.e. all P_i and $P_{i,j}$ are zero, and $n_e \ll n_i$ and $n_{i,j}$. Then, $N_1A_1 = R'_1$; $N_2A_2 = R'_2 + R'_3$; $N_3A_3 = R'_3$; and $N_4A_4 = R'_4$. It is not an accident or overcount that R'_3 shows up in the expressions for levels 2 and 3; this is because electrons populating level 3 will decay twice, first from level 3 to 2, emitting a 10.8 eV photon, and then from level 2 to 0, emitting a 727.1 eV photon.

The observable line ratios for levels 1, 2, and 4 can be calculated as

$$\mathcal{R}_i = \frac{N_iA_i}{\sum_{j=1,2,4} N_jA_j}. \quad (\text{A.24})$$

One can also evaluate this expression for \mathcal{R}_3 ; it gives the ratio of the flux in the 10.8 eV line to the sum of the three $3s - 2p$ lines.

In the limit of low density and UV flux, the denominator sums to $\sum_{i=1}^4 R'_i$. Define $\mathcal{R}_i^\circ =$

$R'_i / \sum_{j=1}^4 R'_j$; these quantities give the values of \mathcal{R}_i in the limit of low density and low UV flux, with the exception that $\mathcal{R}_2 = \mathcal{R}_2^\circ + \mathcal{R}_3^\circ$.

Provisionally neglect the weak decay channels from levels 6, 9, 13, and 16 to ground; in this case the denominator of Equation A.24 is a constant. Then,

$$\mathcal{R}_1 = \frac{\mathcal{R}_1^\circ(1 + P_3 + n_e/n_3) + \mathcal{R}_3^\circ(P_{3,1} + n_e/n_{3,1})}{(1 + P_1 + n_e/n_1)(1 + P_3 + n_e/n_3) - (P_{3,1} + n_e/n_{3,1})(P_{1,3} + n_e/n_{1,3})} \quad (\text{A.25})$$

$$\mathcal{R}_2 = \mathcal{R}_2^\circ + \mathcal{R}_1(P_{1,2} + n_e/n_{1,2}) + \mathcal{R}_3(1 + P_{3,2} + n_e/n_{3,2}); \quad (\text{A.26})$$

$$\mathcal{R}_3 = \frac{\mathcal{R}_3^\circ(1 + P_1 + n_e/n_1) + \mathcal{R}_1^\circ(P_{1,3} + n_e/n_{1,3})}{(1 + P_1 + n_e/n_1)(1 + P_3 + n_e/n_3) - (P_{3,1} + n_e/n_{3,1})(P_{1,3} + n_e/n_{1,3})}; \quad (\text{A.27})$$

$$\mathcal{R}_4 = \mathcal{R}_4^\circ + \mathcal{R}_1(P_{1,4} + n_e/n_{1,4}) + \mathcal{R}_3(P_{3,4} + n_e/n_{3,4}). \quad (\text{A.28})$$

Again, the expressions for levels 2 and 4 can be evaluated using the results for levels 1 and 3.

Now let us consider the effect of neglecting direct decays to ground of $3p$ and $3d$ excited states in these expressions. Since the denominator in Equation A.24 is the total $3s$ line strength in the limit of low density and UV flux, in general the resulting line ratios will sum to slightly less than unity, with the remainder accounted for by strengthening of the $2p - 3p$ and $2p - 3d$ transitions. Since we are only interested in the *relative* strengths of the $2p - 3s$ transitions, we can simply renormalize the ratios to sum to unity.

The values for \mathcal{R}_i° can be fixed from theory, evaluated at low UV flux and low density; or from experiments at sufficiently low density; or from astrophysical observations of low-density, low-UV flux objects. The values for $P_{i,j}$ and P_i can be calculated given the relevant oscillator strengths, A values, and branching ratios, as well as the input UV spectrum, and similarly for

$n_{i,j}$ and n_i with collision strengths, which are weakly temperature dependent. Finally, assuming trivial radiative transfer in the circumstellar environment, a common geometrical dilution term $W(r)$ can be factored out from all P ; or if not, $J_\nu(r)$ must be evaluated for all relevant wavelengths over the circumstellar environment.

Appendix B: Facilities and Software Used in Dissertation

B.1 Facilities

The experimental data in Chapter 3 was performed at FLASH-EBIT ([Epp et al., 2010](#)) at the Max Planck Institute for Nuclear Physics in Heidelberg, Germany (MPIK). The experimental transition energies in Chapter 4 were calculated from measurements taken by PolarX-EBIT ([Micke et al., 2018](#)) at the Petra III P04 synchrotron beamline at DESY in Hamburg, Germany.

The theoretical calculations in Chapter 3 were performed using the NASA Center for Climate Simulation `discover` supercluster.

B.2 Software

1. AstroPy ([Astropy Collaboration et al., 2013](#))
2. CIAO ([Fruscione et al., 2006](#))
3. Flexible Atomic Code ([Gu, 2008](#))
4. HEASoft ([Nasa High Energy Astrophysics Science Archive Research Center \(Heasarc\), 2014](#))
5. Imfit ([Newville et al., 2016](#))

6. Matplotlib ([Hunter, 2007](#))
7. NumPy ([van der Walt et al., 2011](#))
8. XMM SAS ([Gabriel et al., 2004](#))
9. SciPy ([Virtanen et al., 2020](#))
10. Tlusty ([Hubeny & Lanz, 2011](#))
11. XSPEC ([Arnaud, 1996](#))

Bibliography

- Ames, J. S. 1896, *The Astrophysical Journal*, 3, 294
- Amusia, M. Y., Chernysheva, L. V., & Natarajan, L. 1998, *Computers in Physics*, 12, 148
- Apruzese, J., Davis, J., Whitney, K., et al. 2002, *Physics of Plasmas*, 9, 2411
- Arnaud, K. A. 1996, in ASP Conf. Ser., Vol. 101, *Astronomical Data Analysis Software and Systems V*, ed. G. H. Jacoby & J. Barnes, (San Francisco, CA: ASP), 17
- Asplund, M., Grevesse, N., Sauval, A. J., & Scott, P. 2009, *Annual Review of Astronomy and Astrophysics*, 47, 481
- Astropy Collaboration, Robitaille, T. P., Tollerud, E. J., et al. 2013, *Astronomy and Astrophysics*, 558, A33
- Bandler, S. R., Adams, J. S., Amatucci, E. G., et al. 2023, *Journal of Astronomical Telescopes, Instruments, and Systems*, 9, 041002
- Bar-Shalom, A., Klapisch, M., & Oreg, J. 2001, *Journal of Quantitative Spectroscopy and Radiative Transfer*, 71, 169
- Barret, D. et al. 2016, *Proc. SPIE*, 9905, 99052F
- Bearden, J. A. 1967, *Reviews of Modern Physics*, 39, 78
- Beerwerth, R., Buhr, T., Perry-Sassmannshausen, A., et al. 2019, *The Astrophysical Journal*, 887, 189
- Behar, E., Cottam, J., & Kahn, S. M. 2001a, *The Astrophysical Journal*, 548, 966
- Behar, E., Sako, M., & Kahn, S. M. 2001b, *The Astrophysical Journal*, 563, 497
- Beiersdorfer, P. 2003, *Annual Review of Astron and Astrophys*, 41, 343
- Beiersdorfer, P., Behar, E., Boyce, K. R., et al. 2002, *Astrophysical Journal Letters*, 576, L169
- Beiersdorfer, P., Bitter, M., Goeler, S. v., & Hill, K. W. 2004, *The Astrophysical Journal*, 610, 616

- Beiersdorfer, P., Bode, M. P., Ishikawa, Y., & Diaz, F. 2014, *The Astrophysical Journal*, 793, 99
- Beiersdorfer, P., Brown, G., Hell, N., & Santana, J. 2017a, *Nuclear Instruments and Methods in Physics Research Section B: Beam Interactions with Materials and Atoms*, 408, 67
- Beiersdorfer, P., Brown, G. V., & Laska, A. 2017b, *AIP Conference Proceedings*, 1811, 040001
- Beiersdorfer, P., Crespo López-Urrutia, J. R., & Träbert, E. 2016, *The Astrophysical Journal*, 817, 67
- Beiersdorfer, P., Hell, N., & Lepson, J. K. 2018, *The Astrophysical Journal*, 864, 24
- Beiersdorfer, P., Lepson, J. K., Gu, M. F., & Bitter, M. 2017, *The Astrophysical Journal*, 850, 57
- Beiersdorfer, P., Phillips, T., Jacobs, V. L., et al. 1993, *The Astrophysical Journal*, 409, 846
- Beiersdorfer, P., Phillips, T. W., Wong, K. L., Marrs, R. E., & Vogel, D. A. 1992, *Physical Review A: General Physics*, 46, 3812
- Beiersdorfer, P., Scofield, J. H., & Osterheld, A. L. 2003, *Physical Review Letters*, 90, 235003
- Beiersdorfer, P., Vogel, D. A., Reed, K. J., et al. 1996, *Physical Review A*, 53, 3974
- Bernitt, S., Brown, G. V., Rudolph, J. K., et al. 2012, *Nature*, 492, 225
- Betancourt-Martinez, G. L., Adams, J., Bandler, S., et al. 2014, in *Society of Photo-Optical Instrumentation Engineers (SPIE) Conference Series*, Vol. 9144, *Space Telescopes and Instrumentation 2014: Ultraviolet to Gamma Ray*, ed. T. Takahashi, J.-W. A. den Herder, & M. Bautz, 91443U
- Betancourt-Martinez, G. L., Beiersdorfer, P., Brown, G. V., et al. 2018, *The Astrophysical Journal*, 868, L17
- Bitter, M., Gu, M. F., Vainshtein, L. A., et al. 2003, *Physical Review Letters*, 91, 265001
- Blancard, C., Cubaynes, D., Guilbaud, S., & Bizau, J.-M. 2018, *The Astrophysical Journal*, 853, 32
- Blumenthal, G. R., Drake, G. W. F., & Tucker, W. H. 1972, *The Astrophysical Journal*, 172, 205
- Blustin, A. J., Branduardi-Raymont, G., Behar, E., et al. 2002, *Astronomy and Astrophysics*, 392, 453
- Bouret, J.-C., Hillier, D. J., Lanz, T., & Fullerton, A. W. 2012, *Astronomy and Astrophysics*, 544, A67
- Bregman, J. N., Schulman, E., & Tomisaka, K. 1995, *The Astrophysical Journal*, 439, 155
- Brickhouse, N., Cranmer, S. R., Dupree, A. K., Luna, G. J. M., & Wolk, S. 2009, in *Chandra's First Decade of Discovery*, ed. S. Wolk, A. Fruscione, & D. Swartz, 8

- Brown, G. V. 2008, *Can. J. Phys.*, 86, 199
- Brown, G. V., Beiersdorfer, P., Chen, H., Chen, M. H., & Reed, K. J. 2001, *The Astrophysical Journal Lett.*, 557, L75
- Brown, G. V., Beiersdorfer, P., Chen, H., et al. 2006, *Physical Review Letters*, 96, 253201
- Brown, G. V., Beiersdorfer, P., Chen, H., et al. 2006, *Phys. Rev. Lett.*, 96, 253201
- Brown, G. V., Beiersdorfer, P., Liedahl, D. A., Widmann, K., & Kahn, S. M. 1998, *The Astrophysical Journal*, 502, 1015
- Brown, G. V., Beiersdorfer, P., & Widmann, K. 2001, *Physical Review A*, 63, 032719
- Burgess, A. 1964, *The Astrophysical Journal*, 139, 776
- Burrows, D. N., Hill, J. E., Nousek, J. A., et al. 2005, *Space Science Reviews*, 120, 165
- Canizares, C. R., Huenemoerder, D. P., Davis, D. S., et al. 2000, *The Astrophysical Journal Lett.*, 539, L41
- Cash, W. 1979, *The Astrophysical Journal*, 228, 939
- Cassinelli, J. P., Miller, N. A., Waldron, W. L., MacFarlane, J. J., & Cohen, D. H. 2001, *The Astrophysical Journal*, 554, L55
- Castor, J. I., Abbott, D. C., & Klein, R. I. 1975, *The Astrophysical Journal*, 195, 157
- Chen, G. X. 2007, *Phys. Rev. A*, 76, 062708
- Chen, G.-X. 2008, *Phys. Rev. A*, 77, 022701
- Chen, G. X. 2011, *Phys. Rev. A*, 84, 012705
- Chen, G. X. & Pradhan, A. K. 2002, *Phys. Rev. Lett.*, 89, 013202
- Chen, G.-X., Pradhan, A. K., & Eissner, W. 2003, *Journal of Physics B Atomic Molecular Physics*, 36, 453
- Chen, W.-C. 2017, *Astronomy and Astrophysics*, 606, A60
- Chevalier, R. A. & Clegg, A. W. 1985, *Nature*, 317, 44
- Clark, G. W. 1982, *Physics Today*, 35, 26
- Cohen, D. H., de Messières, G. E., MacFarlane, J. J., et al. 2003, *The Astrophysical Journal*, 586, 495
- Cohen, D. H., Leutenegger, M. A., Grizzard, K. T., et al. 2006, *Monthly Notices of the Royal Astronomical Society*, 368, 1905

- Cohen, D. H., Leutenegger, M. A., Wollman, E. E., et al. 2010, *Monthly Notices of the Royal Astronomical Society*, 405, 2391
- Cohen, D. H., Li, Z., Gayley, K. G., et al. 2014, *Monthly Notices of the Royal Astronomical Society*, 444, 3729
- Condon, E. U. & Shortley, G. H. 1963, *The theory of atomic spectra* (Cambridge: University Press)
- Cowan, R. D. 1981, *The theory of atomic structure and spectra* (Los Alamos Series in Basic and Applied Sciences, Berkeley: University of California Press)
- Crespo López-Urrutia, J. R. & Beiersdorfer, P. 2010, *The Astrophysical Journal*, 721, 576
- David-Uraz, A., Wade, G. A., Petit, V., et al. 2014, *Monthly Notices of the Royal Astronomical Society*, 444, 429
- de Plaa, J., Zhuravleva, I., Werner, N., et al. 2012, *A&A*, 539, A34
- Decaux, V., Beiersdorfer, P., Kahn, S. M., & Jacobs, V. L. 1997, *The Astrophysical Journal*, 482, 1076
- Del Zanna, G., Dere, K. P., Young, P. R., Landi, E., & Mason, H. E. 2015, *A&A*, 582, A56
- Dilling, J., Baartman, R., Bricault, P., et al. 2006, *International Journal of Mass Spectrometry*, 251, 198
- Dirac, P. A. M. 1928, *Proceedings of the Royal Society of London Series A*, 117, 610
- Donati, J.-F., Howarth, I. D., Jardine, M. M., et al. 2006, *Monthly Notices of the Royal Astronomical Society*, 370, 629
- Dorman, B., Arnaud, K. A., & Gordon, C. A. 2003, in *AAS/High Energy Astrophysics Division*, Vol. 7, *AAS/High Energy Astrophysics Division #7*, 22.10
- Doron, R. & Behar, E. 2002, *The Astrophysical Journal*, 574, 518
- Doron, R. & Behar, E. 2002, *The Astrophysical Journal*, 574, 518
- Dravins, D. 2003, in *Modelling of Stellar Atmospheres*, ed. N. Piskunov, W. W. Weiss, & D. F. Gray, Vol. 210, E4
- Dubau, J. & Volonte, S. 1980, *Reports on Progress in Physics*, 43, 199
- Eissner, W., Jones, M., & Nussbaumer, H. 1974, *Computer Physics Communications*, 8, 270
- Epp, S. W., Crespo López-Urrutia, J. R., Simon, M. C., et al. 2010, *Journal of Physics B Atomic Molecular Physics*, 43, 194008
- Ezoe, Y., Ishisaki, Y., Fujimoto, R., et al. 2020, *Cryogenics*, 108, 103016

- Ezoe, Y., Ohashi, T., & Mitsuda, K. 2021, *Reviews of Modern Plasma Physics*, 5, 4
- Fabian, A. C., Iwasawa, K., Reynolds, C. S., & Young, A. J. 2000, *Publications of the ASP*, 112, 1145
- Feldmeier, A., Puls, J., & Pauldrach, A. W. A. 1997, *Astronomy and Astrophysics*, 322, 878
- Fischer, C. F. 2000, *Computer Physics Communications*, 128, 635
- Flanagan, K. A., Canizares, C. R., Dewey, D., et al. 2003, in *Society of Photo-Optical Instrumentation Engineers (SPIE) Conference Series*, Vol. 4851, *X-Ray and Gamma-Ray Telescopes and Instruments for Astronomy.*, ed. J. E. Truemper & H. D. Tananbaum, 45–56
- Foster, A. R., Ji, L., Smith, R. K., & Brickhouse, N. S. 2012, *The Astrophysical Journal*, 756, 128
- Fournier, K. B. & Hansen, S. B. 2005, *Physical Review A*, 71, 012717
- Fowler, J. W., O’Neil, G. C., Alpert, B. K., et al. 2021, *Metrologia*, 58, 015016
- Friedman, H., Lichtman, S. W., & Byram, E. T. 1951, *Phys. Rev.*, 83, 1025
- Fruscione, A., McDowell, J. C., Allen, G. E., et al. 2006, in *Society of Photo-Optical Instrumentation Engineers (SPIE) Conference Series*, Vol. 6270, *Observatory Operations: Strategies, Processes, and Systems*, ed. D. R. Silva & R. E. Doxsey, 62701V
- Fukugita, M., Hogan, C. J., & Peebles, P. J. E. 1998, *The Astrophysical Journal*, 503, 518
- Fullerton, A. W., Massa, D. L., & Prinja, R. K. 2006, *The Astrophysical Journal*, 637, 1025
- Gabriel, A. H. 1972, *Monthly Notices of the Royal Astronomical Society*, 160, 99
- Gabriel, A. H. & Jordan, C. 1969, *Monthly Notices of the Royal Astronomical Society*, 145, 241
- Gabriel, C., Denby, M., Fyfe, D. J., et al. 2004, in *Astronomical Society of the Pacific Conference Series*, Vol. 314, *Astronomical Data Analysis Software and Systems (ADASS) XIII*, ed. F. Ochsenbein, M. G. Allen, & D. Egret, 759
- Giacconi, R. 1980, *Scientific American*, 242, 80
- Giacconi, R., Gursky, H., Kellogg, E., Schreier, E., & Tananbaum, H. 1971a, *Astrophysical Journal Letters*, 167, L67
- Giacconi, R., Gursky, H., Paolini, F. R., & Rossi, B. B. 1962, *Phys. Rev. Lett.*, 9, 439
- Giacconi, R., Kellogg, E., Gorenstein, P., Gursky, H., & Tananbaum, H. 1971b, *Astrophysical Journal Letters*, 165, L27
- Gilfanov, M. R., Syunyaev, R. A., & Churazov, E. M. 1987, *Soviet Astronomy Letters*, 13, 3
- Gillaspy, J. D., Lin, T., Tedesco, L., et al. 2011, *The Astrophysical Journal*, 728, 132

- Glasser, C. A., Odell, C. E., & Seufert, S. E. 1994, *IEEE Transactions on Nuclear Science*, 41, 1343
- Grant, I. P., McKenzie, B. J., Norrington, P. H., Mayers, D. F., & Pyper, N. C. 1980, *Computer Physics Communications*, 21, 207
- Grell, G. J., Leutenegger, M. A., Amaro, P., Crespo López-Urrutia, J. R., & Shah, C. 2024, *The Astrophysical Journal*, 971, 78
- Grell, G. J., Leutenegger, M. A., & Shah, C. 2021, *The Astrophysical Journal*, 917, 105
- Griffiths, R. E., Ptak, A., Feigelson, E. D., et al. 2000, *Science*, 290, 1325
- Grilo, F., Shah, C., Kühn, S., et al. 2021, *The Astrophysical Journal*, 913, 140
- Gu, L., Raassen, A. J. J., Mao, J., et al. 2019, *Astronomy and Astrophysics*, 627, A51
- Gu, L., Shah, C., Mao, J., et al. 2020, *Astronomy and Astrophysics*, 641, A93
- Gu, M. F. 2003, *The Astrophysical Journal*, 582, 1241
- Gu, M. F. 2008, *Canadian Journal of Physics*, 86, 675
- Gu, M. F., Holczer, T., Behar, E., & Kahn, S. M. 2006, *The Astrophysical Journal*, 641, 1227
- Guedel, M. & Naze, Y. 2009, *Astronomy and Astrophysics Review*, 17, 309
- Harnden, F. R., Branduardi, G., Gorenstein, P., et al. 1979, *The Astrophysical Journal*, 234, L51
- Heckman, T. M., Armus, L., & Miley, G. K. 1990, *Astrophysical Journal Supplement*, 74, 833
- Henke, B. L., Gullikson, E. M., & Davis, J. C. 1993, *Atomic Data and Nuclear Data Tables*, 54, 181
- Hervé, A., Rauw, G., & Nazé, Y. 2013, *Astronomy and Astrophysics*, 551, A83
- Hitomi Collaboration, Aharonian, F., Akamatsu, H., et al. 2018, *Publications of the ASJ*, 70, 10
- Hitomi Collaboration, Aharonian, F., Akamatsu, H., et al. 2017, *Nature*, 551, 478
- Hodges-Kluck, E., Lopez, L. A., Yukita, M., et al. 2019, *Astro2020: Decadal Survey on Astronomy and Astrophysics*, 51, 257
- Holczer, T., Behar, E., & Kaspi, S. 2007, *The Astrophysical Journal*, 663, 799
- Hoopes, C. G., Heckman, T. M., Strickland, D. K., et al. 2005, *Astrophysical Journal Letters*, 619, L99
- Hubeny, I. & Lanz, T. 2011, *Astrophysics Source Code Library*, record ascl:1109.021
- Hunter, J. D. 2007, *Computing in Science and Engineering*, 9, 90

- Jansen, F., Lumb, D., Altieri, B., et al. 2001, *Astronomy and Astrophysics*, 365, L1
- Jönsson, P., Gaigalas, G., Bieroń, J., Fischer, C. F., & Grant, I. P. 2013, *Computer Physics Communications*, 184, 2197
- Jovanović, P., Borka Jovanović, V., & Borka, D. 2011, *Baltic Astronomy*, 20, 468
- Kaastra, J. S. 2017, *Astronomische Nachrichten*, 338, 146
- Kaastra, J. S., Ferrigno, C., Tamura, T., et al. 2001, *Astronomy and Astrophysics*, 365, L99
- Kaastra, J. S. & Mewe, R. 1993, *Astronomy and Astrophysics Supplement*, 97, 443
- Kaastra, J. S., Mewe, R., & Nieuwenhuijzen, H. 1996a, in *UV and X-ray Spectroscopy of Astrophysical and Laboratory Plasmas*, 411–414
- Kaastra, J. S., Mewe, R., & Nieuwenhuijzen, H. 1996b, in *UV and X-ray Spectroscopy of Astrophysical and Laboratory Plasmas*, 411–414
- Kahn, S. M., Behar, E., Kinkhabwala, A., & Savin, D. W. 2002, *Philosophical Transactions of the Royal Society of London. Series A: Mathematical, Physical and Engineering Sciences*, 360, 1923
- Kahn, S. M., Leutenegger, M. A., Cottam, J., et al. 2001a, *Astronomy and Astrophysics*, 365, L312
- Kahn, S. M., Leutenegger, M. A., Cottam, J., et al. 2001b, *Astronomy and Astrophysics*, 365, L312
- Kallman, T., Daniel, A. E., Marshall, H., et al. 2014, *The Astrophysical Journal*, 780, 121
- Kaneda, H., Ishihara, D., Suzuki, T., et al. 2010, *Astronomy and Astrophysics*, 514, A14
- Kastner, J. H., Huenemoerder, D. P., Schulz, N. S., Canizares, C. R., & Weintraub, D. A. 2002, *The Astrophysical Journal*, 567, 434
- Kelleher, D. E., Martin, W. C., Wiese, W. L., et al. 1999, *Physica Scripta Volume T*, 83, 158
- Kelley, R. L., Akamatsu, H., Azzarello, P., et al. 2016, in *Proceedings of SPIE, Vol. 9905, Space Telescopes and Instrumentation 2016: Ultraviolet to Gamma Ray*, 99050V
- Kellogg, E., Tananbaum, H., Harnden, F. R., J., et al. 1973, *The Astrophysical Journal*, 183, 935
- Kelly, R. L. 1987, *Journal of Physical and Chemical Reference Data*, 17
- Khodja, H. & Briand, J. P. 1997, *Physica Scripta*, 1997, 113
- Kinkhabwala, A., Sako, M., Behar, E., et al. 2002, *The Astrophysical Journal*, 575, 732
- Kochukhov, O. & Sudnik, N. 2013, *Astronomy and Astrophysics*, 554, A93
- Koyama, K., Hyodo, Y., Inui, T., et al. 2007, *Publications of the ASJ*, 59, 245

- Kramer, R. H., Cohen, D. H., & Owocki, S. P. 2003, *The Astrophysical Journal*, 592, 532
- Kühn, S., Cheung, C., Oreshkina, N. S., et al. 2022, *Physical Review Letters*, 129, 245001
- Kühn, S., Shah, C., López-Urrutia, J. R. C., et al. 2020, *Phys. Rev. Lett.*, 124, 225001
- Lamers, H. J. G. L. M. & Leitherer, C. 1993, *The Astrophysical Journal*, 412, 771
- Laming, J. M., Kink, I., Takacs, E., et al. 2000, *The Astrophysical Journal Letters*, 545, L161
- Lanz, T. & Hubeny, I. 2003, *The Astrophysical Journal Supplement Series*, 146, 417
- Lanz, T. & Hubeny, I. 2007, *The Astrophysical Journal Supplement Series*, 169, 83
- Lehnert, M. D. & Heckman, T. M. 1996, *The Astrophysical Journal*, 472, 546
- Lepson, J. K., Beiersdorfer, P., Behar, E., & Kahn, S. M. 2003, *The Astrophysical Journal*, 590, 604
- Leutenegger, M. A., Cohen, D. H., & Owocki, S. P. 2012, in American Institute of Physics Conference Series, Vol. 1438, American Institute of Physics Conference Series, ed. K. Aggarwal, Dr. & F. Shearer, Dr., 111–117
- Leutenegger, M. A., Cohen, D. H., Sundqvist, J. O., & Owocki, S. P. 2013, *The Astrophysical Journal*, 770, 80
- Leutenegger, M. A., Cohen, D. H., Zsargó, J., et al. 2010, *The Astrophysical Journal*, 719, 1767
- Leutenegger, M. A., Kühn, S., Micke, P., et al. 2020, *Physical Review Letters*, 125, 243001
- Leutenegger, M. A., Paerels, F. B. S., Kahn, S. M., & Cohen, D. H. 2006, *The Astrophysical Journal*, 650, 1096
- Levine, M. A., Marrs, R. E., Henderson, J. R., Knapp, D. A., & Schneider, M. B. 1988, *Physica Scripta Volume T*, 22, 157
- Liang, S., Lu, Q., Wang, X., et al. 2019, *Review of Scientific Instruments*, 90, 093301
- Liedahl, D. A. 2005, in American Institute of Physics Conference Series, Vol. 774, X-ray Diagnostics of Astrophysical Plasmas: Theory, Experiment, and Observation, ed. R. Smith (AIP Conference Proceedings), 99–108
- Liedahl, D. A., Osterheld, A. L., & Goldstein, W. H. 1995, *Astrophysical Journal Letters*, 438, L115
- Liu, J., Gou, L., Yuan, W., & Mao, S. 2014, *Monthly Notices of the Royal Astronomical Society*, 437, L76
- Loch, S. D., Pindzola, M. S., Ballance, C. P., & Griffin, D. C. 2006, *Journal of Physics B Atomic Molecular Physics*, 39, 85

- Lopez, L. A., Mathur, S., Nguyen, D. D., Thompson, T. A., & Olivier, G. M. 2020, *The Astrophysical Journal*, 904, 152
- Loulergue, M. & Nussbaumer, H. 1975, *Astronomy and Astrophysics*, 45, 125
- Lucy, L. B. & Solomon, P. M. 1970, *The Astrophysical Journal*, 159, 879
- Madison, D. H. & Shelton, W. N. 1973, *Phys. Rev. A*, 7, 499
- Marcum, P. M., O'Connell, R. W., Fanelli, M. N., et al. 2001, *Astrophysical Journal Supplement Series*, 132, 129
- Martini, P., Leroy, A. K., Mangum, J. G., et al. 2018, *The Astrophysical Journal*, 856, 61
- Mauche, C. W., Liedahl, D. A., & Fournier, K. B. 2001, *The Astrophysical Journal*, 560, 992
- May, M. J., Beiersdorfer, P., Dunn, J., et al. 2005, *The Astrophysical Journal Supplement Series*, 158, 230
- McCammon, D. 2005, arXiv: Instrumentation and Detectors
- McDonald, J. W., Schneider, D., Clark, M. W., & Dewitt, D. 1992, *Phys. Rev. Lett.*, 68, 2297
- McKeith, C. D., Greve, A., Downes, D., & Prada, F. 1995, *Astronomy and Astrophysics*, 293, 703
- Mewe, R. 1999, LNP Vol. 520: X-Ray Spectroscopy in Astrophysics, 520, 109
- Mewe, R., Raassen, A. J. J., Cassinelli, J. P., et al. 2003, *Astronomy and Astrophysics*, 398, 203
- Mewe, R., Raassen, A. J. J., Drake, J. J., et al. 2001, *A&A*, 368, 888
- Micke, P., Kühn, S., Buchauer, L., et al. 2018, *Review of Scientific Instruments*, 89, 063109
- Morton, D. C. 1967, *The Astrophysical Journal*, 150, 535
- Moseley, S. H., Mather, J. C., & McCammon, D. 1984, *Journal of Applied Physics*, 56, 1257
- Mott, N. F. & Massey, H. S. W. 1933, *Theory of Atomic Collisions* (Clarendon Press)
- Murray, S. S., Fabbiano, G., Fabian, A. C., Epstein, A., & Giacconi, R. 1979, *Astrophysical Journal Letters*, 234, L69
- Nakashima, S., Inoue, Y., Yamasaki, N., et al. 2018, *The Astrophysical Journal*, 862, 34
- Nasa High Energy Astrophysics Science Archive Research Center (Heasarc). 2014, *Astrophysics Source Code Library*, record ascl:1408.004
- Ness, J., Brickhouse, N. S., Drake, J. J., & Huenemoerder, D. P. 2003, *The Astrophysical Journal*, 598, 1277
- Ness, J. U. & Schmitt, J. H. M. M. 2005, *Astronomy and Astrophysics*, 444, L41

- Newville, M., Stensitzki, T., Allen, D. B., et al. 2016, Astrophysics Source Code Library, record ascl:1606.014
- Oda, M., Gorenstein, P., Gursky, H., et al. 1971, *Astrophysical Journal Letters*, 166, L1
- Ogorzalek, A., Zhuravleva, I., Allen, S. W., et al. 2017, *Monthly Notices of the Royal Astronomical Society*, 472, 1659
- Owocki, S. P., Castor, J. I., & Rybicki, G. B. 1988, *The Astrophysical Journal*, 335, 914
- Owocki, S. P. & Cohen, D. H. 2001, *The Astrophysical Journal*, 559, 1108
- Owocki, S. P. & Puls, J. 1999, *The Astrophysical Journal*, 510, 355
- Paerels, F. B. S. & Kahn, S. M. 2003, *Annual Review of Astron and Astrophys*, 41, 291
- Parkinson, J. H. 1973, *Astronomy and Astrophysics*, 24, 215
- Penetrante, B. M., Bardsley, J. N., Dewitt, D., Clark, M., & Schneider, D. 1991, *Physical Review A*, 43, 4861
- Peterson, J. R., Paerels, F. B. S., Kaastra, J. S., et al. 2001, *Astronomy and Astrophysics*, 365, L104
- Phillips, K. J. H., Greer, C. J., Bhatia, A. K., & Keenan, F. P. 1996, *Astrophysical Journal Letters*, 469, L57
- Phillips, K. J. H., Mathioudakis, M., Huenemoerder, D. P., et al. 2001, *Monthly Notices of the Royal Astronomical Society*, 325, 1500
- Phillips, K. J. H., Mewe, R., Harra-Murnion, L. K., et al. 1999, *Astronomy and Astrophysics*, 138, 381
- Pindzola, M. S., Loch, S. D., Ballance, C. P., & Griffin, D. C. 2006, *Phys. Rev. A*, 73, 012718
- Pinto, C., Middleton, M. J., & Fabian, A. C. 2016, *Nature*, 533, 64
- Pollock, A. M. T. 2007, *Astronomy and Astrophysics*, 463, 1111
- Porter, F. S., Boyce, K. R., Chiao, M. P., et al. 2018, *Journal of Astronomical Telescopes, Instruments, and Systems*, 4, 011218
- Pradhan, A. K. & Nahar, S. N. 2011, *Atomic Astrophysics and Spectroscopy* (Cambridge University Press)
- Puebla, R. E., Hillier, D. J., Zsargó, J., Cohen, D. H., & Leutenegger, M. A. 2016, *Monthly Notices of the Royal Astronomical Society*, 456, 2907
- Puls, J., Markova, N., Scuderi, S., et al. 2006, *Astronomy and Astrophysics*, 454, 625
- Raassen, A. J. J., Mewe, R., Audard, M., et al. 2002, *Astronomy and Astrophysics*, 389, 228

- Raassen, A. J. J., van der Hucht, K. A., Miller, N. A., & Cassinelli, J. P. 2008, *Astronomy and Astrophysics*, 478, 513
- Rachevski, A., Zampa, G., Zampa, N., et al. 2014, *Journal of Instrumentation*, 9, P07014
- Ralchenko, Y. 2016, *Modern Methods in Collisional-Radiative Modeling of Plasmas* (Springer Series on Atomic, Optical, and Plasma Physics)
- Ranalli, P., Comastri, A., Origlia, L., & Maiolino, R. 2008, *Monthly Notices of the Royal Astronomical Society*, 386, 1464
- Rasmussen, A. P., Behar, E., Kahn, S. M., den Herder, J. W., & van der Heyden, K. 2001, *Astronomy and Astrophysics*, 365, L231
- Rauw, G., Hervé, A., Nazé, Y., et al. 2015, *Astronomy and Astrophysics*, 580, A59
- Raymond, J. C. & Brickhouse, N. S. 1996, *Astrophysics and Space Science*, 237, 321
- Rebusco, P., Churazov, E., Sunyaev, R., Böhringer, H., & Forman, W. 2008, *Monthly Notices of the Royal Astronomical Society*, 384, 1511
- Ross, R. R., Fabian, A. C., & Brandt, W. N. 1996, *Monthly Notices of the Royal Astronomical Society*, 278, 1082
- Rudge, C. M. & Raine, D. J. 1999, in *Astronomical Society of the Pacific Conference Series*, Vol. 175, *Structure and Kinematics of Quasar Broad Line Regions*, ed. C. M. Gaskell, W. N. Brandt, M. Dietrich, D. Dultzin-Hacyan, & M. Eracleous, 257
- Rugge, H. R. & McKenzie, D. L. 1985, *The Astrophysical Journal*, 297, 338
- Russell, H. N. & Saunders, F. A. 1925, *The Astrophysical Journal*, 61, 38
- Rybicki, G. B. & Lightman, A. P. 1979, *Radiative processes in astrophysics* (New York, Wiley-Interscience, 1979. 393 p.)
- Saba, J. L. R., Schmelz, J. T., Bhatia, A. K., & Strong, K. T. 1999, *The Astrophysical Journal*, 510, 1064
- Sakelliou, I., Peterson, J. R., Tamura, T., et al. 2002, *Astronomy and Astrophysics*, 391, 903
- Sako, M., Kahn, S. M., Behar, E., et al. 2001, *Astronomy and Astrophysics*, 365, L168
- Salak, D., Nakai, N., Miyamoto, Y., Yamauchi, A., & Tsuru, T. G. 2013, *Publications of the Astronomical Society of Japan*, 65, 66
- Sampson, D. H., Zhang, H. L., Mohanty, A. K., & Clark, R. E. H. 1989, *Physical Review A*, 40, 604
- Santos-Lleo, M., Schartel, N., Tananbaum, H., Tucker, W., & Weisskopf, M. C. 2009, *Nature*, 462, 997

- Savin, D. W., Beiersdorfer, P., Kahn, S. M., et al. 2000, *Review of Scientific Instruments*, 71, 3362
- Schaaf, R., Pietsch, W., Biermann, P. L., Kronberg, P. P., & Schmutzler, T. 1989, *The Astrophysical Journal*, 336, 722
- Schippers, S., Beerwerth, R., Bari, S., et al. 2021, *The Astrophysical Journal*, 908, 52
- Schmelz, J. T., Saba, J. L. R., & Strong, K. T. 1992, *Astrophysical Journal Letters*, 398, L115
- Schmidt, M., Zschornack, G., Kentsch, U., & Ritter, E. 2014, *Review of Scientific Instruments*, 85, 02B704
- Schreier, E., Levinson, R., Gursky, H., et al. 1972, *Astrophysical Journal Letters*, 172, L79
- Schwartz, D. 2010, *Proceedings of the National Academy of Science*, 107, 7190
- Shah, C., Amaro, P., Steinbrügge, R., et al. 2018, *The Astrophysical Journal Supplement Series*, 234, 27
- Shah, C., Crespo López-Urrutia, J. R., Gu, M. F., et al. 2019, *The Astrophysical Journal*, 881
- Shah, C., Jörg, H., Bernitt, S., et al. 2015, *Phys. Rev. A*, 92, 042702
- Shah, C., Togawa, M., Botz, M., et al. 2024, *arXiv e-prints*, arXiv:2401.08395
- Sherrill, C. D. & Schaefer, Henry F., I. 1999, *Advances in Quantum Chemistry*, 34, 143
- Shull, J. M., Smith, B. D., & Danforth, C. W. 2012, *The Astrophysical Journal*, 759, 23
- Simon, M. C., Schwarz, M., Epp, S. W., et al. 2010, *Journal of Physics B: Atomic, Molecular and Optical Physics*, 43, 065003
- Smith, B. W., Mann, J. B., Cowan, R. D., & Raymond, J. C. 1985, *The Astrophysical Journal*, 298, 898
- Smith, R. K., Abraham, M. H., Allured, R., et al. 2016, in *Society of Photo-Optical Instrumentation Engineers (SPIE) Conference Series*, Vol. 9905, *Space Telescopes and Instrumentation 2016: Ultraviolet to Gamma Ray*, ed. J.-W. A. den Herder, T. Takahashi, & M. Bautz, 99054M
- Smith, R. K., Brickhouse, N. S., Liedahl, D. A., & Raymond, J. C. 2001, *The Astrophysical Journal*, 556, L91
- Steinbrügge, R., Kühn, S., Nicastro, F., et al. 2022, *The Astrophysical Journal*, 941, 188
- Strickland, D. K. & Heckman, T. M. 2007, *The Astrophysical Journal*, 658, 258
- Strickland, D. K. & Heckman, T. M. 2009, *The Astrophysical Journal*, 697, 2030
- Strickland, D. K., Ponman, T. J., & Stevens, I. R. 1997, *Astronomy and Astrophysics*, 320, 378

- Strickland, D. K. & Stevens, I. R. 2000, *Monthly Notices of the Royal Astronomical Society*, 314, 511
- Strüder, L., Briel, U., Dennerl, K., et al. 2001, *Astronomy and Astrophysics*, 365, L18
- Sundqvist, J. O. & Owocki, S. P. 2015, *Monthly Notices of the Royal Astronomical Society*, 453, 3428
- Sundqvist, J. O., Owocki, S. P., & Puls, J. 2018, *Astronomy and Astrophysics*, 611, A17
- Takahashi, T., Kokubun, M., Mitsuda, K., et al. 2016, in Proceedings of SPIE, Vol. 9905, Space Telescopes and Instrumentation 2016: Ultraviolet to Gamma Ray, 99050U
- Tamura, T., Bleeker, J. A. M., Kaastra, J. S., Ferrigno, C., & Molendi, S. 2001a, *Astronomy and Astrophysics*, 379, 107
- Tamura, T., Kaastra, J. S., Peterson, J. R., et al. 2001b, *Astronomy and Astrophysics*, 365, L87
- Tanaka, K. 1986, *Astrophysics and Space Science*, 118, 101
- Tashiro, M., Maejima, H., Toda, K., et al. 2018, Proc. SPIE, 10699, 1069922
- Tubiana, M. 1996, Bulletin de l'Academie nationale de medecine, 180, 97
- van der Walt, S., Colbert, S. C., & Varoquaux, G. 2011, *Computing in Science and Engineering*, 13, 22
- Veilleux, S., Cecil, G., & Bland-Hawthorn, J. 2005, *Annual Review of Astronomy and Astrophysics*, 43, 769
- Viefhaus, J., Scholz, F., Deinert, S., et al. 2013, *Nuclear Instruments and Methods in Physics Research A*, 710, 151
- Virtanen, P., Gommers, R., Oliphant, T. E., et al. 2020, *Nature Methods*, 17, 261
- Vrtilek, S. D., McClintock, J. E., Seward, F. D., Kahn, S. M., & Wargelin, B. J. 1991, *The Astrophysical Journal Supplement Series*, 76, 1127
- Waljeski, K., Moses, D., Dere, K. P., et al. 1994, *The Astrophysical Journal*, 429, 909
- Walter, F., Weiss, A., & Scoville, N. 2002, *Astrophysical Journal Letters*, 580, L21
- Weisskopf, M. C. & Hughes, J. P. 2006, Six Years of Chandra Observations of Supernova Remnants (Springer Berlin Heidelberg), 55–113
- Weisskopf, M. C., Tananbaum, H. D., Van Speybroeck, L. P., & O'Dell, S. L. 2000, in Society of Photo-Optical Instrumentation Engineers (SPIE) Conference Series, Vol. 4012, X-Ray Optics, Instruments, and Missions III, ed. J. E. Truemper & B. Aschenbach, 2–16
- Werner, N., Zhuravleva, I., Churazov, E., et al. 2009, *Monthly Notices of the Royal Astronomical Society*, 398, 23

- Westmoquette, M. S., Smith, L. J., Gallagher, J. S., I., et al. 2007, *The Astrophysical Journal*, 671, 358
- Wilkes, B. J., Tucker, W., Schartel, N., & Santos-Lleo, M. 2022, *Nature*, 606, 261
- Wolfson, C. J., Leibacher, J. W., Doyle, J. G., & Phillips, K. J. H. 1983, *The Astrophysical Journal*, 269, 319
- Wong, K. L., Beiersdorfer, P., Reed, K. J., & Vogel, D. A. 1995, *Physical Review A*, 51, 1214
- Xu, H., Kahn, S. M., Peterson, J. R., et al. 2002, *The Astrophysical Journal*, 579, 600
- Xue, Y., Ginzell, R., Krauß, A., et al. 2014, *Physical Review A*, 90, 052720
- Zatsarinny, O., Gorczyca, T. W., Korista, K., Badnell, N. R., & Savin, D. W. 2004, *Astronomy and Astrophysics*, 426, 699
- Zatsarinny, O., Gorczyca, T. W., Korista, K. T., et al. 2005, *Astronomy and Astrophysics*, 438, 743
- Zhang, D., Thompson, T. A., Quataert, E., & Murray, N. 2017, *Monthly Notices of the Royal Astronomical Society*, 468, 4801
- Zhang, H. L., Sampson, D. H., & Mohanty, A. K. 1989, *Phys. Rev. A*, 40, 616
- Zhang, S., Wang, Q. D., Ji, L., et al. 2014, *The Astrophysical Journal*, 794, 61
- Zhekov, S. A. & Palla, F. 2007, *Monthly Notices of the Royal Astronomical Society*, 382, 1124
- Zhong, J. Y., Wang, C., Zhang, J., et al. 2004, *Physical Review A*, 70, 053803
- ZuHone, J. A., Schellenberger, G., Ogorzałek, A., et al. 2024, *The Astrophysical Journal*, 967, 49